

REPORT DOCUMENTATION PAGE

Form Approved
OMB No. 0704-0188

Public reporting burden for this collection of information is estimated to average 1 hour per response, including the time for reviewing instructions, searching existing data sources, gathering and maintaining the data needed, and completing and reviewing the collection of information. Send comments regarding this burden estimate or any other aspect of this collection of information, including suggestions for reducing this burden, to Washington Headquarters Services, Directorate for Information Operations and Reports, 1215 Jefferson Davis Highway, Suite 1204, Arlington, VA 22202-4302, and to the Office of Management and Budget, Paperwork Reduction Project (0704-0188), Washington, DC 20503.

1. AGENCY USE ONLY (Leave blank)		2. REPORT DATE 7/7/95	3. REPORT TYPE AND DATES COVERED Final ; 02/01/94 - 04/30/95	
4. TITLE AND SUBTITLE Thrust Vector Control of Rectangular Jets Using Counterflow			5. FUNDING NUMBERS F49620-94-1-0159 AFOSR TR 95 0642	
6. AUTHOR(S) A. Krothapalli and D.J. Forliti				
7. PERFORMING ORGANIZATION NAME(S) AND ADDRESS(ES) Florida State University FAMU-FSU College of Engineering Department of Mechanical Engineering 2525 Pottsdamer St., Room 229 Tallahassee, FL 32310			8. PERFORMING ORGANIZATION REPORT NUMBER FMRL-TR95-1	
9. SPONSORING/MONITORING AGENCY NAME(S) AND ADDRESS(ES) Air Force Office of Scientific Research AFOSR/NA 110 Duncan Avenue, Suite B115 Bolling AFB, DC 20332-0001			10. SPONSORING/MONITORING AGENCY REPORT NUMBER NA F49620- 94-1-0159	
11. SUPPLEMENTARY NOTES				
12a. DISTRIBUTION/AVAILABILITY STATEMENT Approved for public release, distribution unlimited			12b. DISTRIBUTION CODE DTIC SELECTED OCT 17 1995 F	
13. ABSTRACT (Maximum 200 words) This research studied the flow generated by a rectangular convergent-divergent Mach 2 nozzle operated in a free jet and a counterflow thrust vectored configuration. Particle Image Velocimetry was used to obtain 2D velocity fields and total and static pressures were measured. In the free jet configuration, the nozzle was operated at ideal, over, and under-expanded conditions. The growth of shear layers was unaffected by shock cells for mildly off-design conditions. The thrust vector configuration is similar to an ejector, where suction is applied to one side of the jet. This creates a cross-stream pressure gradient resulting in a vectoring of the jet. The application of suction creates counterflow. This gives the jet a streamwise curvature, the destabilizing nature of which causes an increase in the growth of the non-suction side of the shear layer. The suction side shear layer experiences counterflow and both destabilizing and stabilizing curvature. It becomes thicker with suction, suggesting a self-excited state. The development of large scale structures when suction is applied gives further evidence of self-excitation. These structures cause enhanced mixing resulting in the cross-stream pressure gradient which leads to vectoring.				
14. SUBJECT TERMS			15. NUMBER OF PAGES 135	
			16. PRICE CODE	
17. SECURITY CLASSIFICATION OF REPORT	18. SECURITY CLASSIFICATION OF THIS PAGE	19. SECURITY CLASSIFICATION OF ABSTRACT	20. LIMITATION OF ABSTRACT	

DTIC QUALITY INSPECTED 5

TABLE OF CONTENTS

ABSTRACT	xv
CHAPTER 1: INTRODUCTION	1
CHAPTER 2: BACKGROUND	3
Shear Layers	3
Compressible Shear Layers	7
Stability of Shear Layers	9
Compressible Flow	15
Jet Excitation	17
Rectangular Jets	19
CHAPTER 3: EXPERIMENTAL FACILITY	22
High Speed Jet Facility	22
Thrust Vectoring Configuration	24
Schlieren Setup	27
Particle Image Velocimetry	28
Pressure Measurements	31
CHAPTER 4: RESULTS	32
Nozzle Operation	33
Free Jet Particle Image Velocimetry Results	34
Thrust Vectoing Schlieren Flow Visualization	46

19951013 033

Bistability	50
Thrust Vectoring PIV Results	52
Similarity and Shear Layer Growth of the Free Jets	67
Free Jet v Component Measurements	73
Growth of Shear Layers for the Thrust Vectored Jets	76
CHAPTER 5: CONCLUSION	84
APPENDICES	86
REFERENCES	121
BIOGRAPHICAL SKETCH	124

Accession For	
NTIS CRA&I	<input checked="checked" type="checkbox"/>
DTIC TAB	<input type="checkbox"/>
Unannounced	<input type="checkbox"/>
Justification _____	
By _____	
Distribution / _____	
Availability Codes	
Dist	Avail and/or Special
A-1	

LIST OF FIGURES

Figure 1.1: Improved maneuverability of an aircraft with thrust vectoring	1
Figure 2.1: The coflowing shear layer	4
Figure 2.2: Example of a counterflowing shear layer	6
Figure 2.3: Coflowing turbulent structures	10
Figure 2.4: Convective instability time-space plot	11
Figure 2.5: Absolute instability time-space plot	12
Figure 2.6: Jet with streamwise curvature	14
Figure 2.7: Edge tone emitted by a probe in a supersonic shear layer	17
Figure 3.1: High speed facility	22
Figure 3.2: Thrust vectoring nozzle configuration	24
Figure 3.3: Static pressure port schematic	26
Figure 3.4: Suction configuration	27
Figure 3.5: Schlieren setup	28
Figure 3.6: Seeding the counterflow	29
Figure 3.7: PIV setup	30
Figure 4.1: PLS image of the span of the long dimension Mach 2 shear layer	33
Figure 4.2: PIV image of ideally expanded jet (short dimension)	35
Figure 4.3: Instantaneous velocity field for the ideally expanded jet (short dimension)	36

Figure 4.27: Thrust vectoring centerline velocity magnitude profiles	61
Figure 4.28: Centerline velocity vector angle for vectored jet cases	62
Figure 4.29: Thrust vectoring shock structure	62
Figure 4.30: Thrust angle distribution for the unvectored jet	63
Figure 4.31: Thrust angle distribution for the vectored jets	64
Figure 4.32: Exit total pressure profiles	66
Figure 4.33: Ideally expanded streamwise velocity profiles	67
Figure 4.34: Velocity shear layer growth of the ideally expanded free jet	68
Figure 4.35: Velocity shear layer growth for the free jets	70
Figure 4.36: Free jet shear layer similarity	71
Figure 4.37: Comparison of a velocity profile using PIV and pressure measurements	73
Figure 4.38: v velocity component profiles for the ideally expanded jet (expansion)	74
Figure 4.39: v velocity component profiles for the ideally expanded jet (compression)	75
Figure 4.40: Velocity shear layer growth for the ejector case	76
Figure 4.41: Curvature effects on the free side shear layer growth	79
Figure 4.42: Suction effects on the collar side shear layer growth	80
Figure 4.43: Velocity ratio distribution for the thrust vectoring configuration	81
Figure 4.44: Instantaneous velocity fields for the counterflow region	83
Figure A.1: Mach 2 rectangular nozzle	87
Figure A.2: Coordinate system (collar is on the positive y side)	87
Figure A.3: External Jet Facility	88
Figure A.4: Thrust vectoring nozzle configuration	88
Figure A.5: Distribution of the number of velocity measurements used in the	

averaging of the short dimension ideally expanded free jet	89
Figure A.6: Mean velocity vector field for the overexpanded jet in the short dimension	90
Figure A.7: Mean velocity field for the underexpanded jet in the short dimension	90
Figure A.8a: PIV image of the underexpanded free jet in the long dimension	91
Figure A.8b: Mean velocity vector field for the underexpanded free jet in the long dimension	91
Figure A.9a: PIV image of the overexpanded free jet in the long dimension	92
Figure A.9b: Mean velocity vector field for the overexpanded free jet in the long dimension	92
Figure A.10: Iso-velocity contours for the ideally expanded free jet in the long dimension	93
Figure A.11: Iso-velocity contours for the overexpanded free jet in the long dimension	94
Figure A.12: Iso-velocity contours for the underexpanded free jet in the long dimension	94
Figure A.13: Comparison of centerline velocities of the ideally expanded jet in both dimensions	95
Figure A.14: Comparison of centerline velocities of the ideally expanded jet and the jet with the collar but no suction	96
Figure A.15: Thrust angle comparisons for the moderate suction case using different inclusion criteria	97
Figure A.16: Thrust angle comparisons for the maximum suction case using different inclusion criteria	98
Figure A.17: Vorticity distributions for the ideally expanded free jet; (a) long dimension, (b) short dimension	99
Figure A.18: Vorticity distributions for the overexpanded free jet; (a) long dimension, (b) short dimension	100
Figure A.19: Vorticity distributions for the underexpanded free jet; (a) long dimension, (b) short dimension	101

Figure A.20: Free jet cross-stream vorticity profiles for $x/H = 2.93$	102
Figure A.21: Vorticity distributions for the thrust vectored configuration; (a) no suction, (b) moderate suction	103
Figure A.22: Thrust vectored cross-stream vorticity profiles for $x/H = 2.83$ 104	
Figure A.23: Mach number profile as calculated from total (P_{o2}) and static pressure for $x/H = 4.9$	105
Figure A.24: v velocity component cross-stream profiles for the overexpanded free jet 106	
Figure A.25: v velocity component cross-stream profiles for the underexpanded free jet	107
Figure A.26: Static pressure profiles at various streamwise locations for the ideally expanded free jet	108
Figure A.27: Static pressure profiles at various streamwise locations for the thrust vectoring configuration without suction	109
Figure A.28: Static pressure profiles at various streamwise locations for the thrust vectoring configuration with moderate suction	110
Figure A.29: Total pressure profiles at various streamwise locations for the ideally expanded free jet	111
Figure A.30: Total pressure profiles at various streamwise locations for the thrust vectoring configuration without suction	112
Figure A.31: Total pressure profiles at various streamwise locations for the thrust vectoring configuration with moderate suction	113
Figure A.32: Total pressure profiles for various jet conditions at $x/H = 0.977$	114
Figure A.33: Total pressure profiles for various jet conditions at $x/H = 1.95$	115
Figure A.34: Total pressure profiles for various jet conditions at $x/H = 3.13$	116
Figure A.35: Total pressure profiles for various jet conditions at $x/H = 3.91$	117
Figure A.36: Total pressure profiles for various jet conditions at $x/H = 4.88$	118

LIST OF ABBREVIATIONS AND SYMBOLS

a_1	Speed of sound in the high speed side of a shear layer
a_2	Speed of sound in the low speed side of a shear layer
G	Height of the suction gap in the nozzle exit plane
H	Short dimension of the nozzle
L	Length of the collar
LDV	Laser Doppler Velocimetry
M	Mach number
M_1	Mach number of the high speed side of a shear layer
M_2	Mach number of the low speed side of a shear layer
M_c	Convective Mach number of a shear layer
N	Number of samples of velocity to be used in the average
NPR	Nozzle pressure ratio
P_b	Back pressure
$P_{exit,max}$	Maximum suction exit pressure for the unattached jet
$P_{o,jet}$	Stagnation pressure of the jet
PIV	Particle Image Velcimetry
PLS	Planar light sheet
P_{02}	Stagnation pressure behind a normal shock
P	Static pressure

P_{exit}	Static pressure in the suction gap in the nozzle exit plane
R	Radius of curvature of the collar
t	Time
T_{exit}	Static temperature in the nozzle exit plane
T_o	Stagnation temperature
U_1	The velocity of the high speed side of a shear layer
U_2	The velocity of the low speed side of a shear layer
$\bar{U}_{calculated}$	The calculated average of the velocity
\bar{U}_{actual}	The actual average of the velocity
ΔU	Velocity difference across the shear layer ($U_1 - U_2$)
$(U_2/U_1)_c$	Critical velocity ratio
u	Horizontal velocity component
v	Vertical velocity component
V	Velocity magnitude
V_1	Maximum velocity
V_2	Minimum velocity
W	Long dimension of the nozzle
x	Horizontal coordinate
y	Vertical coordinate
y_{mid}	The spatial middle of the shear layer
α	Collar divergence angle at the end of the collar
δ_{vel}	Shear layer thickness using 5-95% of the velocity profile
$\delta_{10-90\%}$	Shear layer thickness using 10-90% of the velocity profile
δ'	Shear layer growth rate ($d\delta/dx$)

δ'_i	Incompressible shear layer growth rate
δ'_c	Compressible shear layer growth rate
ρ_1	Density of the high speed side of a shear layer
ρ_2	Density of the low speed side of a shear layer
$\sigma_{\text{calculated}}$	The calculated standard deviation of a sampled variable (velocity)
σ_{actual}	The actual standard deviation of a sampled variable (velocity)
ω	Vorticity

ABSTRACT

This research involved an experimental study of the flow generated by a rectangular convergent-divergent Mach 2 nozzle operated in a free jet as well as a counterflow thrust vectored configuration. The study focused on the initial regions of the various jet flows. Particle Image Velocimetry was used to obtain 2D velocity fields in a selected plane of the flow in addition to the measurement of total and static pressures. The velocity calculated from the pressure measurements was found to be in excellent agreement with the PIV results. The portion of the research dealing with the nozzle in a free jet configuration focused on the effect of operating the nozzle at various exit conditions, ideal, over and underexpanded. It was found that the growth of the shear layers is unaffected by the various operating conditions, suggesting that shock cells do not influence the shear layer growth for mildly off design conditions. The shear layer velocity profiles were found to be self similar irrespective of the exit pressure ratios.

The thrust vectoring of the rectangular jet uses a unique nozzle configuration based on fluidic control. The nozzle configuration is similar to an ejector, where suction is applied to one side of the rectangular jet. This suction creates a cross-stream pressure gradient, which results in a vectoring of the jet. The application of suction creates counterflow, and the ensuing vectored jet has streamwise curvature. The streamwise curvature causes an increase in the growth of the non-suction side shear

layer due to the destabilizing nature of the curvature. The suction side shear layer experiences counterflow as well as destabilizing and stabilizing curvature. Growth rate measurements show that the suction side shear layer becomes thicker with suction, suggesting a self excited state. Instantaneous velocity fields show that large scale structures develop in the counterflowing shear layer when suction is applied, further evidence of self excitation. These structures cause enhanced mixing, resulting in the cross-stream pressure gradient which leads to the vectoring of the jet.

CHAPTER 1

INTRODUCTION

The ability to manipulate the exhaust gas of a jet engine provides an enhanced aircraft maneuverability. If the exhaust of a jet engine can be steered off the axis of the engine, then the resulting thrust force will have a component normal to the flight direction of the aircraft. This will cause a moment on the aircraft, thus turning will be possible without the use of flaps. With the ability to vector the thrust of a jet engine, the maneuverability of the aircraft will be improved (as depicted in Figure 1.1). This would

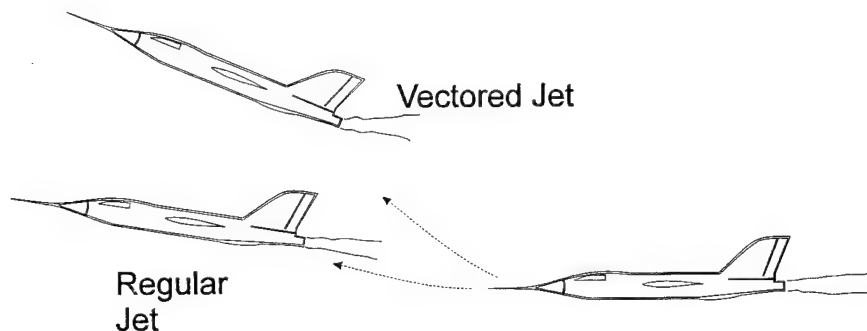


Figure 1.1: Improved maneuverability of an aircraft with thrust vectoring

be advantageous in an air-to-air combat situation. In addition to the improved maneuverability, thrust vectoring would allow for shortened runways due to the reduction in landing and take-off distances.

Many ways are currently being developed to vector jets. One of the most well known designs is Pratt & Whitney's Pitch/Yaw Balanced Beam Nozzle (see Boggs, 1992 for a qualitative description). The technique uses a nozzle that is constructed of surface sections that directs the exhaust up to 20° in any direction. The design uses a balance beam type mechanism to support the deflecting surfaces. Although this method is promising, it requires the use of moving parts to steer the thrust which are susceptible to failure. The design also suffers from heat transfer problems that can occur when the hot exhaust gas impinges on the directing surfaces. Various other thrust vectoring techniques are being explored, see Ashley (1995) for a general review. Most of the methods require moving parts and have heat transfer complications when the jet impinges on the controlling surfaces.

The following research deals with an experimental study of a thrust vectoring technique which uses fluidic control. The experimental objective involves the investigation of the Mach 2 nozzle in a free jet and counterflow thrust vectored configuration. The counterflow technique involves the application of suction to one side of the rectangular nozzle. This suction creates a cross-stream pressure gradient, which is required to vector the jet. The thrust vectored jet with suction will have both counterflow and streamwise curvature. The method requires no moving parts or deflecting surfaces, thus avoiding the complications encountered with most other techniques. This technique appears to be very promising considering that the counterflow method avoids these complications and has been shown to be able to vector a Mach 2 jet up to approximately 20° . An understanding of the role of the counterflow and curvature is the primary goal of the research.

CHAPTER 2

BACKGROUND

This chapter deals with some of the background topics that are relevant to the engineering problem at hand, which is thrust vectoring of a supersonic jet. The chapter begins with a discussion of shear layers, which play an important role on the development of the jet. The pertinent stability issues will follow, including the effects of counterflow and streamwise curvature. Characteristics of supersonic flows will be described, including the effect of the compressibility on the growth of shear layers as well as edge tones generated by intrusive probe measurement techniques. More fundamental issues relating to jets will include a discussion of methods of control of the jet development as well as flow characteristics of rectangular jets.

Shear Layers

An important and heavily studied flow in fluid mechanics is the coflowing shear layer (Figure 2.1). The understanding of this flow is important because of its role in combustion chambers and other mixing processes. The coflowing shear layer is generated by allowing two streams of fluid (with different velocity magnitudes) to come into contact downstream of a splitter plate. Momentum diffusion occurs between the two streams, which results in a smoothing of the cross stream velocity gradients as the flow develops downstream. At a particular streamwise location, the

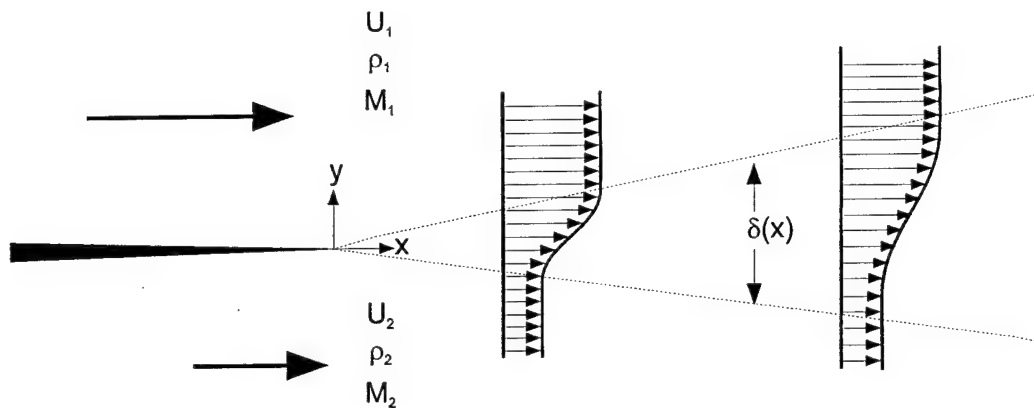


Figure 2.1: The coflowing shear layer

two uniform free streams are separated by a region where the mean velocity smoothly varies from one free stream value to the other (from U_2 to U_1). This region where the mean velocity differs from the freestream values is known as the shear layer.

The thickness of the shear layer can be defined differently depending on the type of information available about the flow development. A possible thickness, called δ_{vel} , bases the location of the edges of the shear layer to be where the mean velocity is near the free stream values (e.g. where U is equal to $U_2 + .05\Delta U$ and $U_1 - .05\Delta U$, where U_2 is the slower velocity of the two streams and $\Delta U = U_1 - U_2$). The distance between these points is the local shear layer thickness. Other common methods used to describe shear layer thickness' are; vorticity, visual, and pitot thickness. Although these different shear layer definitions have different values, they generally are proportional to each other.

The rate of change of the shear layer thickness with respect to the streamwise coordinate is called the shear layer growth rate ($d\delta/dx = \delta'$), which is an

important quantity because it is a measure of the mixing between the two streams. Because of the physical nature in which these shear layers develop (grow with space on average), they are categorized as spatially developing shear layers.

The growth of the spatially developing shear layer is a function of various parameters. In general, the important parameters are the density ratio (ρ_2/ρ_1), velocity ratio (U_2/U_1), and the Mach number ratio (M_2/M_1). Other factors may also come into play, such as the state of the boundary layer on the splitter plate. Brown and Roshko (1974) studied the effect of density ratio on the growth of coflowing shear layers. It was discovered from schlieren flow visualization images that large scale structures were present in the shear layer region. These structures are the primary mechanism for mixing between the two streams. It was concluded that the density ratio had a much weaker effect on the growth rate than the velocity ratio. Ever since the discovery of these structures, they have been the focus of many shear layer investigations. It has been shown that the theoretical velocity at which these structures (most unstable waves) travel downstream, called the group or convective velocity, is equal to the average of the free stream velocities (see Panton, 1984). Large deviations from theory have been observed when compressibility becomes a factor (Papamoschou, 1991).

A different type of shear layer can be generated by having the two streams flowing in opposite directions (counterflowing). A classical way to physically generate this shear layer uses two fluids of different density layered in a horizontal equilibrium (Figure 2.2). Tipping the container off balance will create a buoyancy driven flow in

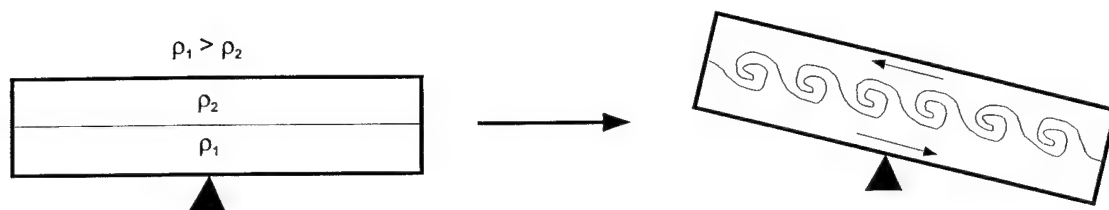


Figure 2.2: Example of a counterflowing shear layer

which the heavier fluid moves to a lower vertical level due to gravity, while the lighter fluid is pushed upward. A mixing layer will develop between the two fluids, lasting for a certain duration of time, until the fluids mix fully or separate due to a large density difference (highly stratified configuration). Either way, there is a point in time at which equilibrium is again reached. As with the coflowing shear layers, the mixing of the two streams is manifested in large scale structures. The growth of these structures is not spatial as in the coflowing case since the structures are at the same level of development throughout the streamwise extent of the flow (repetition of nearly identical vortex structures at a particular wavelength). The structures grow in time and have a finite lifetime, beginning when the disturbance from equilibrium occurs to the point when neighboring structures pair up, eventually breaking up into smaller scales. This type of flow is called a temporally developing shear layer (see Ramshankar, 1983 for a detailed analysis of flows generated with this type of facility).

Although temporal and spatial shear layers are quite different physically, there are some characteristics that are shared by the two flows. The phenomenon of pairing of neighboring structures is observed in both flows. The convective velocity of the vortex structures approaches the average of the two free stream velocities.

However, instead of the shear layer being contained in a wedge shape like spatial layers, temporal layers have uniform shear layer thickness'. Thus instead of a spatial growth rate, a temporal growth rate is used to describe the mixing. The temporal growth rate is the rate of change of the shear layer thickness with respect to *time*. Humphrey (1981) attempted to generate a stable counterflowing incompressible shear layer using two water tunnels. The resulting flow was not the desired shear flow, as a saddle point stagnation region formed in the center of the test section.

A shear layer will tend to exhibit the physical features of either spatial or temporal growth behavior. Some researchers have shown that one can relate spatial and temporal mixing layers through a transformation of reference frames (e.g. Hedges and Eberhardt, 1993). For example, a spatially developing shear layer can be analyzed in a temporal manner if the frame of reference travels at the convective velocity of the structures. One must keep in mind that doing such transformations also changes the relative velocity of the disturbance source (such as a splitter plate or nozzle).

Compressible Shear Layers

The understanding of the mixing characteristics of compressible shear layers has become a topic of intense interest due to the role it has in supersonic jet engine combustion chambers. Papamoschou and Roshko (1988) studied the effect of compressibility on the growth of coflowing shear layers. It was found that the normalized growth rate (compressible growth rate normalized by an appropriate incompressible growth rate) δ'_c/δ'_i decreases as the difference in the free stream

Mach numbers increases. A compressibility factor was suggested, called the convective Mach number, which is defined as,

$$M_c = \left(\frac{\frac{U_1 - U_2}{2}}{\frac{a_1 + a_2}{2}} \right) = \left(\frac{U_1 - U_2}{a_1 + a_2} \right) \quad (1)$$

which is the average Mach number of the two free streams in the frame of reference of a shear layer structure which travels at the average velocity of the two streams. U is the streamwise velocity and a is the speed of sound, the subscripts represent the quantities in the two different streams (1 is for the high speed side). When the convective Mach number is increased above approximately 0.25, a sharp decrease in the normalized growth rate was observed. In fact, data for a variety of operational conditions (U_2/U_1 , ρ_2/ρ_1 , and M_2/M_1) collapsed well onto one curve. Thus the usage of the convective Mach number as a compressibility parameter was justified. The effect of compressibility saturates at a convective Mach number of about 0.7, after which the compressible and incompressible growth rates change proportionally (normalized growth rate is nearly constant). These trends have been supported in a similar study using LDV measurements (Goebel and Dutton, 1991). Therefore the full set of parameters that determine the growth rate are the velocity ratio, density ratio, and convective Mach number.

Clemens and Mungal (1992) studied the structural characteristics of various convective Mach number shear layers. The results for the low convective Mach number shear layers had two dimensional structures, as found in incompressible shear layers. For $M_c > 0.6$, the structures become three dimensional, no longer

spanning the entire width of the shear layer. Shau et al. (1993) and Shau and Dolling (1992) studied the structure of the shear layer between two coflowing streams with Mach numbers of 3.0 and 5.0. This low convective Mach number study ($M_c = 0.3$) showed that the structures in the shear layer are tilted about 45 degrees in the traverse plane. Samimy et al. (1992) conducted an experimental study on shear layers having convective Mach numbers of 0.51 and 0.86. Using multiple spatial pressure measurements, it was found that the lower convective Mach number case has structures that are similar to that of the incompressible case, while the higher convective Mach number case has structures that are somewhat horseshoe shaped. Another important result was that the convective velocity measurements were shown to have a lot of jitter. Thus the geometry of the shear layer structures is highly dependent on the level of compressibility.

Stability of Shear Layers

As was mentioned previously, shear layers tend to fall into two groups according to their physical characteristics. One might ask what makes these two flows different. An approach from the concept of stability helps to understand the difference between these two flows.

In a typical coflowing shear layer, large turbulent structures have been observed to span the shear layer (Figure 2.3). These structures are the result of the instability of the boundary separating the two streams just downstream of the splitter plate. Small disturbances in the flow cause ripples to form on this boundary. These

ripples grow and roll up into vortical structures. The primary source for these disturbances is the boundary layer developing on each side of the splitter plate, in

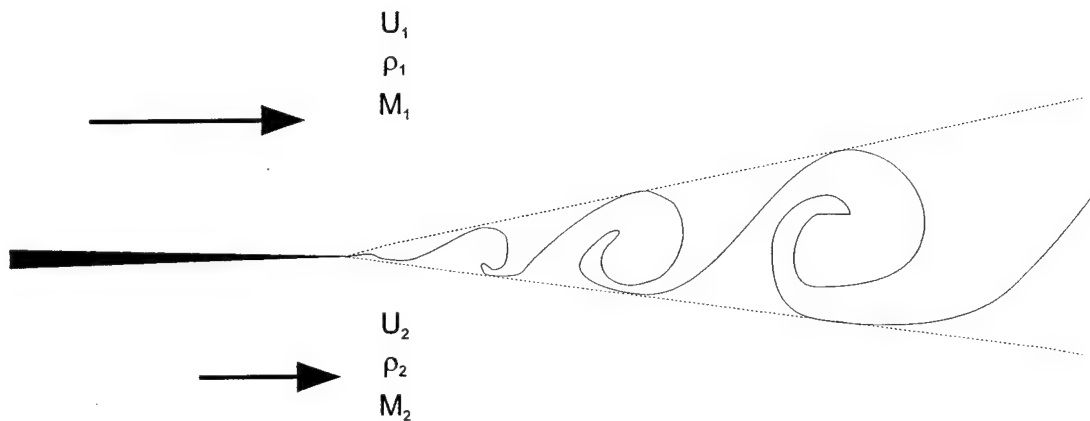


Figure 2.3: Coflowing turbulent structures

fact, some methods of shear layer excitation involve vibrating the splitter plate tip at a known preferred mode frequency. It has been shown that the amplitude of the disturbances play an important role in the growth of shear layers. In fact, Gutmark and Ho (1983) suggest that some of the discrepancies between some of the various experimental studies on the growth of shear layers is a result of the different initial disturbance levels that are present in different facilities.

In the coflowing shear layer, small disturbances are introduced into the flow from the splitter plate or nozzle. These disturbances grow as they travel downstream. The time-space plot helps to display this type of instability (Figure 2.4). X is the streamwise coordinate and t is time. If a disturbance is introduced into the flow at the origin, it will grow and move downstream. An observer at X_0 would first see the disturbance at time t_1 , and continue to see it until time t_2 , after which the disturbance has left the observers position. This type of flow is called convectively

unstable because the instability waves travel fast enough (as it grows) so that the entire disturbance moves downstream (travels faster than it grows). Spatially

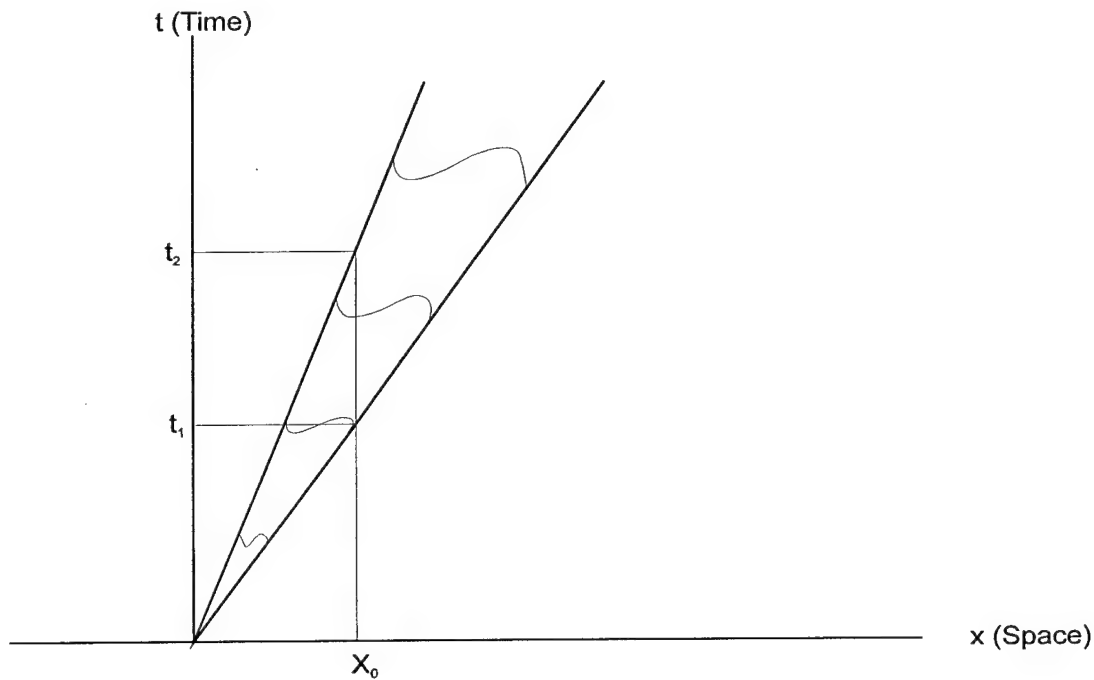


Figure 2.4: Convective instability time-space plot

developing shear layers are convectively unstable.

An alternative situation is depicted in Figure 2.5. In this case, an observer at x_0 would first see the disturbance at time t_1 , and then continue to see it from that time on for the lifetime of the disturbance. Therefore the disturbance does not travel, but amplifies in a stationary position. It is interesting to note that the disturbance even grows upstream. This flow is called absolutely unstable. Temporally developing shear layers are absolutely unstable.

What determines whether a shear layer is convectively or absolutely unstable? Just as for shear layer growth, the variables that determine this are the

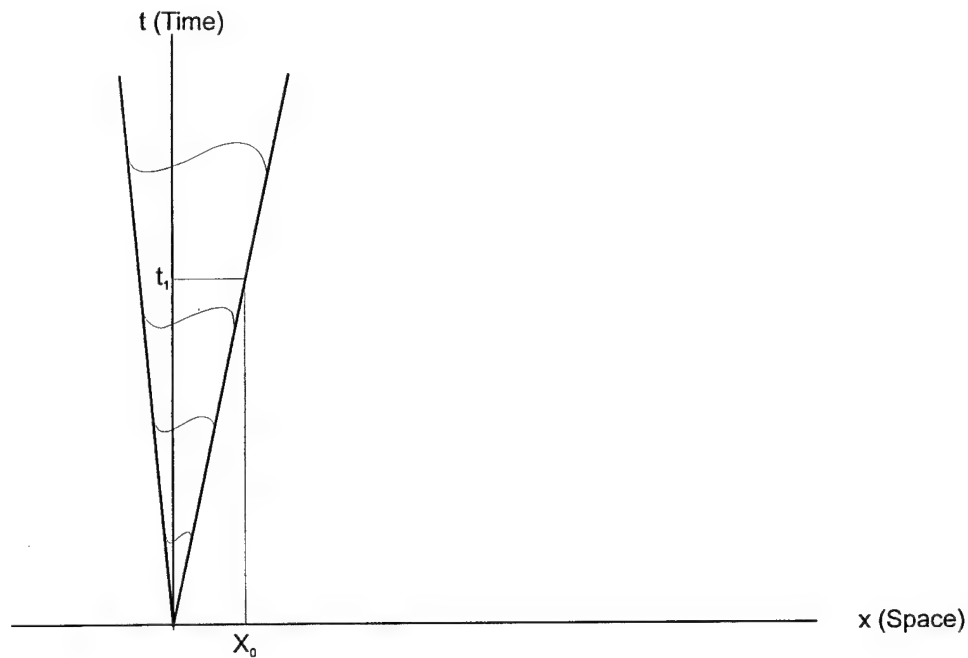


Figure 2.5: Absolute instability time-space plot

velocity ratio, density ratio, and convective Mach number. In general, it is considered that the velocity ratio is the most influential parameter, and easiest to manipulate. Thus we can define a critical velocity ratio $(U_2/U_1)_c$ as the velocity ratio bounding the flow between convective and absolute instability. This critical velocity ratio is a function of the density ratio and convective Mach number. For a velocity ratio below the critical value, which means higher levels of counterflow, the flow will be absolutely unstable. If the velocity ratio is larger than the critical value, the shear layer will be convectively unstable. It is interesting to note that the critical velocity ratio is negative, meaning that a shear layer with small levels of counterflow can still have a convective instability nature. The theoretical values which bound the flow regimes between convective and absolute instability for an axisymmetric shear layer (initial region of a coaxial counterflowing axisymmetric jet) can be found in Strykowski

et al. (1994). For a density ratio of 1.0 and incompressible flow ($M_c \approx 0$), the critical velocity ratio is approximately -0.15. Boundary curves defining the critical velocity ratio as a function of convective Mach number for different wave numbers (corresponding to helical modes) are also given for a density ratio of 1.0. The most unstable modes are of the helical type at higher convective Mach numbers. It is important to note that as the convective Mach number is increased and the density ratio is decreased (approaching the experimental conditions for this study), the critical velocity ratio drops to approximately -0.30 considering the more unstable higher wave number modes.

At this point, a qualitative discussion of the growth rate behavior of shear layers as a function of the velocity ratio can be done. When U_2 is equal to U_1 , there is no shearing and the flow is controlled by a wake instability. The wake instability is manifested in pairs of vortex structures that are shed asymmetrically from the splitter plate. If U_2 is lowered, shear layer instabilities develop. Cross stream profiles have been shown to have characteristics of both shear and wake modes for velocity ratios near unity (Papamoschou and Roshko, 1988). As U_2 is further lowered, the shear layer instability begins to dominate, and the flow field is of the convectively unstable type. Since the structures travel at the average velocity of the two streams, their convection velocities decrease with decreasing U_2 , leading to larger shear layer growth rates since the structures have a longer time over which to entrain. Thus the shear layer growth rate starts at zero for U_2 equal to U_1 and increases as the velocity ratio is lowered. When U_2 is lowered to zero, the shear layer is like that found in a free jet. The growth continues to increase as U_2 becomes negative. When the

velocity ratio begins to exceed the critical velocity ratio, absolute instability regions develop in the flow. If a large enough region of absolute instability is present in the flowfield, then global changes in the flow can occur. Hidden in this analysis is the effect of lowering U_2 on the compressibility. As U_2 is reduced, the convective Mach number increases, which causes a reduction in the normalized growth rate. Therefore the net effect of lowering U_2 on the shear layer growth depends on two counteracting effects, decreasing velocity ratio and increasing convective Mach number.

In addition to the disturbance instabilities, a vectored jet will have the added complication of streamwise curvature as shown in Figure 2.6. At a particular

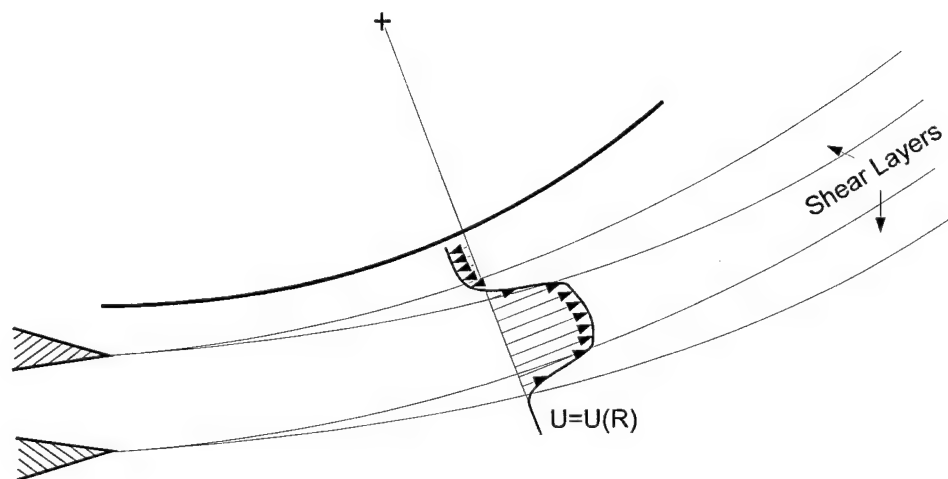


Figure 2.6: Jet with streamwise curvature

streamwise location, the velocity will be a function of the radial distance from the polar coordinate origin (dependent on the radius of curvature of the flow). Rayleigh's curved shear layer instability theory states that the effect of the curvature on the growth of a curved shear layer depends on the rate of change of the magnitude of

the angular momentum (Drazin and Reid, 1981). If the angular momentum magnitude is decreasing with radial distance, then the curvature has a destabilizing effect. An increasing angular momentum has a stabilizing effect. Mathematically, these conditions can be stated as,

$$\frac{\partial (UR)^2}{\partial R} > 0 \quad \text{stabilizing curvature}$$

$$\frac{\partial (UR)^2}{\partial R} < 0 \quad \text{destabilizing curvature}$$

Plesniak and Johnston (1989) studied the effect of curvature on incompressible coflowing shear layers using a water facility. This particular study was done for an average shear layer thickness equal to 5% of the radius of curvature of the flow. The destabilizing curvature shear layer growth rate was nearly twice that of a straight shear layer at similar conditions. This enhanced mixing has been speculated to be due to enhanced growth of the streamwise vorticity. See Bernal and Roshko (1986) for a study on the streamwise vortex structures found in an incompressible planar shear layer without curvature.

Compressible Flow

The assumption of incompressibility holds up well for gases flowing at low velocities when referenced to the local speed of sound. The general convention is that when the Mach number exceeds 0.3, the flow becomes compressible, meaning that density changes become significant. Many textbooks discuss the details of compressible flow, see for example Shapiro (1953) or Saad (1993).

For supersonic convergent-divergent nozzles, the operational regime is a function of the area ratio of the nozzle and the stagnation to back pressure ratio. The area ratio is set to generate the desired isentropic design Mach number, and the nozzle pressure ratio (NPR) defined as,

$$NPR = \frac{p_o}{p_b} \quad (2)$$

describes the operational conditions. When the NPR is dropped below the design value by a moderate amount (i.e. no shocks are present inside the nozzle), the static pressure of the flow in the exit plane of the nozzle is lower than the back pressure. This generates a compression wave system that raises the static pressure of the jet to satisfy the constant pressure boundary. This condition is termed overexpanded. The compression of the flow results in a pinching of the jet just downstream of the nozzle exit. When the NPR is raised above the design value, the pressure in the nozzle exit plane is larger than the back pressure. An expansion fan develops to satisfy the constant pressure boundary. This flow condition is called underexpanded. The expansion process causes an expanding of the jet in the region just downstream of the nozzle exit. Although these two off design conditions begin with waves of opposite nature, the waves reflect off the shear layer as their complimentary wave, thus compression waves become an expansion fan and vise-versa. Thus both flows contain expansion and compression waves.

One of the difficulties with supersonic flow experiments is the sensitivity of the flow to intrusive measurement techniques. As observed by Powell (1953), an acoustic tone is emitted by a probe placed in a supersonic flow. This phenomena

illustrated in Figure 2.7 is called edge tone generation. The edge tones created by a probe would be similar to a point acoustic source. In an experimental setting, a high pitch tone can be distinctively heard when a probe passes through a supersonic

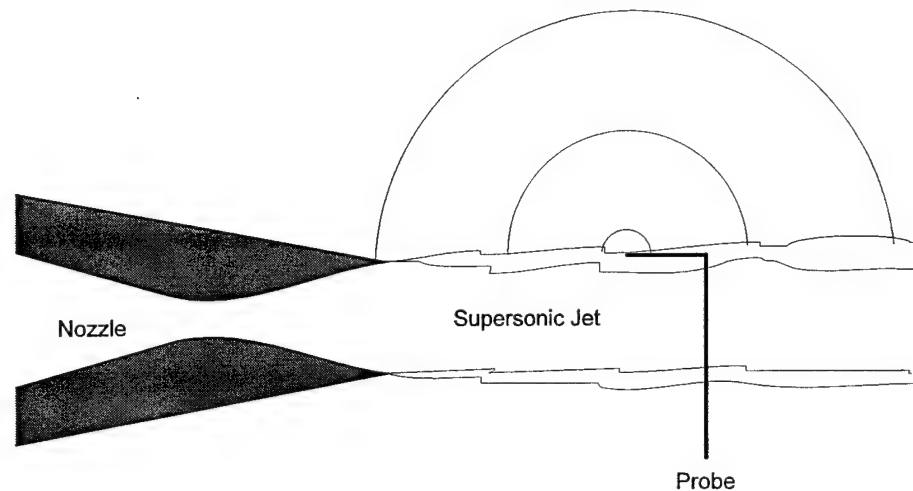


Figure 2.7: Edge tone emitted by a probe in a supersonic shear layer

shear layer. The edge tones propagate upstream to the nozzle lip and can influence the initial region of the shear layer. Constructive or destructive interference can occur depending on the phase difference between the edge tones and shear layer structure formations.

Jet Excitation

There have been many studies which involve the mixing enhancement of jets. A classic paper by Crow and Champagne (1971) describes some of the structure present in an incompressible turbulent jet. To help separate the preferred mode from the other weak modes present, forcing of the jet was done using acoustic excitation upstream of the nozzle exit. It was found that forcing the jet at the preferred mode

frequency or its first harmonic increased the root mean square of the velocity along the centerline, as well as accelerating the decay of the centerline mean velocity (shortened potential core length). Thus mixing was enhanced by the acoustic excitation. The entrainment was found to be increased in the first six diameters above the levels of the unforced case. The effect of the forcing amplitude was determined by measuring the rms velocity at a fixed point for a variety of excitation levels (frequency was also varied separately). At the preferred mode frequency, the rms of the velocity fluctuations increased with the forcing amplitude, eventually saturating. This method of controlling the jet is effective, but it requires the knowledge of the preferred mode frequency. This can complicate things because of the dependence of the preferred mode frequency on the small disturbance level variations attributed to different facilities (Gutmark and Ho, 1983). Lepicovsky et al. (1987) showed that acoustic excitation can be used to excite the preferred mode of a supersonic jet, but the forcing had very little effect on the overall flow characteristics. Thus enhanced mixing of supersonic jets through the use of acoustic excitation may not be effective.

To avoid the complexities of such active forcing techniques, a passive approach to jet excitation can be used. A technique that uses counterflowing coaxial jets has been used to gain control of the jet development. A circular jet can be modified by placing an annular gap around the perimeter of the jet in the exit plane, and the gap manifold can be attached to a suction system to generate counterflow (see Strykowski and Niccum, 1991 for a complete facility description). A collar can be placed extending downstream of the jet exit to generate a large streamwise region

where high levels of counterflow is present. An experimental investigation of this configuration can be found in Strykowski and Wilcoxon (1993). It was found that the length of the potential core decreased with increasing counterflow (decreasing velocity ratio) and higher velocity fluctuation rms peaks on the centerline axis. These trends are identical to that described earlier for the acoustic excitation results of Crow and Champagne (1971). One interesting observation was that suppressed mixing occurred for low levels of counterflow when the boundary layer inside the nozzle was laminar at the nozzle exit. The effect of counterflow on the jet with tripped boundary layers always enhanced mixing, even in the convectively unstable regime. For both boundary layer conditions, once the velocity ratio exceeded the critical value, enhanced mixing was observed. Regions of absolute instability cause disturbances to travel upstream and disturb the shear layer, thus the shear layer becomes self-excited. As the counterflow increases to nearly twice the critical amount, large oscillations in the entire flow arise. These global oscillations occur at a frequency which is constant in the entire flowfield. The flow has acquired a globally unstable mode.

Rectangular Jets

The usage of rectangular nozzles on jet engines is attractive because of the different mixing characteristics of such a nozzle geometry. Quinn (1992) studies the flowfield of a square jet and showed that large streamwise vortex structures were being generated at the corners of the nozzle. This streamwise vorticity helps the rectangular jet mix faster than the axisymmetric jet. Krothapalli et al. (1981) studied

the mixing of an incompressible rectangular jet of moderate to large aspect ratio. They found that the flow development was characterized by three streamwise regions. The first was the potential core region, where the centerline velocity is invariant. The second region (called the two dimension region) has a decay rate in the streamwise velocity that differs from that of the axisymmetric jet. The third region is where the centerline decay agrees with that of round jets, and is called the axisymmetric region. The third region usually begins somewhere on the order of 100 short widths of the rectangular nozzle (depending on the jet initial conditions and nozzle aspect ratio). The different growth behavior in the major and minor planes causes the familiar axis switching (long dimension of the jet becoming the short, and vice-versa). The location of the axis switching is a function of the aspect ratio of the nozzle.

Krothapalli et al. (1986) followed up with a study on the screech tone emission of an underexpanded rectangular jet. Strong sound generation was observed to occur in an underexpanded jet (emanating from a convergent rectangular nozzle) near the third shock cell when the pressure ratio was set near a critical value. These sound waves propagate in the ambient fluid and reach the nozzle lip, where they can excite the newly formed shear layer. Thus the screech tone forms a feedback loop resulting in an increased spread rate. The jet becomes self excited, just as with counterflow, in a passive manner.

The instability modes of a rectangular jet (aspect ratio of 4.0) under a wide range of operational conditions was reported by Shih et al. (1992). It was found that both symmetric and antisymmetric modes exist (depending on the operation

conditions), and that the screech tones have an antisymmetric nature. In this study, examination of the near field of a supersonic rectangular jet was carried out. The Mach 2 nozzle was operated under free and counterflow thrust vectored conditions. The effect on the global flowfields of operating off design (such as flapping caused the screech tone feedback loop) will be studied. The instability mechanisms including the effects of counterflow and streamwise curvature on the vectored jet will also be explored.

CHAPTER 3

EXPERIMENTAL FACILITY

High Speed Jet Facility

The experiments were conducted at the Florida A & M University / Florida State University Fluid Mechanics Research Laboratory located on the Florida State University campus. The high speed lab schematic is shown in Figure 3.1.

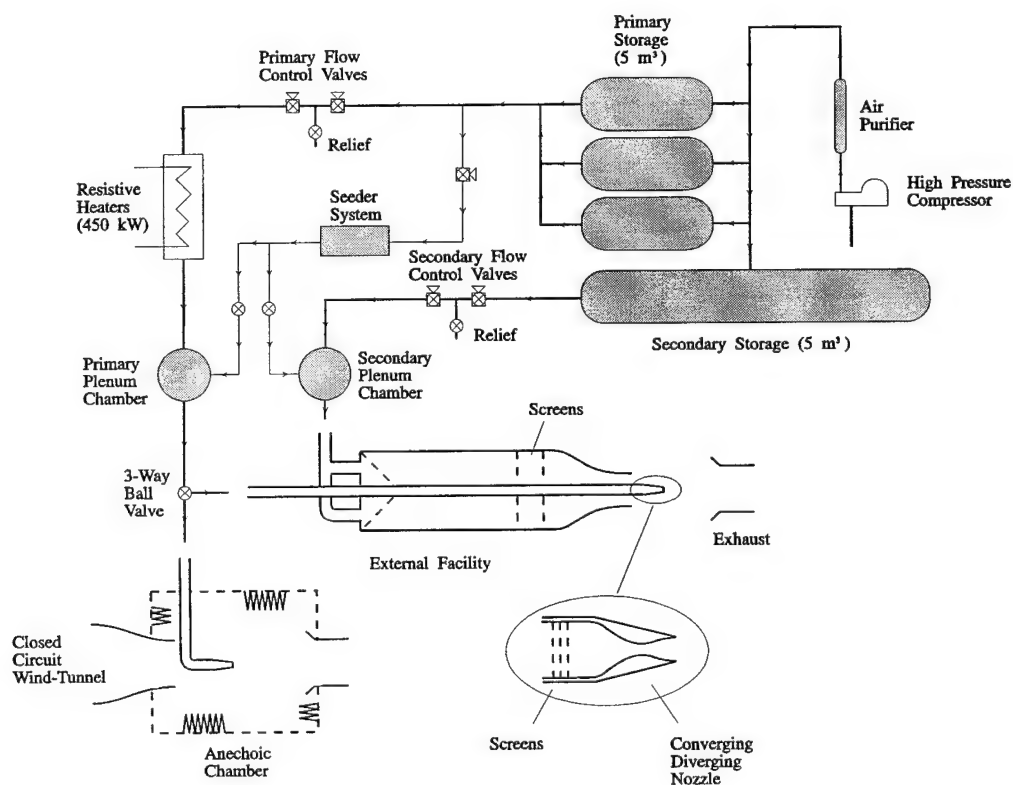


Figure 3.1: High speed facility

High speed flows can be generated in this two part facility. Part one of the facility implements an anechoic chamber in line with a closed circuit subsonic wind tunnel to study aeroacoustics. The external half of the facility is used to measure various other quantities of high speed flows such as static and total pressures as well as velocities using Particle Image Velocimetry. All of the experiments that will be discussed were done using the external facility. Both halves of the high speed facility are of the blow-down type. A Bauer four stage reciprocating compressor compresses air that is stored in our primary and secondary tanks which have a net volume of 10 m^3 . The tanks, which have a maximum pressure limit of 2000 psig, are connected to the external facility through a series of stages. Two Fisher Controls pneumatic control valves reduce the pressure from the tank (held within 2000-500 psig during experiments) to obtain the desired stagnation pressure. The flow then passes through two Watlow resistance heaters that are capable of heating the jet up to stagnation temperatures of approximately 1000°F . The flow continues through a settling chamber and ball valve before entering the external facility. One of the advantages of this facility is its versatility. Besides the anechoic chamber, the external facility can generate a secondary annular flow (up to a Mach number of about 1.0) that can be used to study coflowing jets, thus simulating aircraft flight. The facilities can be fitted with various nozzles to study jets of different Mach numbers and geometrical configurations (axisymmetric, rectangular, diamond, etc.). Since Particle Image Velocimetry (PIV) is a primary measurement tool in this laboratory, the flow needs to be seeded with particles. To accomplish this, a seeding mechanism was put in parallel with the primary flow (Ross, 1993). A cyclone is used to remove

larger particles and agglomerations. The seeded flow is then combined with the primary flow as it enters the external facility. The author references Wishart (1995) for a more detailed description of the high speed jet facility.

Thrust Vectoring Configuration

The thrust vectoring nozzle configuration is shown in Figure 3.2. The nozzle used is a converging-diverging rectangular nozzle (aspect ratio of 4.0) with short and long dimensions of 13 and 52 mm respectively. The throat to exit area ratio is designed for an isentropic Mach number of 2.0. A manifold is created on the top and

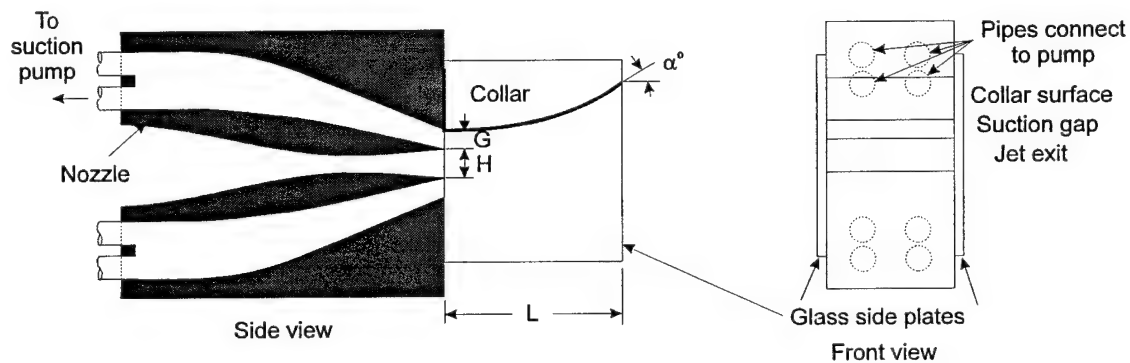


Figure 3.2: Thrust vectoring nozzle configuration

bottom of the nozzle exterior, so that a small gap exists above and below the nozzle in the long dimension. These manifolds are connected to a suction pump that generates the counterflow. The purpose of the two gaps is to allow for vectoring in both directions in the vertical plane. A surface (referred to as the collar) is placed extending downstream from the exit plane so that when the counterflow is applied, a

large streamwise region of the jet is exposed to the counterflow. Usually two collars would be present so that the jet can be vectored in both directions, but since PIV will be one of the measurement techniques used, the bottom collar is removed to allow for laser illumination of the flow. Plexi glass side plates are used as side walls to ensure that the generated counterflow actually flows opposite to the jet, otherwise most of the flow would come in from the sides.

There are numerous geometrical parameters that can be varied in the current configuration, such as R/H , G/H , L/H , and the slope of the collar at the downstream end α (the collar profile follows a sector of a circle of radius R). A previous study was done on a low speed facility of similar construction to get an understanding of the effect of these parameters on the vectoring performance (Van der Veer, 1995). A brief study was done on the high speed facility to approximate the optimum geometrical configuration. One of the important factors was whether the jet attached to the collar surface when sufficient suction was applied. If the jet attaches to the collar, then the suction needs to be reduced to a lower value for the jet to pull away from the collar, thus a temporary loss of control results (for a detailed description of this hysteresis effect, see Van der Veer, 1995). Qualitatively, this attachment of the jet to the collar can be avoided by increasing the suction gap height G , and reducing the length of the collar L , but as these changes are made, it becomes harder to vector the jet. The geometry that seems to compromise these two counteracting effects have a G/H and L/H of 0.385 and 6.8 respectively. The collar shape has been empirically determined in a previous study to have good vectoring capabilities and minimal attachment problems.

A previous study was conducted in which static pressure distribution measurements along the surface of the collar were made. It was found (Strykowski et al., 1995) that the observed vectored jet angle is a linear function of the static pressure in the exit plane of the nozzle (on the suction side). In fact, the data collapsed onto one line, which included different gap heights and jet stagnation temperatures. Thus the static pressure in the gap at the nozzle exit, P_{exit} , was

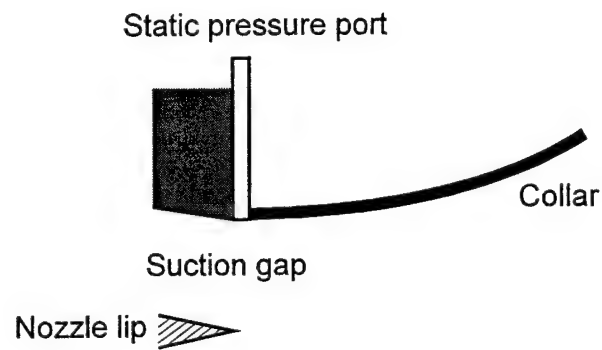


Figure 3.3: Static pressure port schematic

measured and held constant to get a particular vectored jet angle. The static pressure port shown in Figure 3.3 is connected using tygon tubing to a Wallace & Tiernan series 66-100 digital pressure transducer with a maximum differential pressure of 15 psid.

The nozzle configuration is connected to the Fuji three phase ring compressor (model number 804) as shown in Figure 3.4. The compressor is connected to the nozzle through four rubber hoses and 2" ID PVC as shown in the schematic. A bleed off line and two valves are used to vary the amount of suction that is applied to the

nozzle configuration. A pitot static probe located in the PVC section is used to measure the flow rate of the counterflow. In general, the mass flow rate was very unsteady and mean values did not vary much at the various vectoring angles.

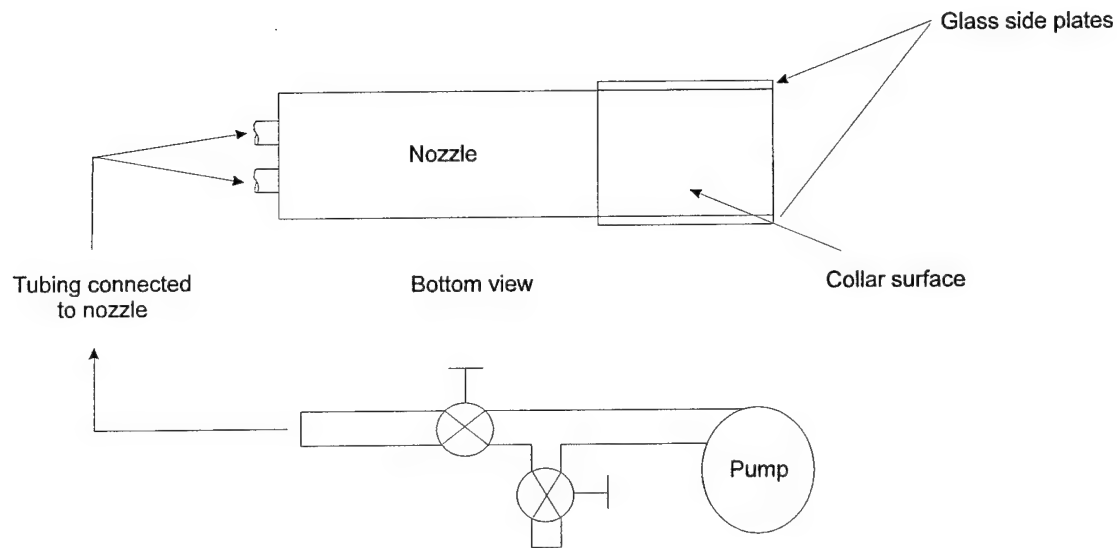


Figure 3.4: Suction configuration

Schlieren Setup

Flow visualization images were acquired using the Schlieren system shown in Figure 3.5. The light source used was a EG & G Electro-Optics flash tube which can generate high frequency pulses of light. The plano-convex lens focuses the light onto a horizontally slitted plate (to emphasize vertical density gradients). A convex mirror located at the focal length from the slit collimates the light, which reflects off a plane mirror and then passes through the test section. The jet is being vectored in a plane that is perpendicular to the light rays. The light is then reflected again by a plane mirror onto a convex mirror that focuses the light onto a horizontal knife edge

(sensitive to vertical density gradients). The image was then captured on a Kodak MEGAPLUS CCD Camera Model 4.2 which has 2000x2000 pixel resolution. The camera is controlled by FFD's Mark IV PIV software which is run on an IBM RISC Powerserver 340.

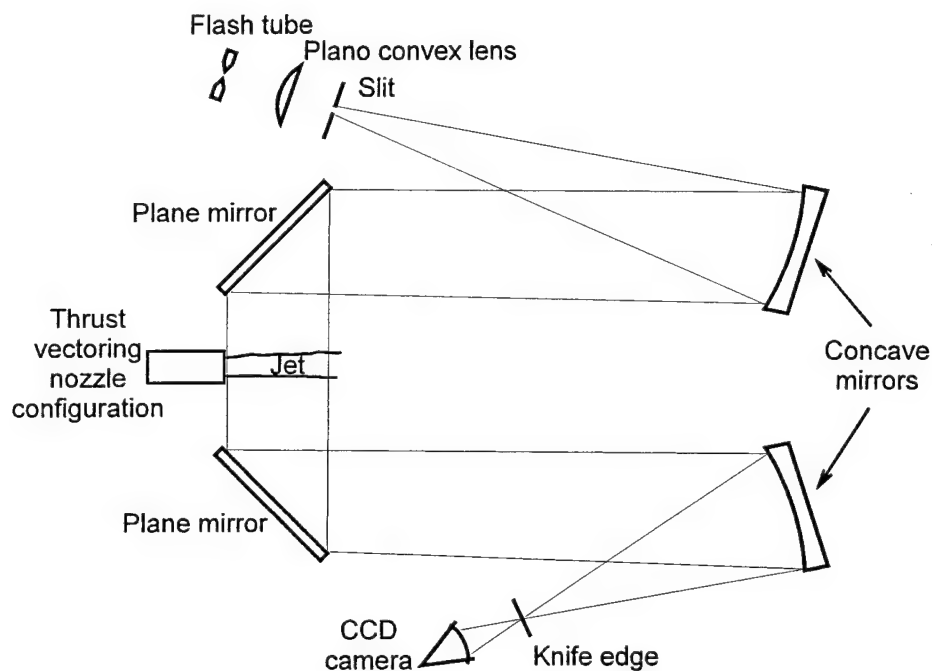


Figure 3.5: Schlieren setup

Particle Image Velocimetry

To obtain Particle Image Velocimetry data, the flow must be seeded with tiny particles. Aluminum Oxide is currently the tracer particle (which has an advertised particle size of $0.3 \mu\text{m}$) that is being used for the high speed experiments. The application of PIV to supersonic flows has been done in the past, showing good agreement with results from probe measurements (Wishart and Krothapalli, 1994),

with deviations being due to particle lag across shocks. Since this particular flow has counterflow being drawn from the ambient room air, it also needs to be seeded with particles. Tobacco smoke and water vapor (both having similar particle sizes as the Aluminum Oxide) was used to seed the ambient air near the nozzle (Figure 3.6). Water vapor tends to have somewhat higher signal to noise ratios, most likely due to the fact that the tiny droplets are spherical and scatter the laser light more effectively than the tobacco smoke. The laser light sheet is generated using a Lumonics

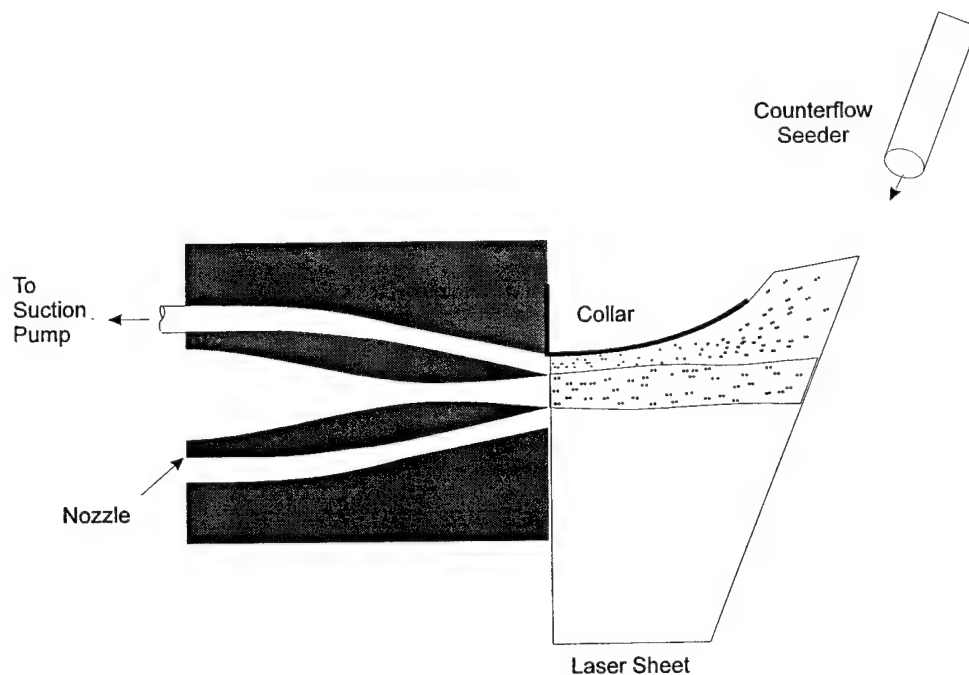


Figure 3.6: Seeding the counterflow

HyperYAG double pulse laser model HY1200 (250 mJ/pulse) and typical sheet forming optics. Figure 3.7 shows the PIV setup that is used for all experiments (the figure shows a rectangular nozzle without the collar). For the thrust vectoring experiments, only the plane containing the small dimension is needed to measure the

vectoring angle and velocity ratio within the collar. Free jet PIV images were taken without the collar present to study the flowfield of the rectangular jet. Images were captured for the Mach 2 free jet being operated at ideal and off design conditions along both center planes (containing the long and short dimensions). The double pulsed laser allows for variance of the time between the double pulses. A delay of $0.63 \mu\text{s}$ was used for the free jet and the thrust vectoring experiments. The time is set according to the characteristic flow velocities and the amount of shift required, which depends on the maximum magnitude of the velocity in the negative streamwise direction (Ross, 1993).

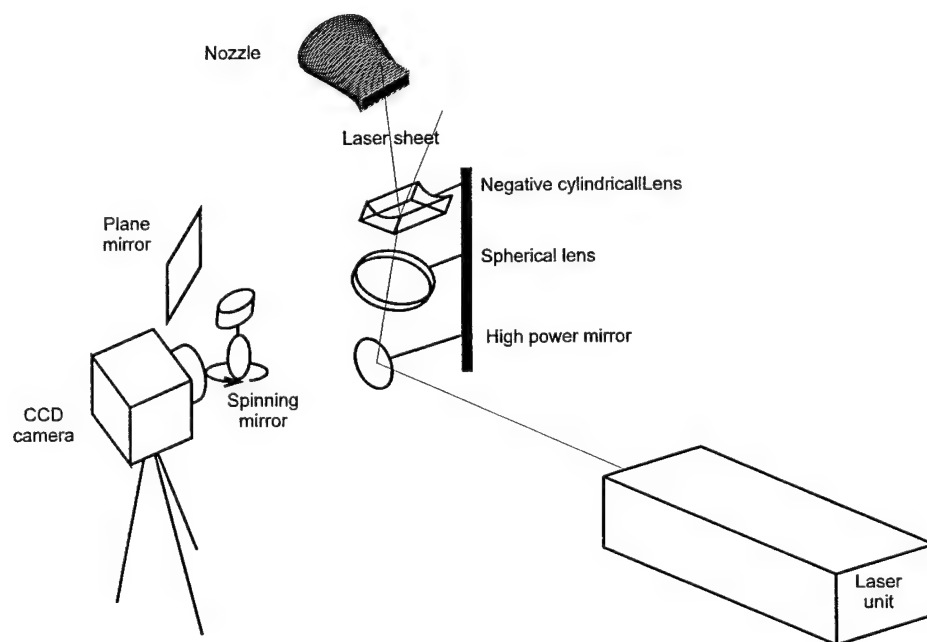


Figure 3.7: PIV setup

The Mark III PIV software from FFD uses auto correlation of the image intensity within a small region to calculate the average particle displacements. The method

has the disadvantage that it is directionally ambiguous. In order to get the direction of the displacement, an artificial shift must be added. The shift is introduced through the use of a spinning mirror that shifts the entire image downstream. The mirror is controlled by an FFD controller which also triggers the laser. The delay of the mirror is set so that the laser fires when the spinning mirror is at an angle of 45° to the camera (as viewed from above). A plane mirror is used in combination with the spinning mirror to reflect the flow images into the camera. Mirror speeds for the experiments were 120 and 140 revolutions per second for the free jet and thrust vectoring, respectively. The shift can be calculated by taking several images of seeded stagnant fluid, and processing the images on the PIV software. Once known, the software then subtracts off the shift from the net displacement, the result being the displacement due to the fluid motion.

Pressure Measurements

In addition to the PIV data, total and static pressure cross-stream profiles were acquired in the central plane containing the short dimension at different streamwise locations for three cases; the free jet at ideally expanded conditions, the nozzle with collar but no suction applied, and the nozzle with collar and suction set for a thrust angle of approximately 10° . A Validyne variable reluctance differential pressure transducer model DP15 is used to measure the pressures. The transducer is operated by a Validyne high gain demodulator board model CD19A which is plugged into a Validyne module case MCI-333. The probe location was controlled by a Parker Hannifin Corporation three axis traverse, motor drivers, and controller.

CHAPTER 4

RESULTS

The experimental objectives were broken into two parts. Part one consists of studying the flow generated by the Mach 2 nozzle in a free jet configuration. The nozzle was operated at design and off design conditions. The flowfield characteristics of the free jet operating at these conditions will be described and compared. Part two of the experiment dealt with the nozzle in a counterflow thrust vectored configuration as described in chapter 3. Flow characteristics of the thrust vectored jet will be studied, and comparisons will be made to the free jet results.

The chapter begins with a short discussion of the operating conditions of the nozzle for both parts of the experiment. This will be followed by a presentation of the Particle Image Velocimetry results for the free jet experiments. The following two sections will describe the thrust vectoring experiments with schlieren flow visualization images and PIV velocity fields. In addition to PIV data, total and static pressure measurements were taken. It will be shown that the velocity as calculated by the pressure data and the PIV results will agree quite well. Shear layer dynamics of the free jets will be presented including growth rates as well as velocity profile similarity. Shear layer growth of the thrust vectored jets will be investigated to explore the role of counterflow and curvature.

Nozzle Operation

The Mach 2 rectangular nozzle was operated under a variety of conditions. The free jet experiments consisted of operating the nozzle at jet stagnation pressures of 100, 115 and 130 psia (corresponding to NPR values of 6.80, 7.82, and 8.84) resulting in over, ideal, and underexpanded conditions. The temperature ratio (T_o/T_{exit}) is equal to 1.8. The density ratio is 0.56 assuming that the jet is ideally expanded (the static pressure in the jet exit plane is equal to the back pressure). The stagnation temperature of the jets were kept between 60 and 70°F, which was near that of the ambient. Using the dynamic viscosity of the jet (as found from the calculated static temperature) and the jet height H as the length scale, the Reynolds number of the ideally expanded jet is found to be 1.28×10^6 . Assuming that the secondary velocity is zero (for the free jet), the convective Mach number is 0.86. Since the convective Mach number is relatively large, such that compressibility plays a strong role, the structures in the shear layer are expected to be three dimensional. A planar laser light sheet (PLS) illumination of the span of the long dimension shear

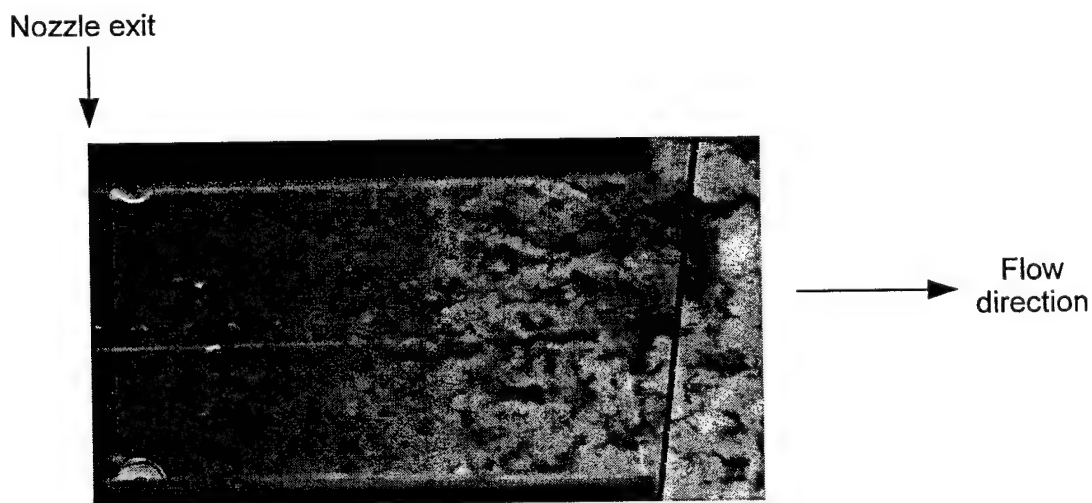


Figure 4.1: PLS image of the span of the long dimension Mach 2 jet shear layer

layer is shown in Figure 4.1 (the collar surface is in the background). The light patches in the image are caused by the scattering of the laser light by the water condensation in the shear layer which occurs when the moist ambient air mixes with the cold jet. As can be seen from the image, the structures appear to be three dimensional. This is expected since the convective Mach number is 0.86, which is large enough so that compressibility leads to three dimensionality (Clemens and Mungal, 1992).

Free Jet Particle Image Velocimetry Results

Particle Image Velocimetry was used to measure instantaneous velocity fields of the Mach 2 rectangular jet operating at various conditions. The measured pulse separation of the double pulsed laser was 0.63 μsec . The artificial shift induced by the spinning mirror was measured by processing shift images of stagnant seeded air. Multiple shift files were processed in order to determine the steadiness of the shift. The average shift was found to be 5.12 pixels, with a standard deviation of .09 pixels. Average displacements for the flow in the potential core of the jet were approximately 11 pixels. For a 95% confidence level, the mirror shift was held within 4% of the average shift. This leads to a maximum bias error in the streamwise velocity component of 20 m/s for the free jet instantaneous flow fields. The error in the average velocity field is calculated using equation 3,

$$\bar{u}_{\text{calculated}} = \bar{u}_{\text{actual}} \pm \frac{2\sigma_{\text{calculated}}}{\sqrt{N}} \quad (3)$$

smoke while the jet is seeded with Aluminum Oxide. The particle pairs (showing the displacement between the laser pulses) can be readily seen. The jet seems to be expanding slightly downstream of the nozzle exit suggesting a slightly underexpanded condition. This is most likely due to the stronger waves produced by the parallel short dimension side walls of the nozzle interior. The cold jet has a low absolute humidity which leads to water condensation when mixing occurs between the cold jet and the humid ambient air. The condensed water droplets scatter the laser light causing a cloudy appearance inside the shear layer. This effect (as seen in Figure 4.2) is present in most of the PIV images and has been used by other researchers in our laboratory as a visual representation of the shear layer. The instantaneous velocity field corresponding to this image is shown in Figure 4.3. There are regions where the velocity can not be accurately extracted from the particle displacements because of low signal to noise ratios. Each image has regions of low signal to noise ratios, but when the averaging process occurs, most locations in the

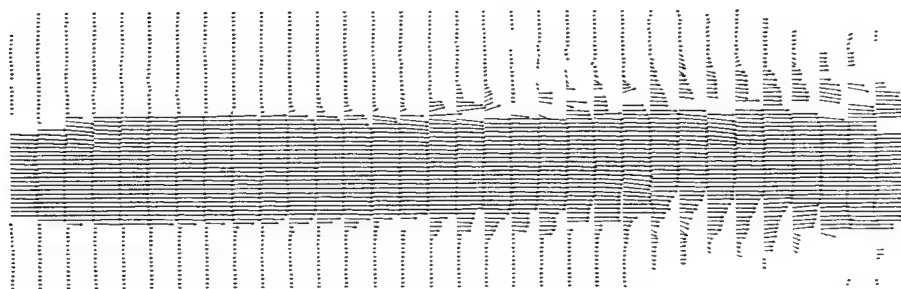


Figure 4.3: Instantaneous velocity field for the ideally expanded jet (short dimension)

flowfield have a sufficient number of samples that are used to calculate the average velocity. Some regions have consistently low signal to noise ratios, namely near the nozzle exit, where glare (due to the reflection of the laser light sheet from the nozzle) generates noise problems in the images. See the appendix for a spatial distribution of the number of data points used in the averaging process for the ideally expanded free jet. For the free jet cases, approximately 120 velocity data files were used to calculate the mean velocity field. Figure 4.4 shows the average velocity vector field for the ideally expanded jet (short dimension). As can be seen, the shear layers of

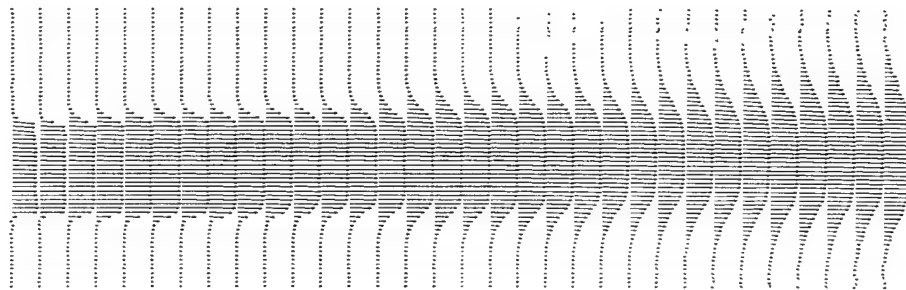


Figure 4.4: Mean velocity field for the ideally expanded jet (short dimension)

the jet are captured with fidelity. The potential core spans the entire streamwise length of the flowfield, as seen by the constant velocity region in the middle of each cross stream profile.

In order to ensure the two-dimensionality of the jet, the plane containing the long dimension of the nozzle must also be investigated. A typical PIV image of the ideally expanded jet in the long dimension is shown in Figure 4.5. The image shows that the shear layers in this dimension are relatively thin compared to the long

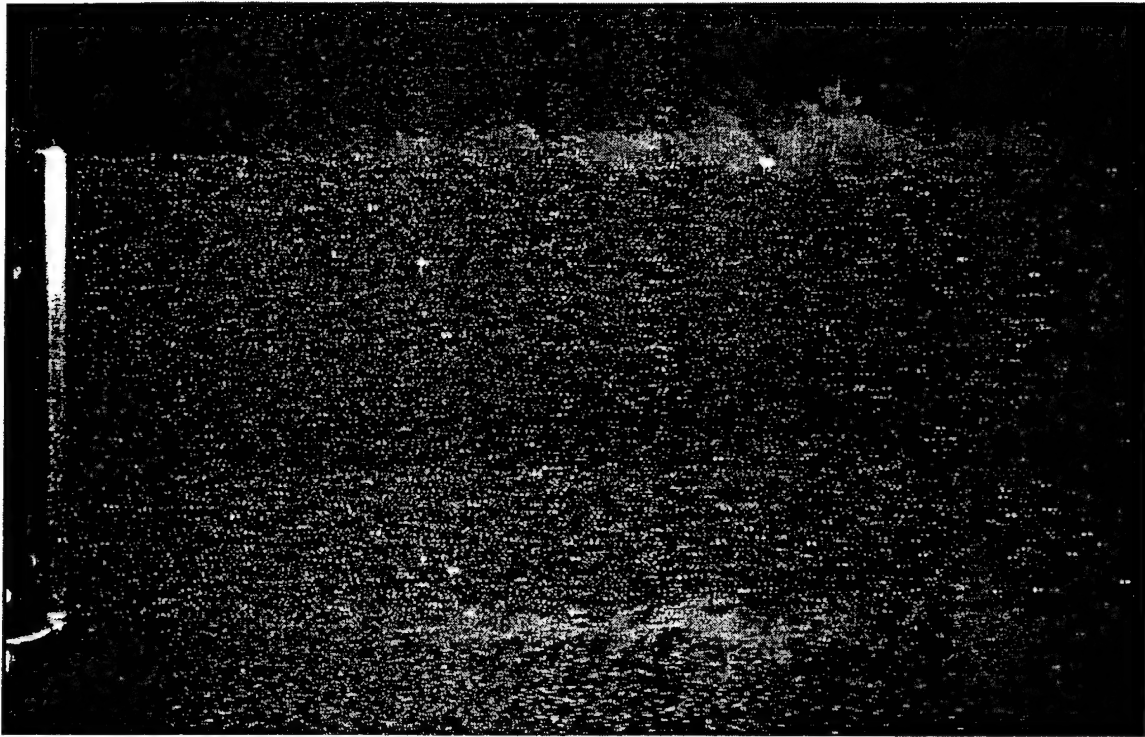


Figure 4.5: PIV image for the ideally expanded jet (long dimension)

dimension of the nozzle. The instantaneous velocity field which corresponds to the above image is shown in Figure 4.6. As can be seen, the instantaneous velocity profiles have a top hat shape.

As mentioned earlier, the holes in the velocity field near the nozzle exit are due to laser sheet glare from the nozzle. The mean velocity field for the long dimension of the ideally expanded jet is shown in Figure 4.7. The shear layer growth is seen to not extend too much into the core but skews toward the low speed side (growth into the core of the jet is minimal). Similar observations have been made for

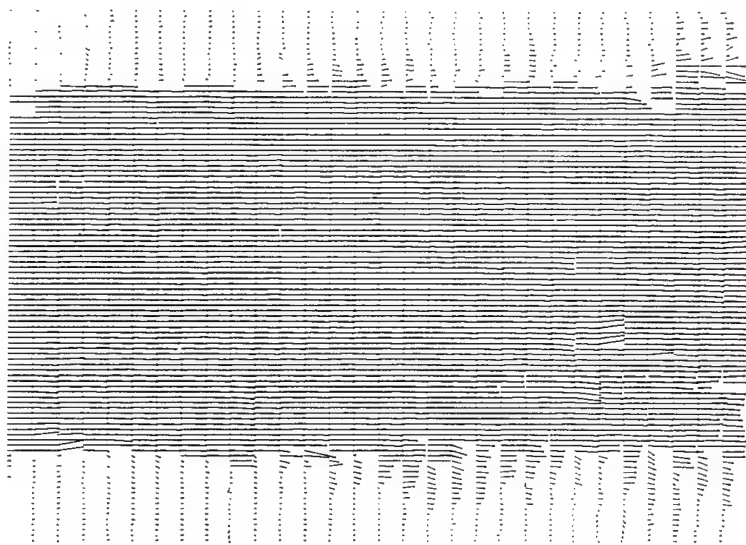


Figure 4.6: Instantaneous velocity field for ideally expanded jet (long dimension)

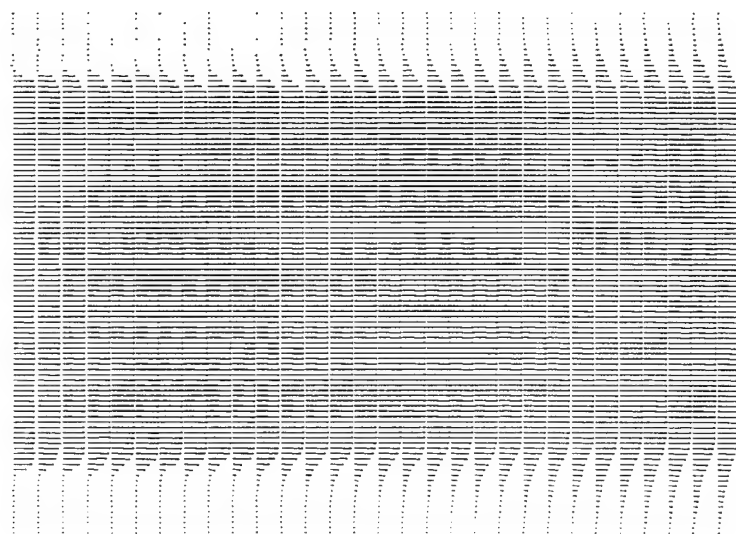


Figure 4.7: Mean velocity field for ideally expanded jet (long dimension)

axisymmetric jets (Wishart, 1995). The influence of the shear layers in this plane play a secondary role in the jet development as compared to the shear layers in the short dimension plane, as can be seen by the negligible effect the shear layers have on the potential core.

To investigate the behavior of the jet operating off design, PIV measurements were taken for over and underexpanded conditions. The nozzle pressure ratios (NPR) were 6.80 and 8.84 for the over and underexpanded flows, respectively. PIV images for these two flows are useful for identification of flow features such as flapping modes. The overexpanded jet PIV image in the plane of the short dimension is shown in Figure 4.8. The upstream portion of the overexpanded jet appears slightly thinner than the ideally expanded jet, due to the compression waves which result from the negative static gage pressure in the nozzle exit plane. A flapping motion of

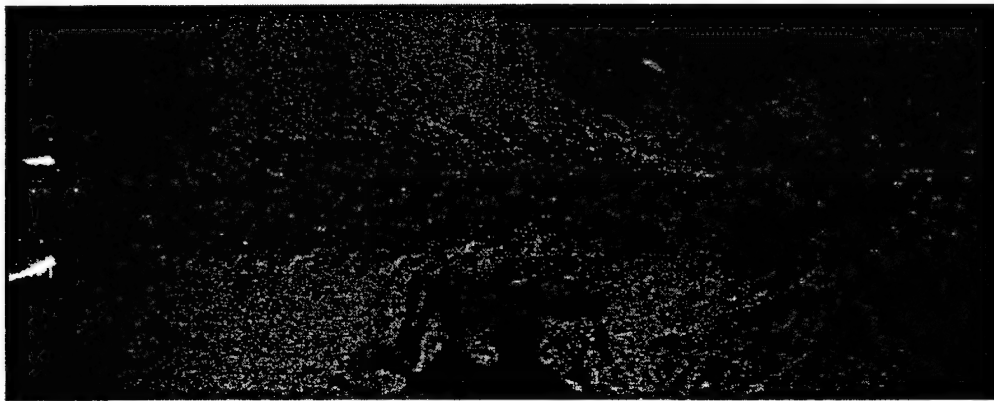


Figure 4.8: PIV image of overexpanded jet (short dimension)

the jet column can be observed in the photograph. As discussed by Krothapalli et al.

(1986), screech tones may be present for imperfectly expanded jets. In the presence of screech, the jet will have a strong flapping mode that is set up by the screech tone feedback loop. If the flapping is quite strong, the spreading of the jet can be enhanced. A high pitch discrete tone was heard during the overexpanded jet experiments. This flapping is seen to be quite violent and more dominant than the weaker flapping observed in the ideally and underexpanded PIV images.

The nozzle was also operated off design in the underexpanded regime ($NPR = 8.84$). The underexpanded jet is coupled to the thrust vectoring experiments because the application of suction lowers the back pressure on the suction side of the nozzle causing underexpansion on that side. The exit gage pressure is positive in this case, resulting in an expansion fan centered at the nozzle lip. Expanding of the jet near the nozzle exit can be seen in the PIV image of the underexpanded jet

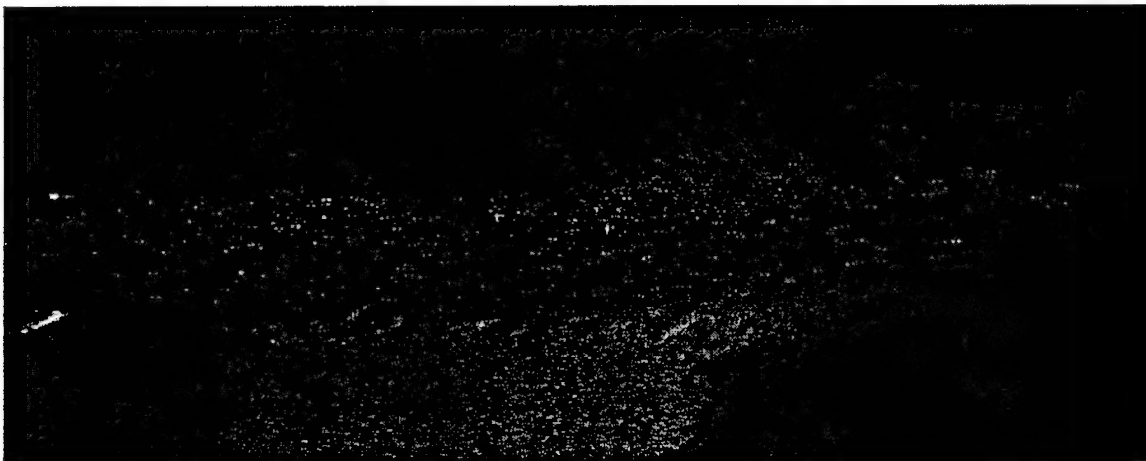


Figure 4.9: PIV image of underexpanded jet (short dimension)

(Figure 4.9). The underexpanded jet flapping is weaker compared to the overexpanded jet. Please see the appendix for mean velocity fields for the over and underexpanded jets, including both short and long dimensions.

In order to better understand the structural difference between the different jet flows, an iso-velocity contour is more insightful than vector plots. The velocity contour plot for the ideally expanded jet in the short dimension is shown in Figure

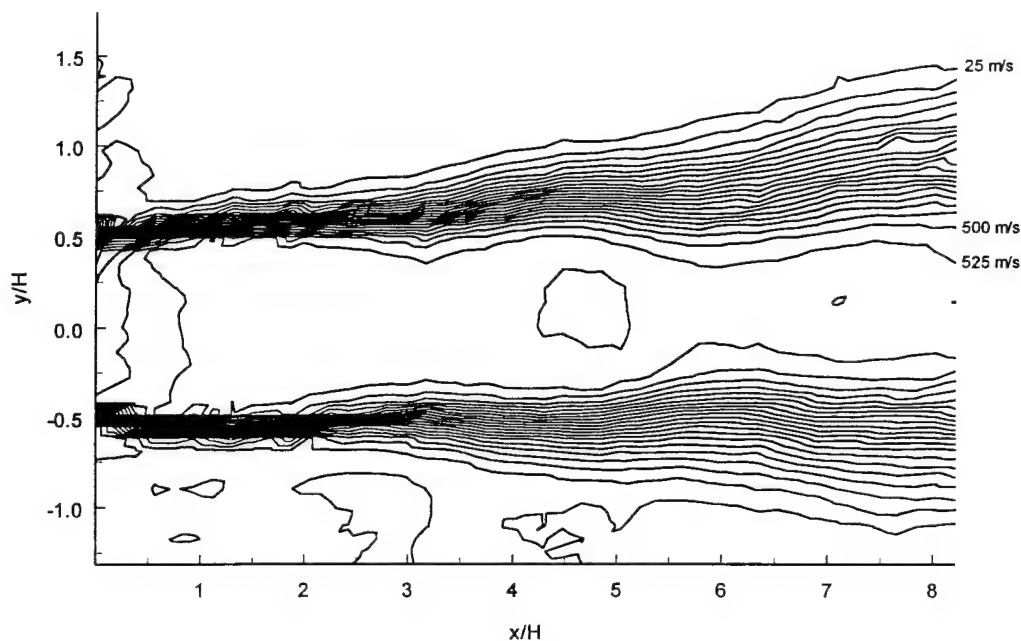


Figure 4.10: Iso-velocity contours for ideally expanded jet (short dimension)

4.10. The flow appears to be slightly underexpanded by the increase in velocity (and expanding appearance) near the nozzle exit. This effect is a direct result of the stronger wave system that is present because the short dimension walls of the nozzle are parallel (they are not contoured to avoid waves). As mentioned before, the shear

layer growth appears to be uniform, even though the location of the shear layer is displaced by the shock cells. There does not seem to be large velocity variations in the potential core region, which suggests that the shock cell structure consists of weaker waves. The iso-velocity contours for the overexpanded jet are shown in Figure 4.11. As observed in the PIV images, the jet width is slightly compressed in

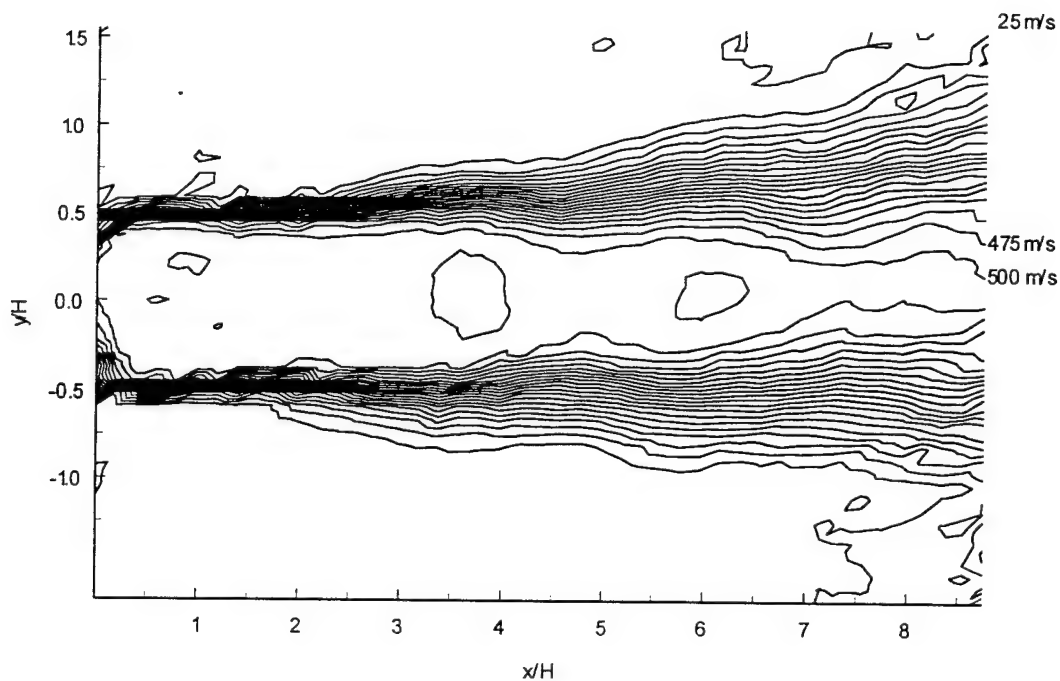


Figure 4.11: Iso-velocity contours for overexpanded jet (short dimension)

the near exit region (as compared to the ideally and underexpanded jets), although the effect is subtle. The compression waves due to the overexpansion appear to destructively interfere with the waves caused by the parallel short walls of the nozzle interior, resulting in an ideally expanded appearance in the initial region (from nozzle exit to about $3H$). The velocity inside the potential core is seen to go through regions

of high and low velocity, due to the stronger shock structure. The shear layers are seen to be vertically displaced by the presence of the expansion zones.

The underexpanded iso-velocity contour plot is shown in Figure 4.12. The expansion of the flow near the nozzle exit is manifested in bulging of the jet column followed by shock cells. The expansion (as represented by the increase in velocity),

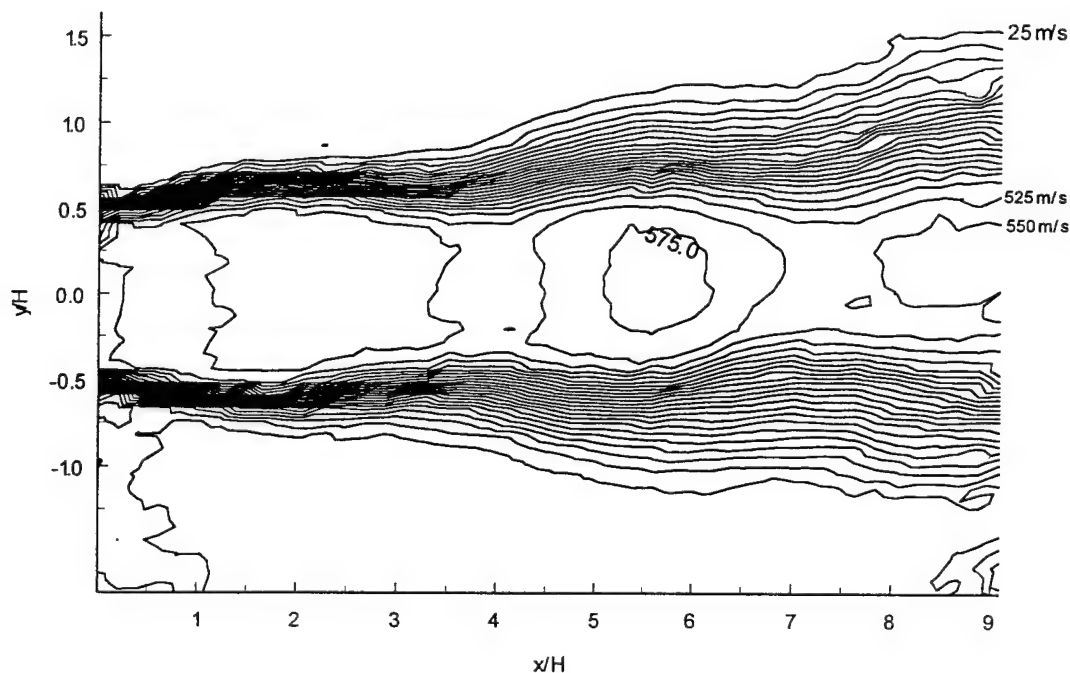


Figure 4.12: Iso-velocity contours for underexpanded jet (short dimension)

is shown to be particularly strong in the second shock cell. The potential core seems to be longer than that of a overexpanded jet due to the weaker flapping mode. The vertical displacement of the shear layers due to the shock structure is again present, and the effect of this on the shear layer growth will be discussed in a later section of

this chapter. The long dimension iso-velocity contours can be found in the appendix (Figures A.10, A.11 and A.12), it was found that the flow did not differ much in the long dimension except for the differences in the core region due to the shock cells.

In addition to the velocity contours, some additional characteristics of the shock structure can be identified in the centerline velocity profiles for the different jets (Figure 4.13). The centerline velocity varies over a larger range for the under and overexpanded jets than for the ideally expanded jet because of the presence of

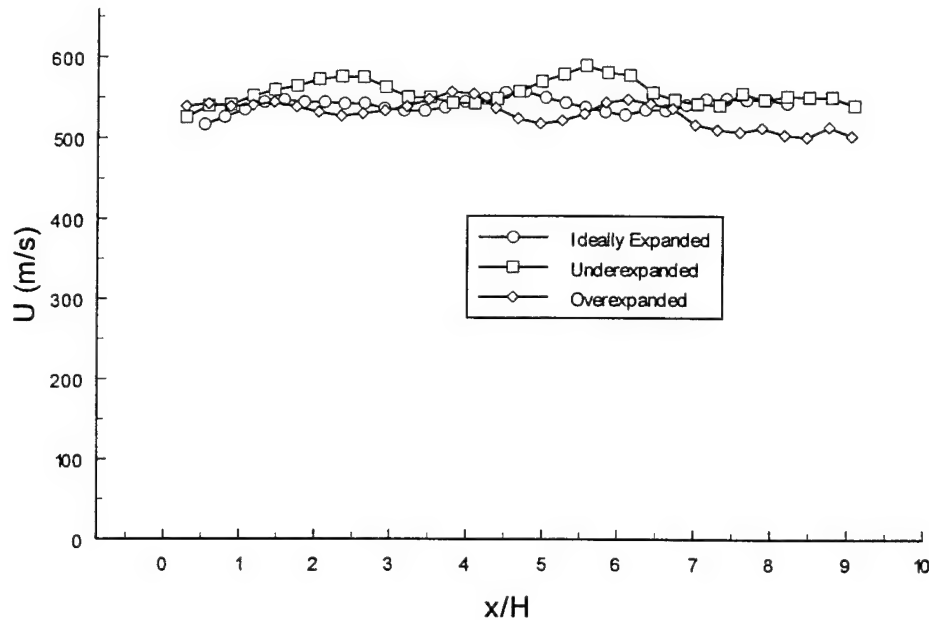


Figure 4.13: Free jet centerline velocity profiles

stronger shock cells. The velocity trends for the over and underexpanded jets are out of phase, as would be expected by the nature of the flow (overexpanded begins with compression while underexpanded begins with expansion). The spacing of the

centerline velocity peaks increases with increasing NPR, as has been observed in previous studies of axisymmetric jets (Wishart, 1995). As seen in the iso-velocity contours, the ideally expanded jet flowfield seems to have some of the same trends as the underexpanded jet, with lower variations of the velocity magnitude. The centerline velocity profile for the different planes (short and long) agree well for each condition (for ideally expanded jet, see appendix Figure A.13).

The structure of the jet at the ideal and mildly off design conditions is seen to be different in the core region due to the different shock cell structure. The effect of the shock cells on the shear layer growth of the jet will be discussed in a later section of this chapter.

Thrust Vectoring Schlieren Flow Visualization

Schlieren flow visualization images were taken for the heated thrust vectored jet with the top collar only. The stagnation temperature of the jet was approximately

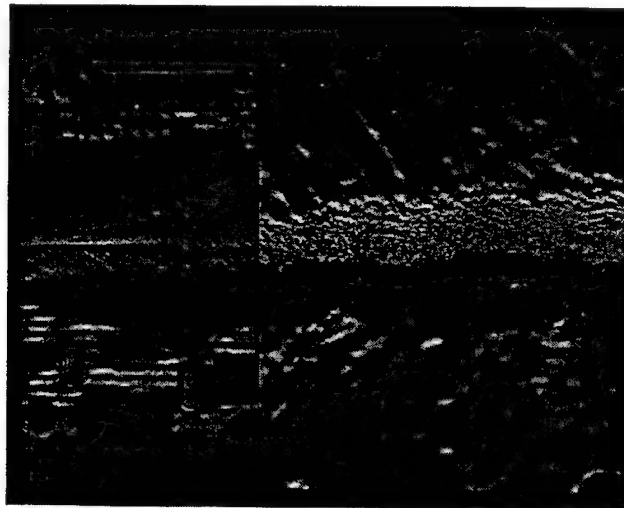


Figure 4.14: Schlieren image of the jet with no suction

700°F. The image of the jet with no suction is shown in Figure 4.14. The tubing along the top collar is connected to the static pressure ports along the collar surface to measure static pressure distributions (see Strykowski et al., 1995). The image contains both the internal (within the collar) and external regions. As can be seen, the jet is unvectored, further support that removing the bottom collar has a minimal effect. The acoustic radiation from the jet in the near field is seen to consist of similar wavelength waves on each side. The schlieren image with low suction ($P_{\text{exit}} \approx -1.5$ psig) is shown in Figure 4.15. The jet appears to be slightly vectored. The external

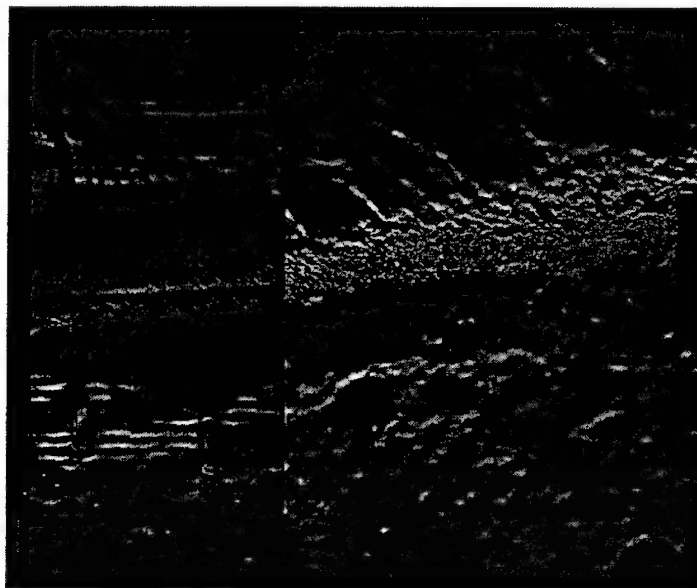


Figure 4.15: Schlieren image of the jet with low suction

region of the jet is straight, thus the turning occurs inside the collar region. An image for medium suction is shown in Figure 4.16. In this image, the upstream region of the jet seems to be expanding on the suction side just downstream of the exit. This is

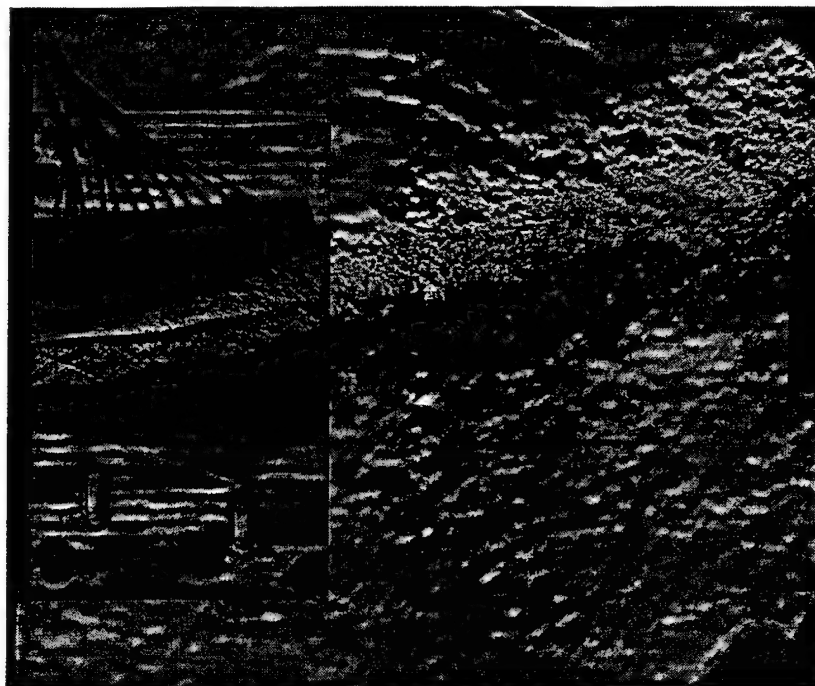


Figure 4.16: Schlieren image of the jet with moderate suction

due to the pressure mismatch on that side of the jet since the jet is being operated for ideally expanded conditions for a back pressure of 14.7 psi. Again the portion of the jet outside of the collar is seen to be quite straight. The jet does appear to be somewhat thicker, which would suggest that the application of counterflow enhances mixing. The acoustic waves being radiated from the suction side appears to have a shortened wavelength. This effect may be connected to the fact that the structures in the shear layer are moving at a lower convective velocity. The effect of counterflow on the acoustic field has yet to be understood. See King et al. (1995) for a discussion on the effect of counterflow on supersonic jet noise. The maximum suction case schlieren image is shown in Figure 4.17. The jet is being vectored at the highest angle possible with the given collar geometry and suction system. The

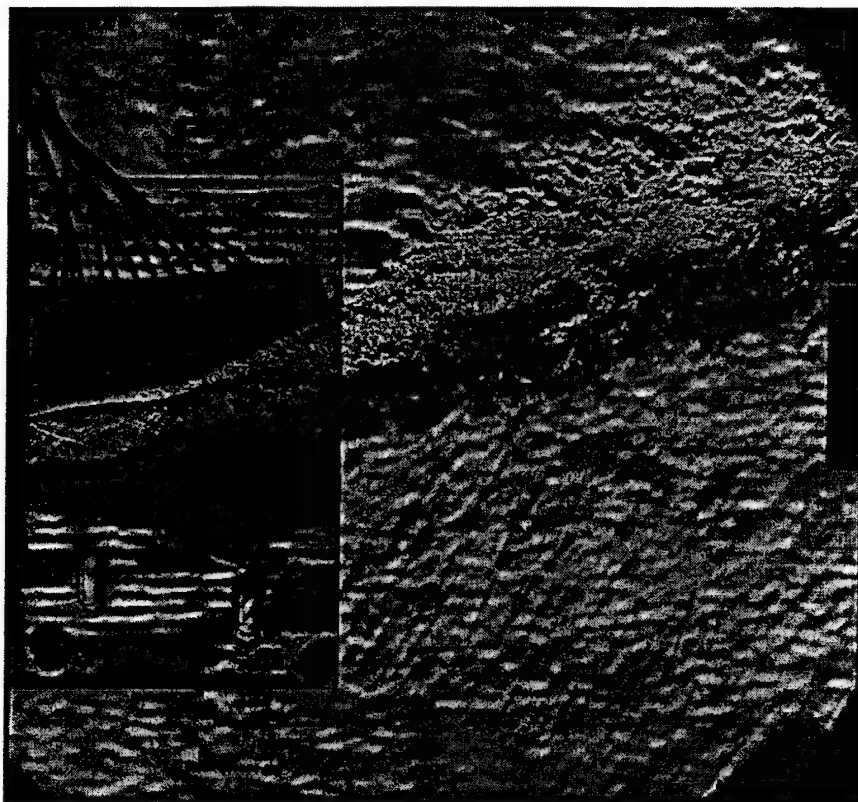


Figure 4.17: Schlieren image of the jet with maximum suction

visually measured vector angle is approximately 18° relative to the no suction jet. This angle is larger than that achieved with the cold jet. The difference is likely due to the fact that heated jets tend to spread faster (Wishart, 1995), thus the jet entrainment plays a larger role in creating a cross-stream pressure gradient. It appears as if the jet is actually attached to the collar in this image. A discussion of the attachment issues will be delayed until the next section of this chapter. The expansion in this case is more severe, as the pressure in the gap is lower, thus the effective NPR is larger (on that side of the jet). The length of the first shock cell is also seen to increase in these images as the suction is increased, again suggesting that the application of the suction is analogous to raising the NPR.

Bistability

One of the important issues with counterflow thrust vectoring is the phenomenon of bistability such as that observed in flip-flop nozzles. Although a complete study of this has not been done on the supersonic jet thrust vectoring, some interesting observations have been made when collecting the PIV and pressure data.

Before describing this phenomenon, a short discussion of the transient startup of the high speed jet facility is required. The stagnation pressure of the flow is increased from zero by adjusting the pneumatic control values. When the value begins to open, air begins to flow through the nozzle. With the one collar present, the jet will attach to the collar due to the Coanda effect during the beginning of the startup process. The jet will remain attached to the collar until the stagnation pressure is raised (by opening the valve) to approximately 85 psia, at this point, the jet will detach from the collar and obtain an unvectored state (assuming that the suction pump is not operating). The stagnation pressure of the flow is slowly raised to the desired value (115 psia for the ideally expanded Mach 2 nozzle). Once the desired flow conditions are achieved, the control valves maintain the stagnation pressure to be within 0.5 psi of the set value.

During the thrust vectoring experiments with no suction applied, different configurations were used. Initially, the tubes that connect to the suction system were blocked off such that no coflow due to the low pressure between the jet and the collar was allowed. During the startup, the jet attached to the collar as expected. The

stagnation pressure was raised all the way to the ideally expanded conditions, with the jet never detaching from the collar. The control of the jet was completely lost. The blockage of the suction manifold was removed, allowing for coflow to be induced by the jet. This configuration is analogous to an ejector. The startup of the jet with the manifold open had the attachment during the low stagnation pressure portion, but once the stagnation pressure was raised above approximately 85 psia, the jet detached from the collar. Once the facility reached steady state, the manifold was blocked off. The jet remained detached from the collar and appeared to have no vector angle. This observation suggests that for the given geometry, the jet is bistable. The issue is whether the suction pump can make the jet attach. As seen from the thrust vectored schlieren images, the jet under maximum suction appears to be very close to the collar surface. But the control of the jet was never lost, a slight decrease in the suction causes the jet to move away from the wall.

To further explore the bistable nature of this configuration, the gap height G was lowered to 3.5 mm ($G/H = 0.27$). When sufficient suction is applied, the jet attaches to the collar. If the suction is reduced, the jet still remains attached, and the pressure within the collar in the exit plane remains at approximately -6.0 psig. This is much lower than that achieved by the 5 mm gap experiments ($P_{\text{exit,max}} = -4.3$ psig). Removal of the suction puts the jet in a very chaotic mode. The jet randomly switched between being attached to the collar and separating and obtaining an unvectored state. This effect is not observed when the gap G is 5 mm. This simply means that the jet is not attached in a bistable manner when the gap G is 5 mm. If a stronger suction pump is used and losses in the manifold are reduced, it would most

likely be possible to put the jet in a bistable mode. This needs to be further explored, since the attachment behavior causes the jet to violently attach and detach from the collar in a very chaotic manner, resulting in a loss of control of the thrust angle.

Thrust Vectoring PIV Results

Particle image velocimetry measurements were taken for the thrust vectoring nozzle configuration as discussed in chapter 3. Three cases were done, with various levels of suction. The first case that will be analyzed will be when the collar is present and no suction is applied to the nozzle manifold. These experiments were first attempted with the counterflow manifold blocked off, but this caused attachment problems (see section on bistability in this chapter). The manifold was opened to allow for a secondary flow in the same direction as the primary jet flow, which is a result of the entrainment of the jet. In essence, the configuration is acting like an

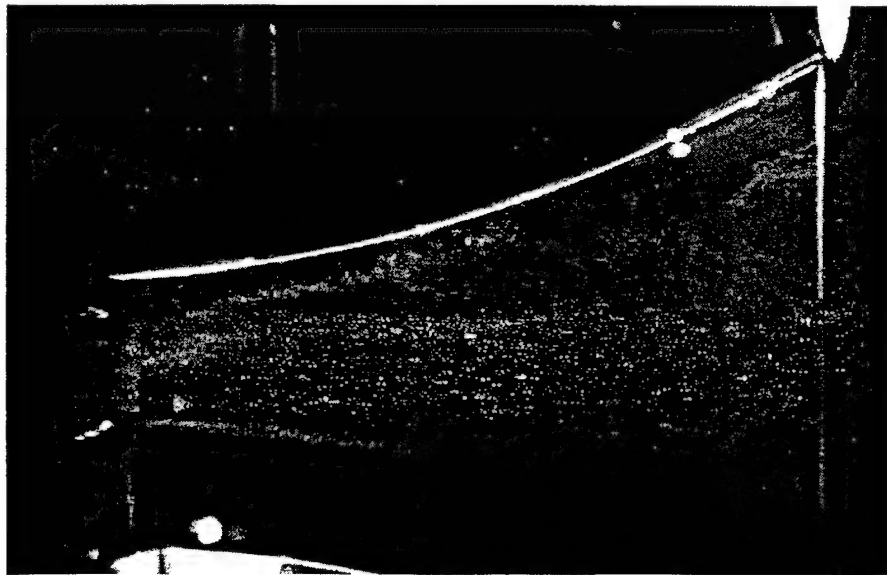


Figure 4.18: PIV image of unvectored jet

ejector. The collar exit pressure drops to -0.5 psig, due to entrainment of the jet (the jet entrainment is being constrained by the presence of the collar). A typical PIV image of this case is shown in Figure 4.18. The counterflow is seeded in the ambient region downstream of the collar. It is interesting to note that even though there is a coflowing stream generated through the suction gap, counterflow is induced between the collar and the jet. The smoke particles are evidence of this fact. The streamwise extent of the seeded air between the jet and collar gives an idea of how far upstream the counterflow is reaching. From the observation of several images, it appears that the counterflow reaches almost all the way up to the nozzle exit plane. This suggests that the secondary coflowing stream has a small mass flow rate, as compared to the counterflow. This is probably a result of a large pressure drop that occurs in the manifold, which has a sudden expansion type geometry. The image suggests that the presence of the collar has not caused any obvious vectoring effect. The particle displacements in the counterflow region near the nozzle exit have lower signal to noise ratios, which is caused by the water condensation which builds up on the Plexi glass in this region. This is one of the complications caused by the presence of the side plates. The shear layers also have lower signal to noise ratios, due to the much larger spatial velocity gradients and the attachment of Aluminum Oxide particles to the side plates in the shear layer region (these streaks can be seen in the image).

The mean velocity vector field for the unvectorized case is shown in Figure 4.19. On average, the counterflow does reach quite far upstream. The jet column behavior, as represented by the velocity field, suggests that the flow is operating near

the ideally expanded conditions. The nozzle is being operated for ideally expanded flow with a back pressure of 14.7 psi, and the collar static pressure only drops 0.5 psi

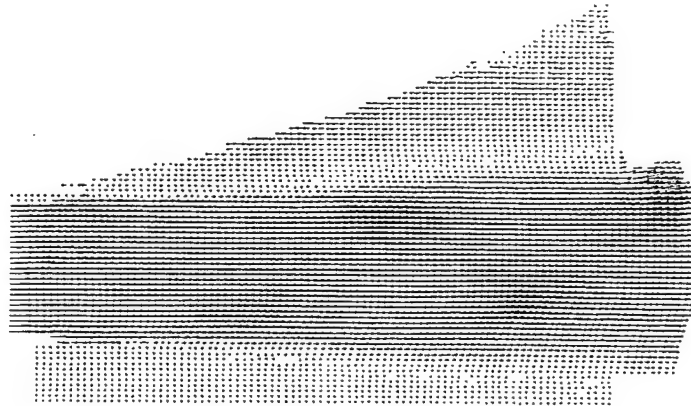


Figure 4.19: Averaged velocity vector field for unvectorized jet

below this value, the flow should be nearly ideally expanded on both sides. The core of the jet at the end of the collar has no noticeable vectoring angle. The shear layers appear to have relatively similar thickness' on the two sides, even though the upper shear layer has a larger velocity difference, which means higher vorticity levels are present.

To take a more quantitative look at the flow structure, iso-velocity contours are shown in Figure 4.20. When compared to the free jet case, the velocity magnitudes for this case are in good agreement with the ideally expanded free jet, as well as the shock cell center locations. The centerline velocity profiles (see Figure A.14 in the appendix) for the ejector and the ideally expanded free jet planes show

similar trends. These observations suggest that the presence of the collar has a minimal effect on the global flowfield of the jet.

To compare these results with the jet with suction applied, a case of mild vectoring was investigated. The choice of a moderate vectoring case is made because counterflow seeding becomes more difficult when the jet gets closer to the

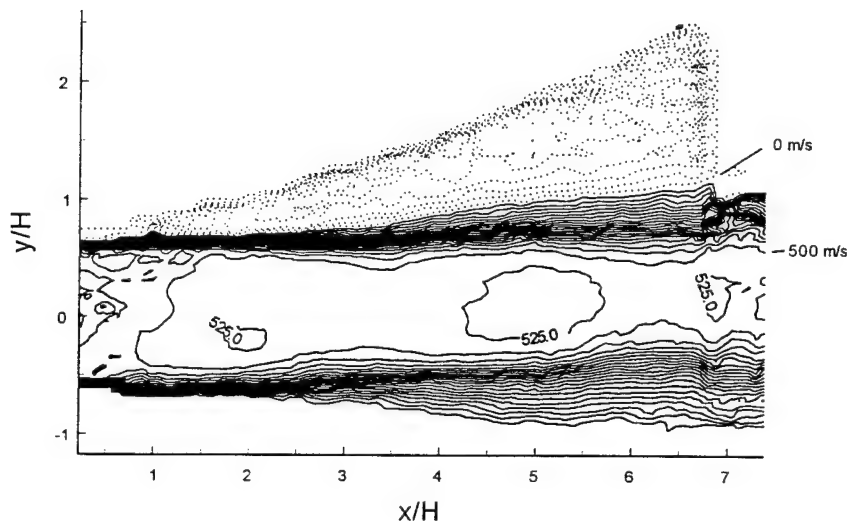


Figure 4.20: Iso-velocity contours of unvectored jet

collar (the highly vectored jet tends to entrain most of the seeded air while very little seed enters the collar region). Since an effective model for the thrust vectoring performance has been developed by Van der Veer (1995), we can predict the required static collar exit pressure to achieve a particular vectored jet angle. To obtain approximately 10° vectoring, the exit pressure was held to a value of -2.0 ± 0.1 psig. A typical PIV image is shown in Figure 4.21. The jet is observed to be slightly vectored near the downstream region of the image. The particles in the counterflow

region are more distinct than in the unvectorized case. This is due to the fact that seeding of the counterflow with water vapor was attempted midway through data collection, and it was found that the particle images were more intense in the

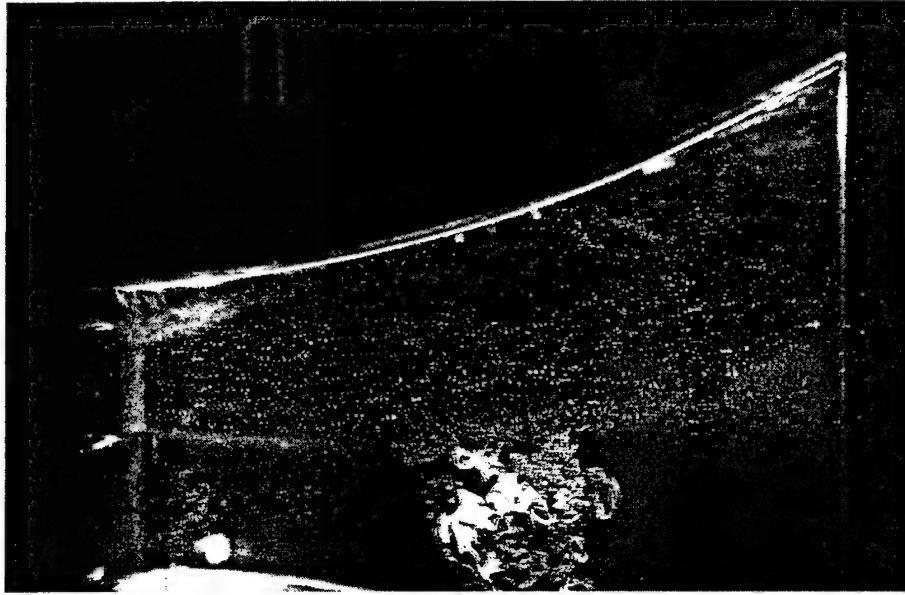


Figure 4.21: PIV image of moderate vectoring case

counterflow region. This is due to the fact that the water droplets scatter light better than the tobacco smoke.

The average velocity vector field for the moderate vectoring case is shown in Figure 4.22. The counterflow velocity in the nozzle exit plane is seen to be quite low, on the order of 10% of the jet exit velocity. The expansion of the upper half of the jet can be seen in the mean flowfield. The turning of the velocity vectors appears to occur over discrete lines, which suggests the presence of waves. The first wave of vector turning is seen to emanate from the top lip of the nozzle, and travel downstream and across the jet. Since the vectors are turning away from the wave, and because of the

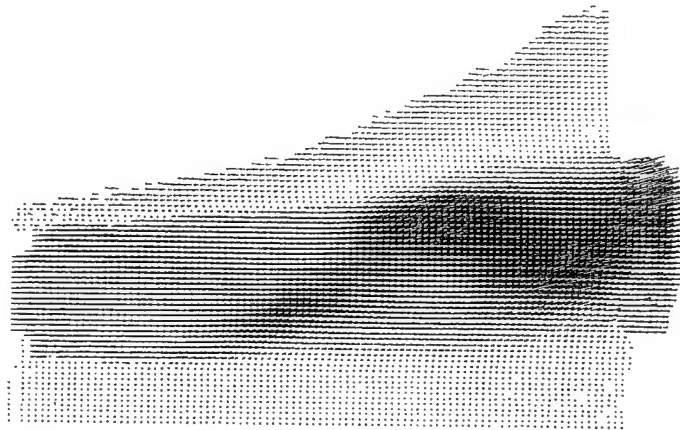


Figure 4.22: Averaged velocity field for moderate vectoring case

lower pressure on the top side, the first wave system is an expansion fan. This expansion fan is quite weak, using the angle of turning as a strength indicator. This wave reflects off the lower shear layer as a compression wave and passes across the jet core. Interestingly, the turning angle of the velocity vectors across this wave system is larger. Most of the turning appears to be occurring at this location, and just downstream. Such asymmetric wave structures are due to the asymmetric expansion conditions the jet is being operated under.

The iso-velocity contours for the moderate vectoring case are shown in Figure 4.23. the shock cells are centered at about $2.5H$ and $5.5H$ downstream of the nozzle exit, which agrees well with that found in the underexpanded free jet case. There is substantial thinning of the potential core near $3.5H$ due to compression waves.

In addition to the cases discussed above, a case for maximum suction was studied. This will correspond to the maximum vector angle for the given geometry. The strongly vectored jet will be closer to the collar surface, which complicates the

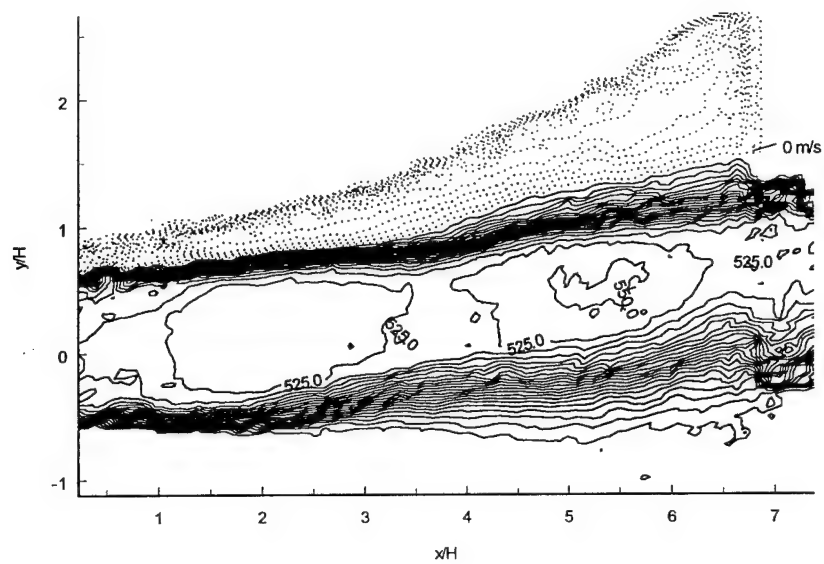


Figure 4.23: Iso-velocity contours for moderate vectoring

seeding of the counterflow. The suction system bleed off valve is shut completely, which results in a collar exit pressure of -4.3 psig. Figure 4.24 shows a typical PIV

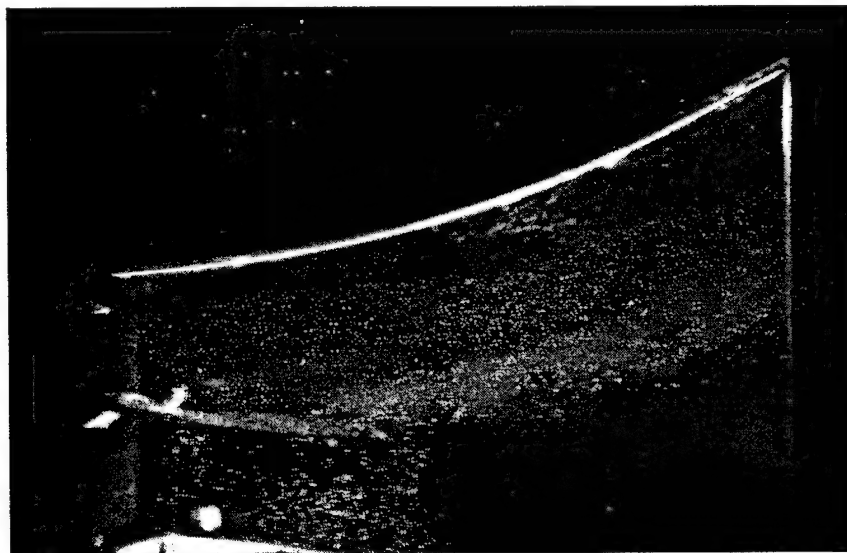


Figure 4.24: PIV image of maximum vectored jet

image for the maximum suction condition. The figure shows that the jet is being strongly vectored, as the jet appears nearly parallel to the collar surface. The level of underexpansion is now quite high, with an effective NPR of 11.0 using the collar sidepressure in the nozzle exit plane. Some bulging in the top region can be observed in the image as a result of the expansion. The average velocity vector field is shown in Figure 4.25. This average field has been calculated with approximately 60 instantaneous velocity fields, with lower signal to noise ratios in the top shear layer

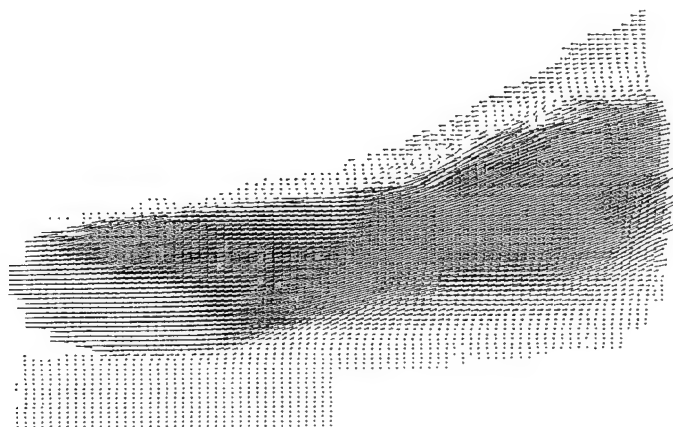


Figure 4.25: Average velocity vector field for maximum vectored jet

due to the seeding difficulties mentioned earlier. The average flowfield shows strong indication of asymmetric shock cell structure, as shown by the turning behavior of the velocity vectors. The waves emanating from the top lip of the nozzle is obviously an expansion fan, as seen by the turning direction of the velocity vectors as they pass through the fan. The expansion fan reflects off the shear layer as compression

waves, as can be seen by the velocity vectors turning away from the wave. To take a more quantitative look at the flowfield, the iso-velocity contour plot is shown in Figure 4.26. More evidence of the first expansion fan is shown by the increase in

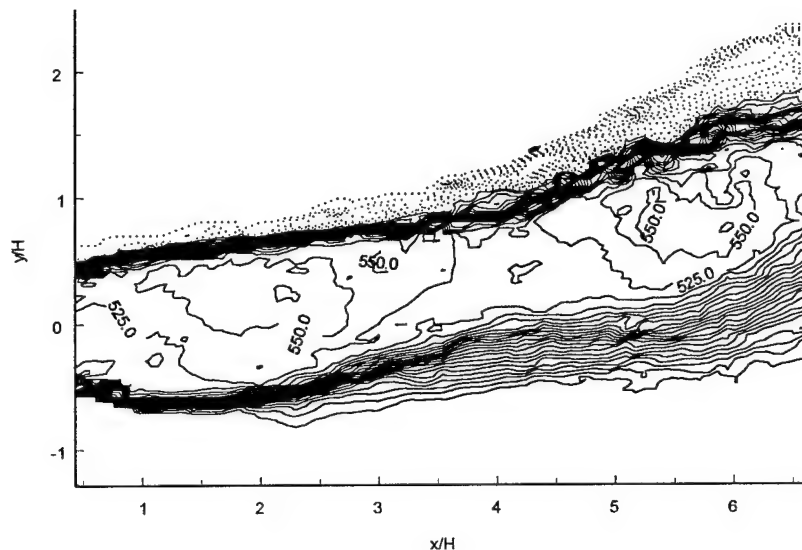


Figure 4.26: Iso-velocity contours for maximum suction case

velocity between 1 and 3H. The growth of the bottom shear layer also appears larger than of the counterflow shear layer, which is being constrained by the collar surface.

A better understanding of the shock structure can be derived by looking at the centerline profiles. The centerline axis for the vectored jets were chosen using the velocity magnitude contour plots previously shown, attempting to choose points in the middle of the jet core. The centerline velocity magnitude distribution for the three thrust vectoring cases is shown in Figure 4.27. Oscillations in the velocity magnitude are present showing the locations of the shock cells. As the suction is applied, the position of the peaks in the centerline velocity magnitude move downstream and

spread out, a similar trend noticed as that for free jets with increasing NPR. Thus the application of suction to one side of the jet has an effect of making the jet behave underexpanded with an increasing NPR. To help identify the location and type of

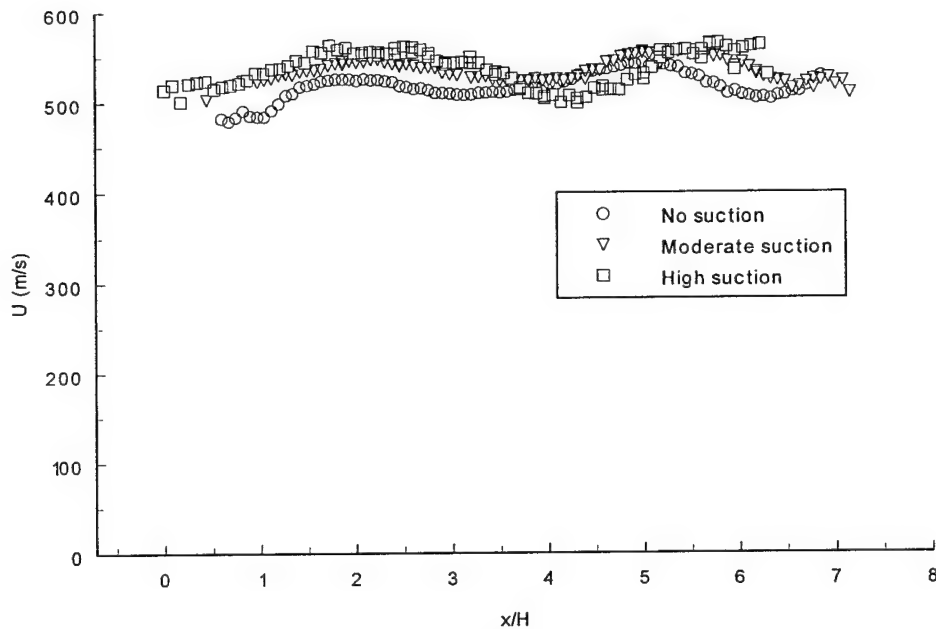


Figure 4.27: Thrust vectoring centerline velocity magnitude profiles

waves present in the flow, the velocity angle distribution along the centerline (same position in the flow as the velocity plot in Figure 4.27) is shown in Figure 4.28. The unvectored case shows that there is some vectoring present, approximately 1° , which is due to the pressure difference across the jet due to the lower pressure experienced by the top shear layer. Some interesting trends are noticed for the vectoring cases. For the moderate suction case, there is a decrease in the vector angle at about $2.5H$, and subsequent one at about $4.2H$. This is caused by the wave

system and particle lag in the flow. The curve for the maximum suction has a similar shape, with the dips in the angle occurring at 2.6 and $4.2H$. As the flow passes through the expansion fan, they gradually turn up (towards the fan). The turning is

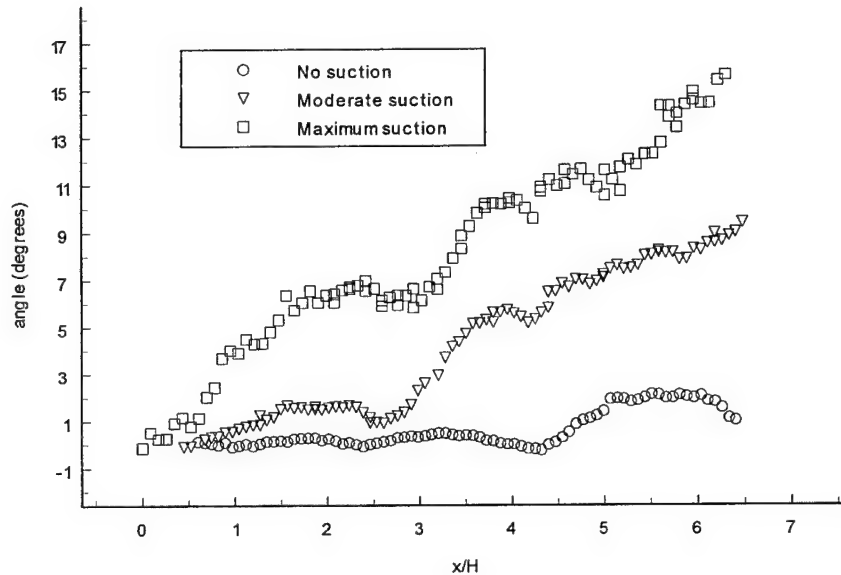


Figure 4.28: Centerline velocity vector angle for vectored jet cases

seen to be gradual. Near x/H equal to 3.4 , a sharper increase in the angle is seen to occur. This is the compression wave zone causing a more rapid turning of the flow. Using these results, the general shock cell structure can be visualized as shown in Figure 4.29. The shocks are similar as that found in an underexpanded jet, but asymmetric in nature. The first wave system consists of an expansion fan centered at the nozzle lip. The expansion fan reflects as a compression wave system. Just as found for underexpanded jets, the shock cells (now triangular instead of diamond) become longer when the suction is increased (which raises the NPR value).

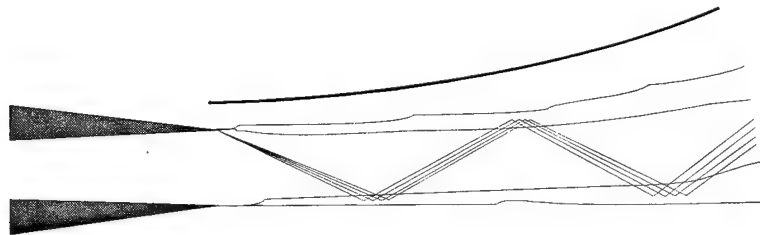


Figure 4.29: Thrust vectoring shock structure

Since the flow is compressible, the calculation of the thrust angle using control volume analysis becomes complicated. As a first approximation, the angle of the vectors in the core of the jet can be used. Of course, the velocity will have a weighing factor on the true angle of thrust. Hence, the thrust angle can be determined by looking at the higher speed portion of the flowfield. An average angle can be calculated at a particular streamwise location x/H , by averaging the angle of

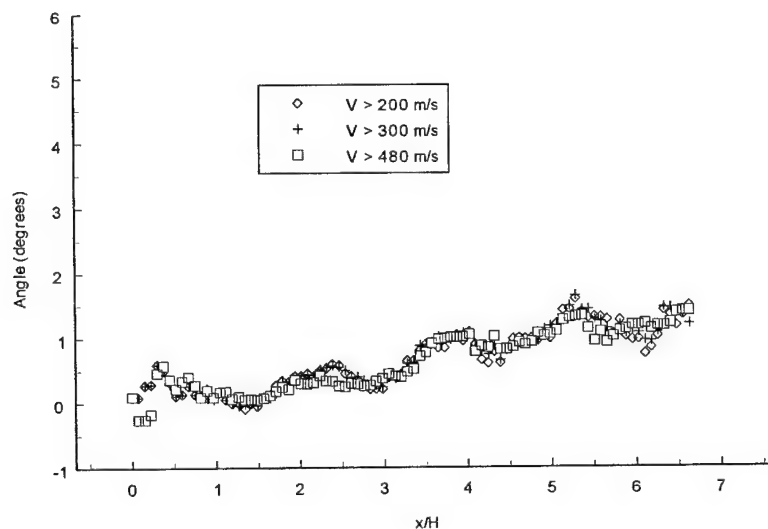


Figure 4.30: Thrust angle distribution for the unvectored jet

the velocity vectors that have a velocity magnitude above a set threshold level. Figure 4.30 shows the average angle distribution for the case without suction using this approach. The average angle at a particular streamwise location is calculated using velocity vectors that have a magnitude above a certain threshold value (200, 300, and 480 m/s were used in Figure 4.30). As this velocity threshold criteria increases, the thrust angle calculation is based more on the potential core. The curves collapse, showing an increasing angle with streamwise position. Similar curves for the moderate and maximum suction (see Figures A.15 and A.16 in the appendix) show the same collapsing trends. The jet at the end of the collar has an angle of about 1° which is due to the small cross stream pressure gradient that is caused by the presence of only one collar. The thrust angle distribution for the jets

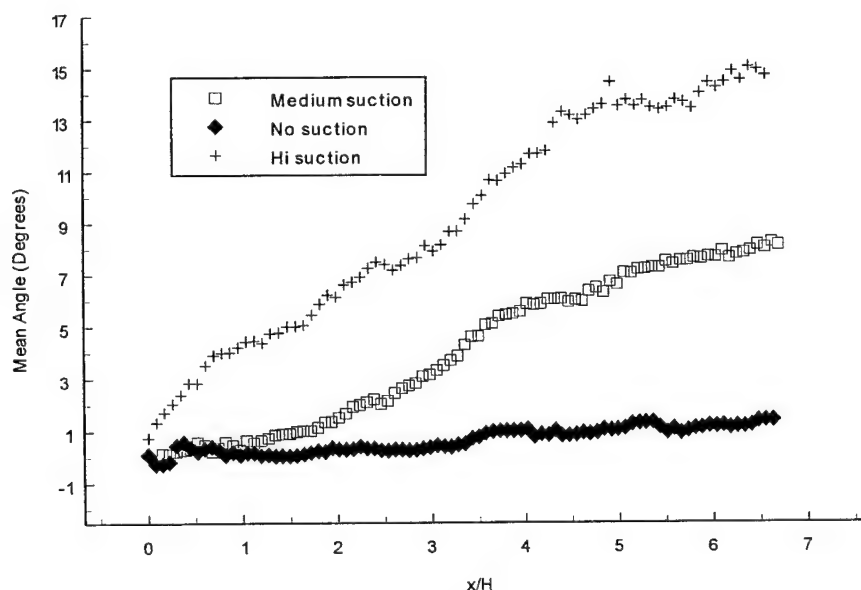


Figure 4.31: Thrust angle distribution for the vectored jets

with various levels of suction is shown in Figure 4.31. The thrust angle is seen to increase in a relatively linear fashion. The angle of the thrust for the moderate suction case appears to be about 8° near the end of the collar, while the maximum suction thrust angle appears to be about 16° , which can be increased by optimizing the geometrical configuration (G/H, L/H, etc.). Vector angles thus obtained are in good agreement with that of the flow visualization pictures.

Pressure Measurements

In addition to the particle image velocimetry measurements, static and total pressure data was collected for the ideally expanded free jet and thrust vectored jets. See the appendix (Figures A.26 through A.31) for the spatial pressure distributions of each case.

The presentation of the pressure measurements will begin with a discussion of the total pressures measured for the above mentioned cases. It must be reiterated that the pressure measured by a pitot probe in a supersonic flow is actually the total pressure behind the normal shock that forms in front of the probe tip. The stagnation pressure drop across a normal shock increases with increasing Mach number (as the shock becomes stronger). The cross-stream total pressure profiles (within the center plane including the short dimension) at the exit of the nozzle is shown in Figure 4.32. The collar is on the positive y/H side. The profiles have a top hat character as expected. The important result derived from this figure is that the

presence of the collar, and subsequent application of suction, has no effect on the thrust of the jet. The total pressure profile for the jet with suction applied has a

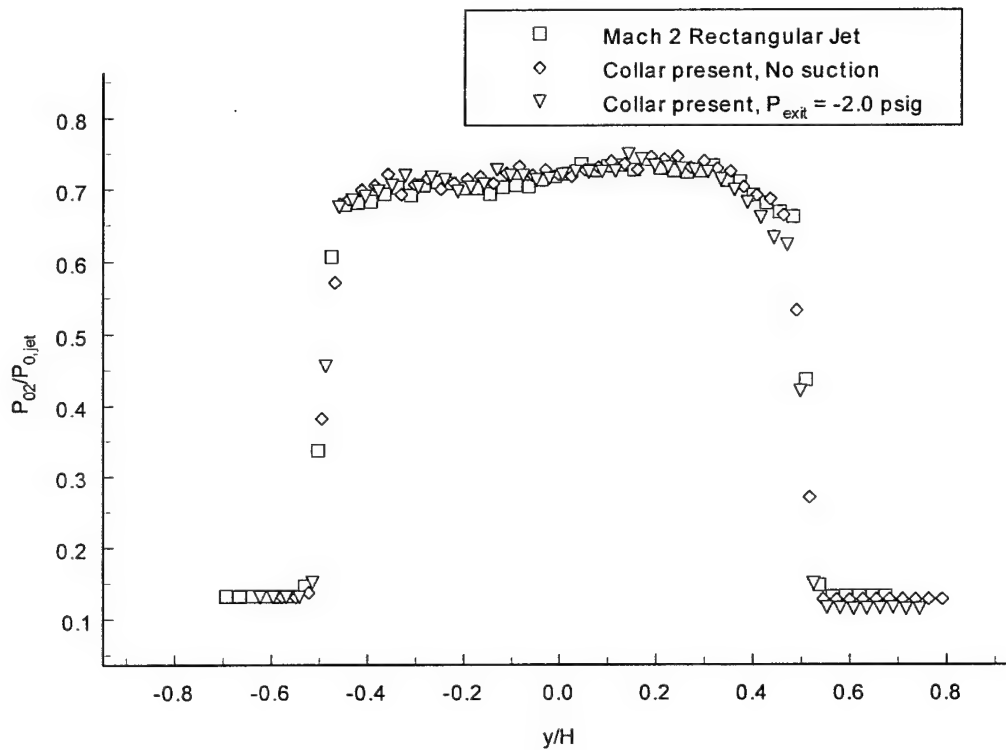


Figure 4.32: Exit total pressure profiles

slightly negative gage pressure measurement in the gap region because the probe is opposite to the flow and is influenced by the static pressure.

A comparison between the total pressure profiles of the various cases at different streamwise locations can give insight into the shock structure present in the flow. The cross-stream total pressure profiles at four different x/H locations is shown in the appendix (Figures A.32 to A.36). The profiles show that the vectored jet is shifted to the collar side.

Static pressure traverse profiles were taken for the three cases at various streamwise locations. See the appendix for spatial distributions of the static pressure measurements for the three different cases (Figures A.26, A.27 and A.28). In general, the profiles are quite irregular.

Similarity and Shear Layer Growth of the Free Jets

The previous sections dealt with the global flow features of the free and thrust vectored jets. Since the initial region of the jet plays such a large role in the overall jet development, a detailed analysis of the shear layer characteristics of the initial region will now be presented. All of the data is taken from the PIV investigation.

The development of the shear layers in the short dimension of the rectangular Mach 2 jet will dictate important flow features such as the potential core length. Streamwise velocity profiles for the ideally expanded Mach 2 jet (short dimension) is

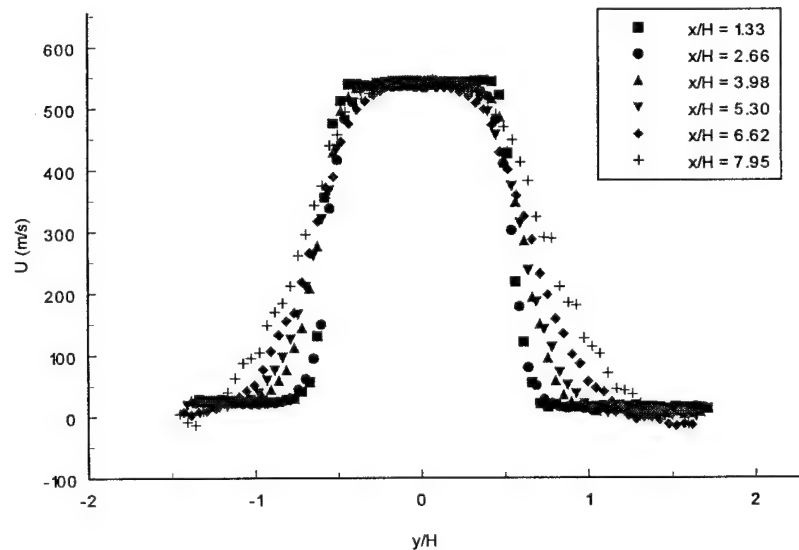


Figure 4.33: Ideally expanded streamwise velocity profiles

shown for various streamwise locations in Figure 4.33. The profiles near the nozzle exit have a top hat shape, with the shear layers becoming thicker with increasing x/H . The end of the potential core has not yet been reached, as can be seen by the flat velocity region near the middle of all of the profiles. The velocity profiles shown in Figure 4.33 suggest that the shear layers have a similar shape if plotted using an appropriate normalization. As discussed in chapter 2, the shear layer thickness can be defined in many ways. Since velocity and pressure data has been collected for these experiments, two methods can be used. The velocity shear layer thickness, δ_{vel} , is based on the distance between the locations where the velocity is equal to $U_1 - 0.05\Delta U$ and $U_2 + 0.05\Delta U$. A distribution of the velocity shear layer thickness as a

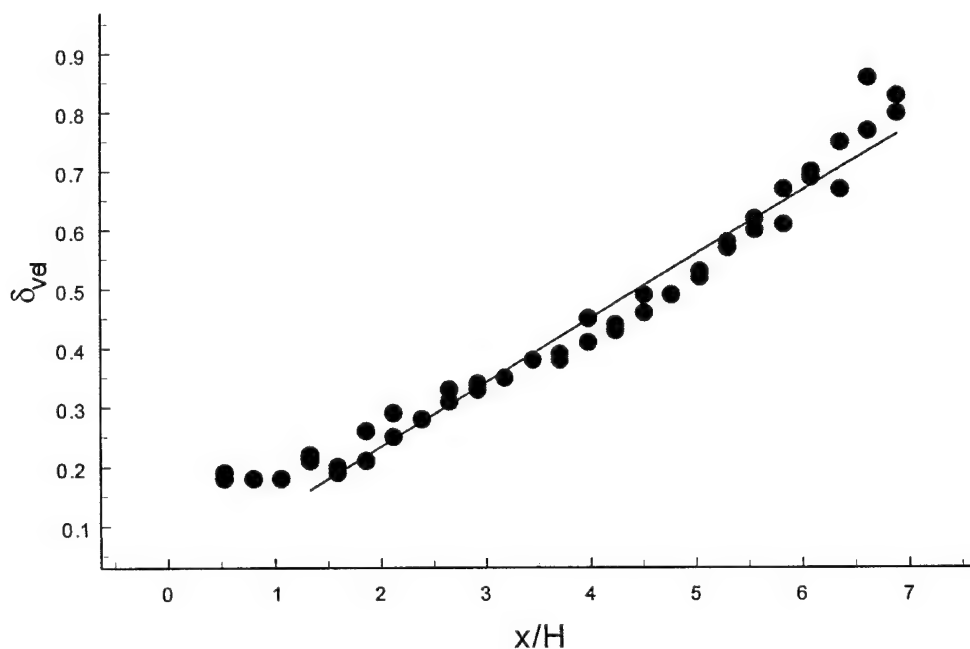


Figure 4.34: Velocity shear layer growth of the ideally expanded free jet

function of x/H for the ideally expanded jet is shown in Figure 4.34. The growth appears to be linear except for near the nozzle exit, where the shear layer is not fully developed and the thickness can not be accurately measured because of the scale of the image. Excluding these points, the growth rate of the shear layers for the ideally expanded jet is 0.11. The growth rate is slightly lower than that of a axisymmetric Mach 2 jet (Wishart, 1995). Comparing the growth rates of the Mach 2 jet under various operating conditions can give insight into the effect of the shock cell structure on the shear layer growth. There are slight oscillations that can be seen in the shear layer thickness distribution, which are likely due to the curvature induced by the shock cell structure. It can be seen that this effect is minimal. The stronger shock cells present in the off design experiments can effect the shear layer growth through the larger spatial variation of the velocity in the potential core as well as the shear layer curvature caused by the bulging and compressing jet. Operation of the nozzle in the overexpanded regime can lead to a strong flapping mode which enhanced the jet spreading rate. Figure 4.35 shows the shear layer thickness in the fully developed shear layer region for the over and underexpanded jets as well as the ideally expanded jet. It can be seen that the effect of the different shock-cell structure (in the mildly off design conditions explored in this study) has a minimal effect on the growth rate behavior of the jet shear layers. This conclusion agrees with the observations made for an axisymmetric jet (Wishart, 1995). Consequently, the vorticity levels for the different free jets have similar magnitudes (see the appendix for full vorticity distributions, Figures A.17, A.18 and A.19, as well as cross-stream vorticity profiles for the free jets in Figure A.20).

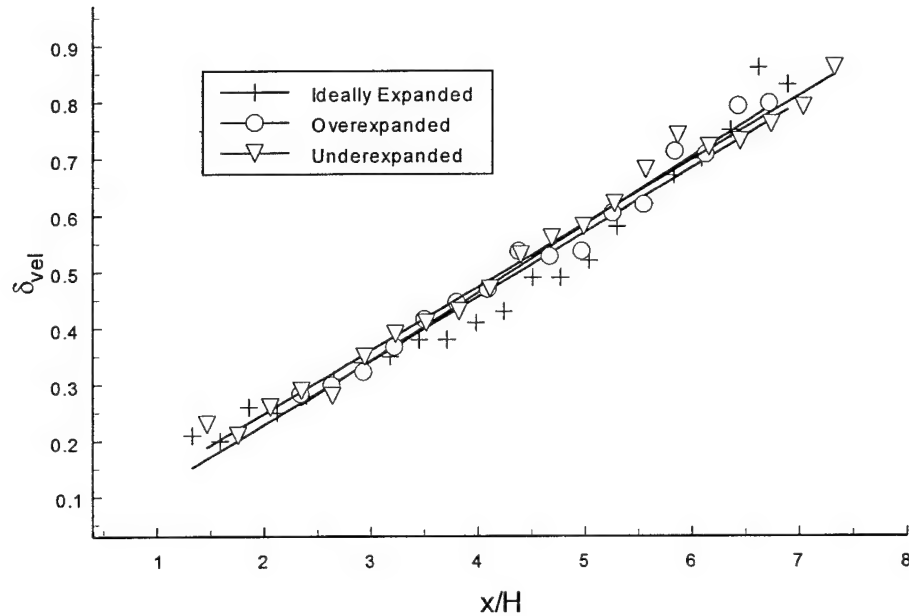


Figure 4.35: Velocity shear layer growth for the free jets

Although the growth rate is unaffected by the mildly off design operating conditions, the shape of the shear layer may be different. The similarity of the shear layer velocity profiles can be investigated by proper normalization of the streamwise velocity and cross-stream coordinate y/H . Since the location of the edges of the shear layer are known from the above mentioned convention for the velocity thickness, the location of the middle of the shear layer can be calculated. This point, called y_{mid} , is the middle of the shear layer and not necessarily the location where the velocity is equal to the average of U_1 and U_2 (i.e. the jet half width). A similarity variable can be formed by subtracting y_{mid} from y/H and normalizing by the velocity

shear layer thickness δ_{vel} , which is calculated from the linear behavior of the experimental data. The velocity normalization is chosen to be $(U-U_2)/(U_1-U_2)$ which forces the velocity to 1.0 on the high speed side and 0.0 on the low speed side. The similarity of the jet shear layers for the different operating conditions is shown in Figure 4.36. The velocity profiles collapse well for x/H greater than approximately 3.0,

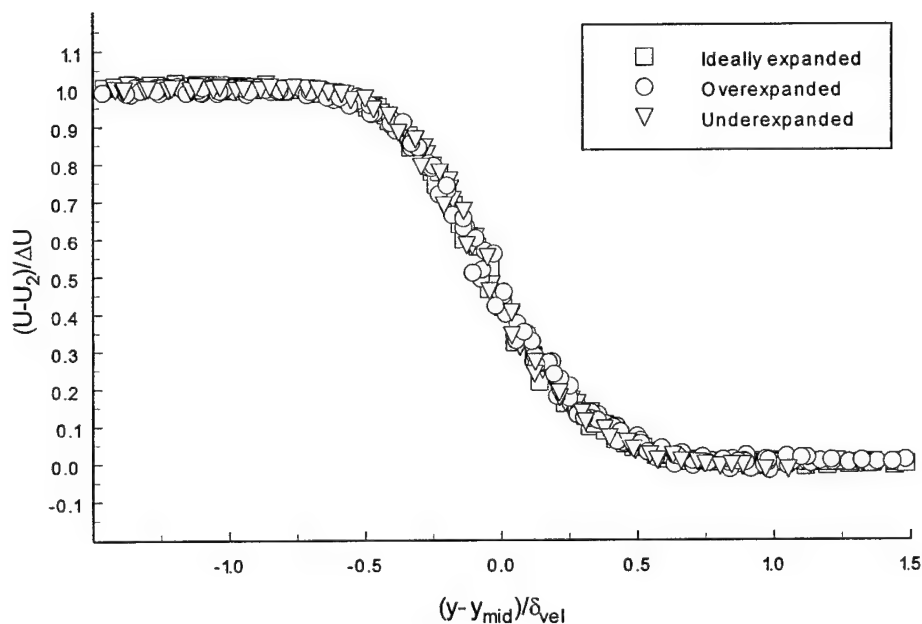


Figure 4.36: Free jet shear layer similarity

which suggests that the true location where the shear layers become fully developed is near $3H$. Some interesting things can be seen from this figure. First of all, the middle of the shear layer (where the spatial similarity variable is 0.0) is at a location where the velocity is somewhat lower than the average velocity of the two free streams. This differs from observations made for compressible planar shear layers

where the middle of the shear layer coincided with the location of the mean velocity (Goebel and Dutton, 1991). Additionally, the location of the maximum velocity gradient appears slightly shifted to the high speed side. The similarity curve can be used to determine the growth rate using a different velocity criteria, such as a 10-90% velocity difference for comparison with other studies. This growth rate, called $\delta_{10-90\%}$ is equal to approximately 0.08. This is substantially larger than the results for planar shear layers (Goebel and Dutton, 1991), and probably due to the difference in the similarity shape of the shear layer profiles as discussed above. Since the velocity profiles of these two flows appear to differ slightly, one must take great caution in choosing a shear layer thickness criteria and making comparisons with other studies.

One possible issue that may cause inaccurate growth rate measurements from the PIV data is particle slip. Velocity data can also be computed from pressure and temperature measurements. The Mach number can be calculated from the pressure measurements using Rayleigh's pitot formula in the supersonic region (see Liepman and Roshko, 1953) and the isentropic pressure relation in the subsonic flow region. Thus from total and static pressure profiles, Mach number profiles can be calculated (see Figure A.23 in the appendix for an example). The velocity can then be calculated if the stagnation temperature across the jet is assumed to be constant. Velocity profiles from PIV and pressure data for the ideally expanded free jet at $x/H = 4.9$ is shown in Figure 4.37. As can be seen, the agreement between the measurement techniques is excellent, suggesting that the PIV measurements accurately represent the shear layers.

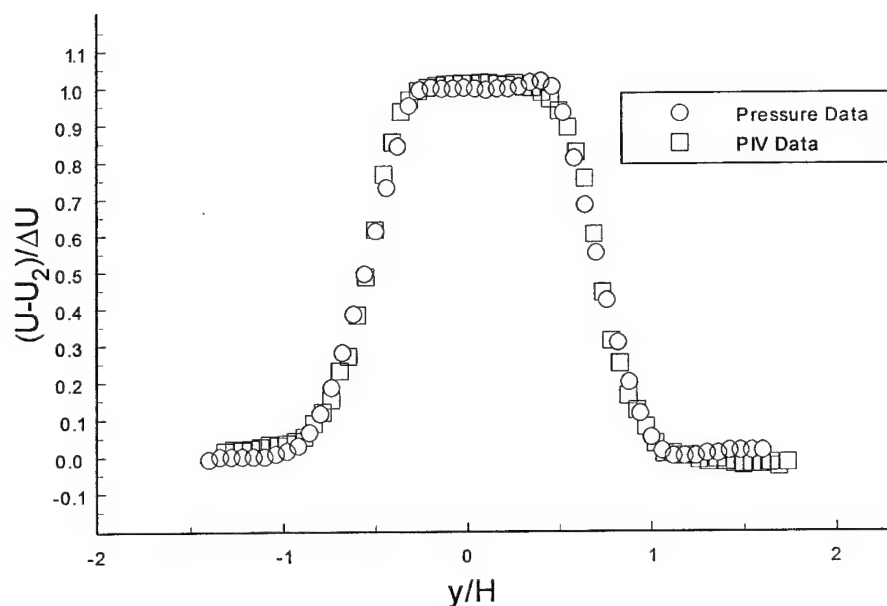


Figure 4.37: Comparison of a velocity profile using PIV and pressure measurements

Free Jet v Component Measurements

One of the advantages of the PIV measurement technique is that both components of the velocity are simultaneously measured. In the case of the free jets, the cross-stream profiles of the v velocity component can illustrate some interesting features. The relative error in these measurements is large due to the large turbulence intensity present in the v velocity component. These measurements give insight into the magnitude of the v component relative to the streamwise component u as well as the shock cell spacing.

As shown previously, the Mach 2 free jet has shock cells that expand and compress the jet core. This effect leads to v component velocity profiles that repeat at the wavelength of the shock cells. The profiles fall into two categories depending

on the compression-expansion nature of the flow. Figure 4.38 shows the v velocity profiles for streamwise locations where expansion of the jet core is occurring. The locations of the profiles are also shown on an iso-velocity contour illustrating that expansion is occurring at these streamwise locations. Other locations in the flowfield are experiencing a compression of the jet core. The v velocity profiles for the compression zones are shown in Figure 4.39. The iso-velocity contour is included again to show that these streamwise locations are in a compression region.

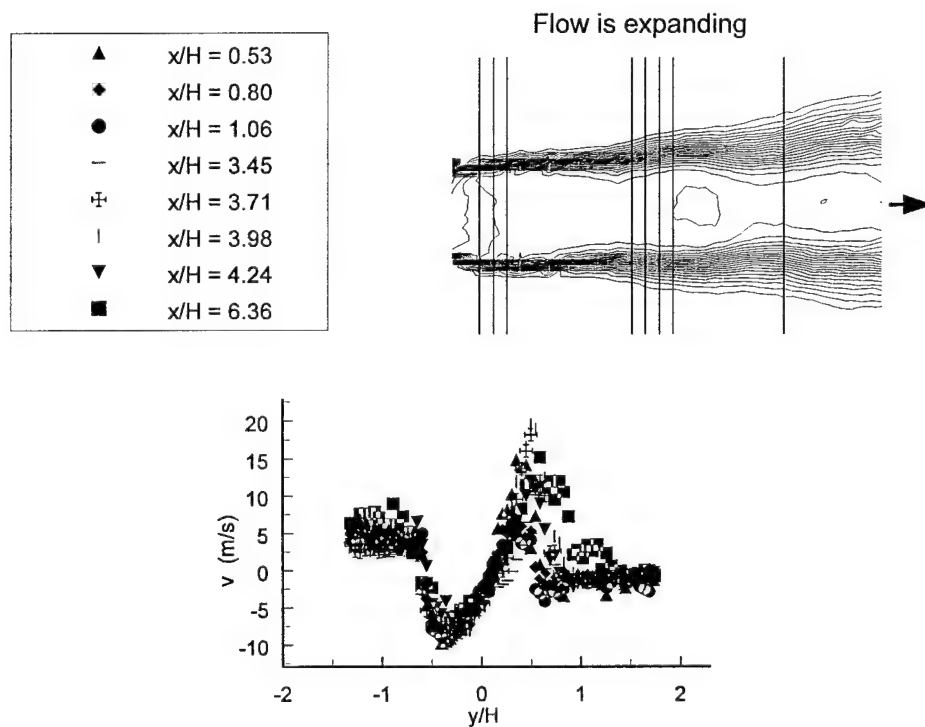


Figure 4.38: v velocity component profiles for the ideally expanded jet (expansion)

It is interesting to see that the potential core of the jet has a v velocity component that varies in a linear like fashion across the jet, which represents the expanding and

compressing processes in the jet core. The streamwise distance between clusters of profiles that have similar shapes is equal to the wavelength of the shock cells. For

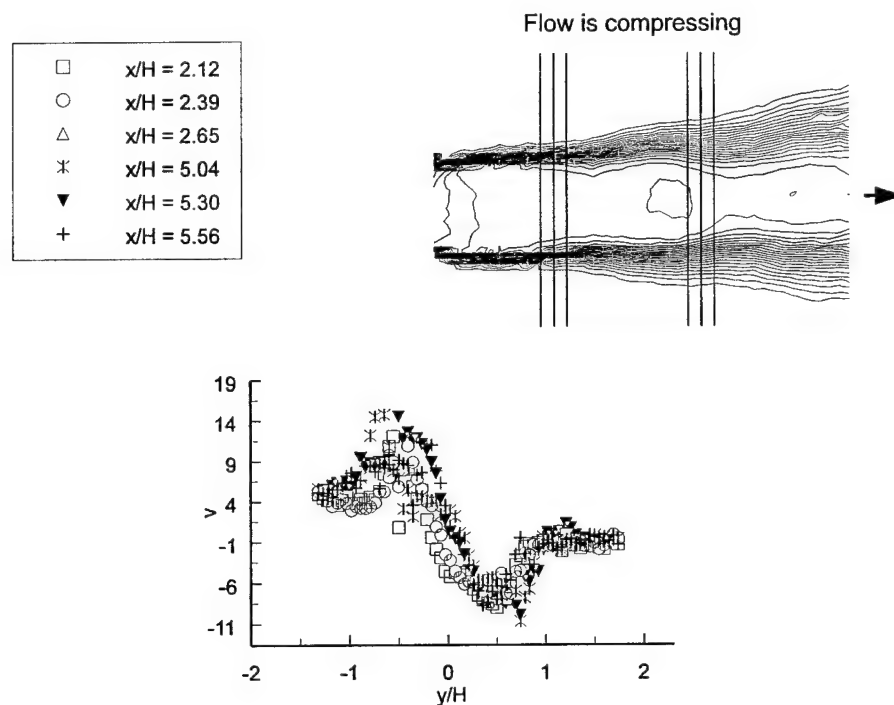


Figure 4.39: v velocity component profiles for the ideally expanded jet (compression)

the ideally expanded case shown in Figure 4.38, it appears that the profiles separated by 3 jet heights H have similar shapes. Thus the shock cells have a wavelength of approximately $3H$. The v velocity component profiles for the over and underexpanded jets can be found in the appendix (Figures A.24 and A.25). The shock cell spacing is seen to be approximately 2.5 and $3.5H$ (in agreement with the velocity magnitude plots) for the over and underexpanded jets. The v component reached somewhat larger values for the underexpanded jet than the other free jet

cases (due to the larger expansions of the jet), with all v component magnitudes remaining below 4% of the streamwise velocity in the potential core.

Growth of Shear Layers for the Thrust Vectored Jets

Growth rate measurements for the Mach 2 jet in a thrust vectoring configuration will give insight into the effect of the curvature and counterflow on the jet behavior. The growth of the shear layers of the ejector case (collar present, no suction) will be investigated first to determine the effect of the addition of the collar and Plexi glass side plates. The moderately vectored case ($P_{\text{exit}} = -2.0$ psig) growth behavior will help isolate the effects of curvature.

As shown in previous sections, the velocity flowfield for the ejector case (no suction) is very similar to that of the ideally expanded free jet from the standpoint of

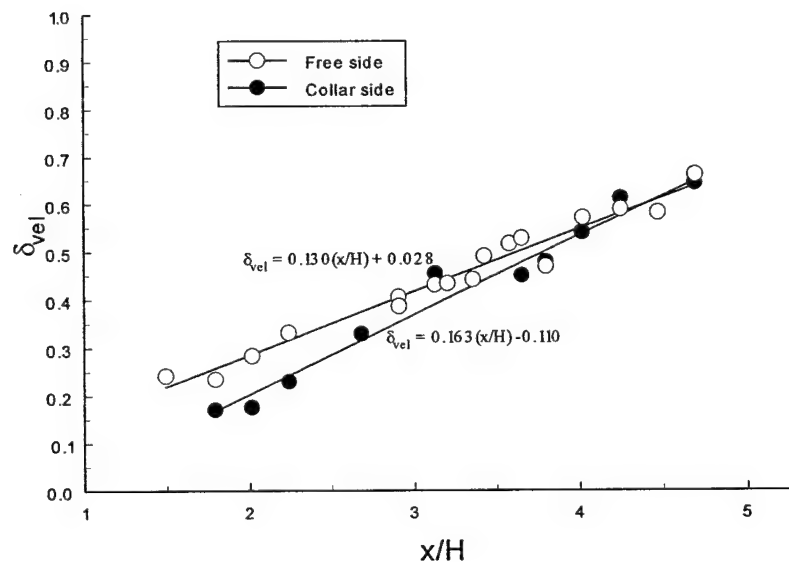


Figure 4.40: Velocity shear layer growth for the ejector case

shock structure. The shear layers of this flow must be addressed separately because of the asymmetry of the configuration (only one side of the collar is present). The shear layer thickness' of the free and collar side shear layers for the ejector is shown in Figure 4.40. The growth is seen to be relatively linear as expected. It is interesting to note that the growth rate is 0.13 for the free side, which is slightly larger than that for the free jet. This suggests that the placement of the side plates has an effect of forcing the jet to spread faster in the short dimension plane. This growth rate is in excellent agreement with axisymmetric jets at similar conditions (Wishart, 1995). The ejector case behaves more like a two dimensional jet than the rectangular free jet due to the confinement caused by the side plates. Thus for free rectangular jets, the effect of the growth in the long dimension does have an effect on the short dimension shear layer growth. If we suppose that axisymmetric and two dimensional jet shear layers grow at the same rate, then it may be concluded that a rectangular jet with an aspect ratio of 4.0 does not behave two dimensionally from a shear layer growth standpoint.

As presented in previous sections, the ejector case induces a large amount of counterflow from the natural entrainment process of the collar side shear layer. From a qualitative observation of the instantaneous velocity fields, the flowfield between the core of the jet and the collar surface is believed to have higher levels of turbulence than the free jet. In fact, the local turbulence intensity becomes very large in the low speed portion of the shear layer. To accurately measure the mean properties of a highly turbulent flow, many samples are required. Unfortunately, because of the time costs of processing PIV images, the number of velocity values

available to calculate the average flowfield has a practical limit. This leads to high levels of relative error in the counterflow region. This will inevitably add error to the growth rate calculations. This is evident in the growth distribution of the collar side shear layer of the ejector case (Figure 4.40). The growth rate for this shear layer is 0.16, which is a 23% increase over the free side shear layer growth rate. The counterflow velocity magnitudes are quite high for the jet without suction, generally on the order of 20% of U_1 . This leads to slower convective velocities of the shear layer structures resulting in larger growth rates.

The effect of the curvature and suction on the growth rate of the shear layers can be addressed with an investigation of the moderately vectored case. Since the resulting vectored angle is less than 10° , this case lends itself well to the growth rate calculations because the curvature is small. The growth of a curved shear layer is no longer a function of the x direction but is depended on the curvilinear streamwise coordinate. Since the curvature is small, the streamwise coordinate can be assumed to be the x axis. The growth of the free side shear layer for the ejector and moderate suction cases are shown in Figure 4.41. The growth rate is 32% larger than the ejector case. Since this side is absent of counterflow effects, and the curvature is of the destabilizing type, the observed increase in the growth rate is purely due to the curvature. This is a surprising result since the curvature is so small.

The growth of the collar side shear layer for the moderately vectored case is a complicated issue since counterflow and streamwise curvature are present. In fact, the curvature effect alone is complicated since the shear layer is made up of regions of both types of curvature. The portion of the shear layer where the mean velocity

varies from the jet core U_1 to zero has stabilizing curvature while the region with negative velocity (referenced to the primary jet flow direction), thus the counterflow portion, has destabilizing curvature. The growth of the top shear layer for the

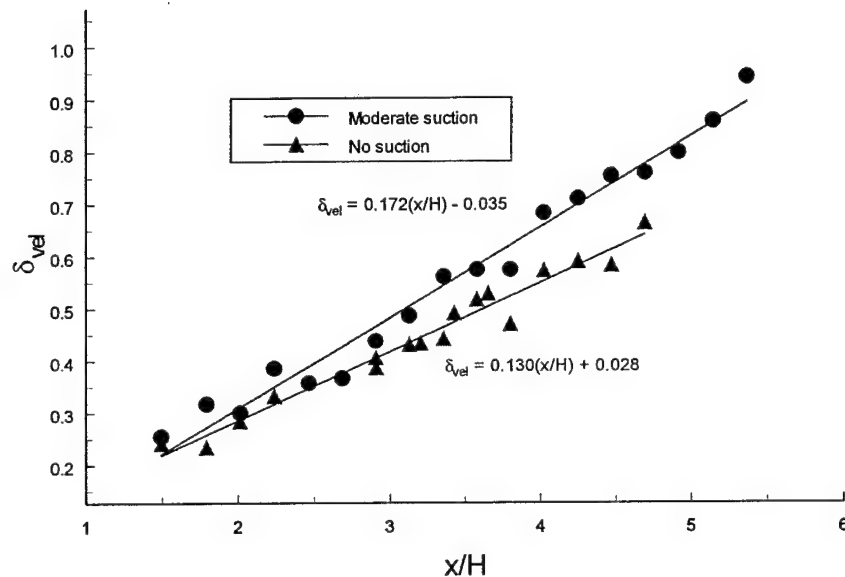


Figure 4.41: Curvature effects on the free side shear layer growth

moderately vectored jet is shown in Figure 4.42. The growth rate is found to be 0.166, which is the same as the ejector case. This can be rationalized in many ways. Intuitively, the growth of the top shear layer should be larger if the jet entrainment causes the drop in pressure between the jet and collar. But the presence of the collar has a controlling effect on the growth of the shear layer because it limits the amount of entrainment mass available to the jet. One can speculate that the application of suction has a net effect of exciting the shear layer. This enhanced mixing leads to a lower pressure on the one side of the jet, causing the jet to vector.

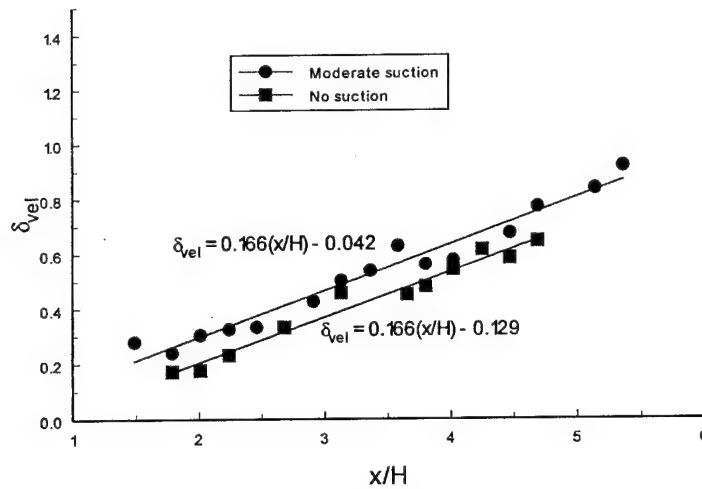


Figure 4.42: Suction effects on the collar side shear layer growth

As the jet moves closer to the wall, the mass available for entrainment is lowered causing a reduction in the growth rate. Equilibrium between the mixing enhancement (caused by the suction) and entrainment constraint due to the presence of the collar leads to a vectored jet with the suction side shear layer having an unchanged growth rate.

The collar side shear layer growth for the ejector and moderate suction cases (as shown in Figure 4.42) can give insight into the effect of the application of suction on the counterflowing shear layer. The growth rates of the two shear layers are nearly identical, but the shear layers are thicker for the case with the suction applied. This suggests that the application of the suction excites the shear layer. The cause of the excitation is not clear since the situation is complicated by the effects of

counterflow, destabilizing and stabilizing curvature, and the entrainment constraining collar.

To further explore the role of the counterflow on the vectoring process, the velocity ratio distribution for the ejector and moderately vectored jet as a function of x/H is shown in Figure 4.43. The calculated velocity ratios are based on the maximum

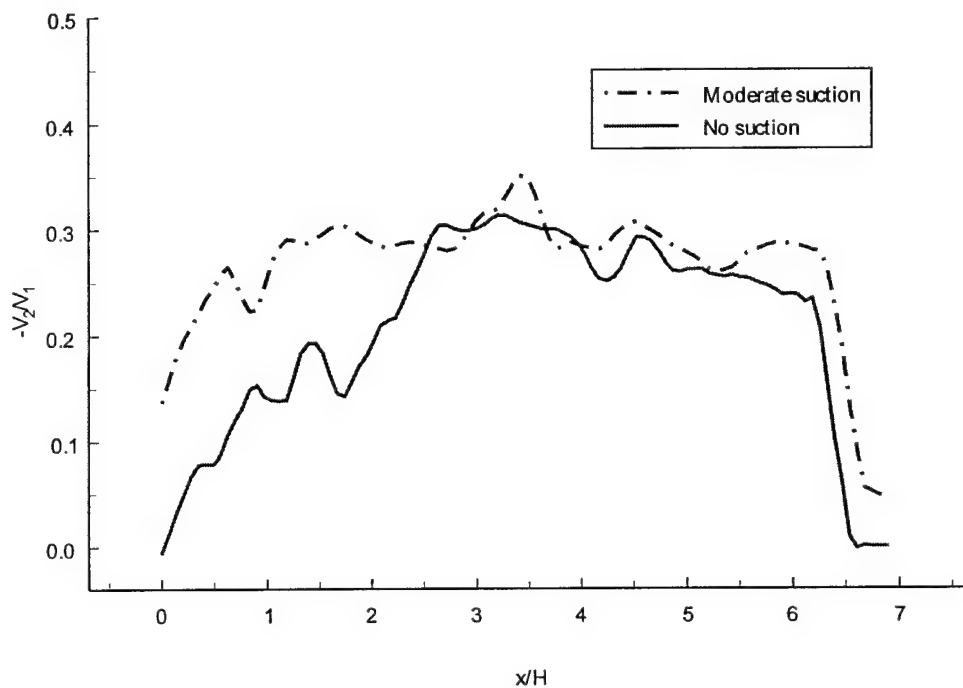


Figure 4.43: Velocity ratio distribution for the thrust vectoring configuration

and minimum velocities in each cross-stream velocity profile. Since the relative error of the velocities in the counterflow region (due to the speculated high turbulence intensities) are quite high, the error in the velocity ratio is large. The curves shown in Figure 4.43 are a spline curve fit to the experimental data which has large scatter. The trends of the curves accurately represent that of the experimental data, which

has been omitted for clarity. The magnitude of the velocity ratio suggests that absolute instability may not play a role, since theory predicts that more than 30% counterflow needs to be applied to generate absolute instability at the given density ratio and convective Mach number. The effect of the curvature on the stability has not been explored, but the streamwise curvature may have an effect of lowering the critical velocity ratio, thus absolute instability may emerge as a factor. The velocity ratio is somewhat larger for the suction case, noticeably in the first two jet heights H . This would lead to a larger shear layer growth rate in that region, leading to a thickened shear layer in the downstream portion as observed in the growth rate measurements. Thus the counterflow mechanism appears to play a role in the vectoring of the jet.

The structures present in the shear layer can be identified using instantaneous velocity flowfields as captured by Particle Image Velocimetry. Knowing that the structures grow as they travel downstream, the obvious location at which to observe the scale of the structures is in the downstream third of the collar. Some typical velocity vector fields for this region are shown in Figure 4.44. As can be seen, the structures for the jet with no suction appear quite small, and the counterflowing stream seems relatively undisturbed by the presence of the jet. For the jet with moderate suction, large scale structures appear to be present, and mixing between the counterflow and the jet appears enhanced. This would suggest that the application of suction causes the suction side shear layer to become self-excited. These larger structures cause the observed increase in the shear layer thickness.

Thus the shear layer growth investigations show that the destabilizing curvature causes a substantial increase in the growth of the outside shear layer. The collar

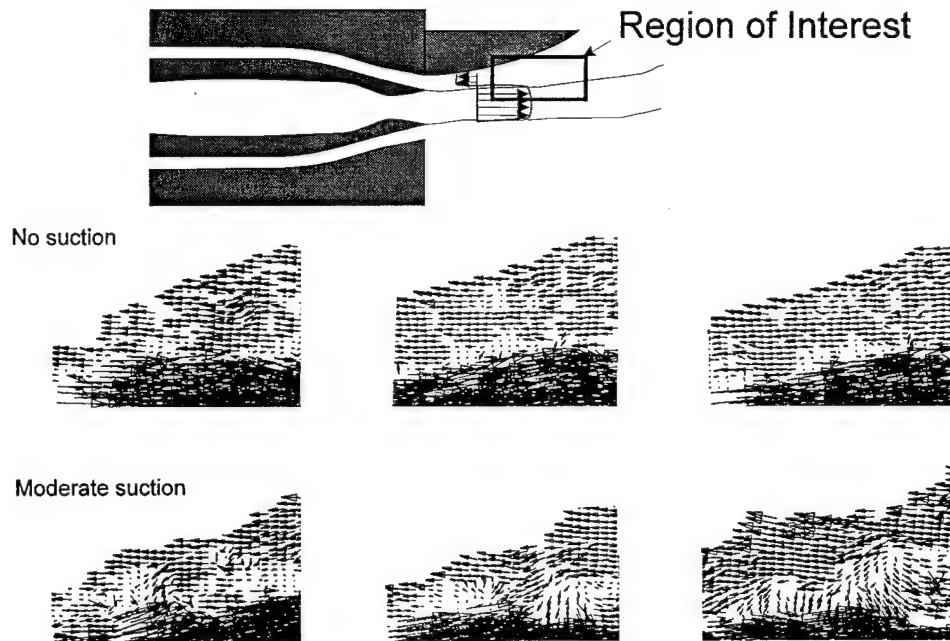


Figure 4.44: Instantaneous velocity fields for the counterflow region

side shear layer growth behavior suggests that suction causes self-excitation by the thickening of the shear layer.

CHAPTER 5

CONCLUSION

An experimental study was conducted on flows generated by a Mach 2 convergent-divergent rectangular nozzle with an aspect ratio of 4.0. The experiments were done for the nozzle in a free jet as well as a counterflow thrust vectored configuration. Measurement techniques included Particle Image Velocimetry as well as total and static pressure measurements. It was found that the velocities calculated from the pressure measurements showed excellent agreement with the PIV results, suggesting that the particles accurately follow the fluid motion.

The free jet experiments were done for the nozzle operated at ideally expanded conditions as well as mildly over and underexpanded. The ideally expanded flowfield characteristics were similar to a slightly overexpanded jet, which is due to the waves that are generated by the nozzle (the short dimension walls are parallel to each other). The shock cell structure of the jet at different operating conditions was described, and the shock cell spacing was found to increase with increasing Nozzle Pressure Ratio (NPR). The overexpanded PIV images show signs of a flapping mode, which suggests that a screech tone feedback loop was present. The structure of the shock cells had no effect on the growth behavior of the shear layers. In fact, the shear layer streamwise velocity profiles have the same similarity shape for the jet operated at the different conditions.

The experiments with the nozzle in a thrust vectored configuration were done for three different levels of suction (no suction, medium, and maximum). The flowfields show that the resulting shock cell structure (with the suction applied) is similar to that of an underexpanded jet except that the shocks are asymmetric. For the jet without suction, the free side shear layer had a shear layer growth rate similar to that found in axisymmetric jets at similar operating conditions. Thus the addition of the Plexiglass side plates force the jet to spread in a more two dimensional manner. The presence of the collar for the jet without suction causes large levels of counterflow which is induced by the natural entrainment of the jet. This counterflow causes an increase in the shear layer growth rate of approximately 23%. When moderate suction is applied, causing approximately 8° vectoring, the free side shear layer has destabilizing streamwise curvature. This addition of slight curvature caused an increase in the growth rate of approximately 30%. The suction side shear layer had a similar growth rate as the case without suction. This shear layer is complicated by the presence of counterflow, destabilizing and stabilizing curvature, and an entrainment constraining collar. The net effect is a shear layer that is slightly thicker when suction is applied. The instantaneous images support this observation, as larger scale structures appear in the shear layer when suction is applied. This suggests that the application of suction (and ensuing effects of counterflow, curvature, and collar) has a net effect of exciting the shear layer in the region near the nozzle exit. These structures enhance mixing of the jet, and lead to a lower pressure along the collar. It is this cross-stream pressure gradient that causes the thrust vectoring effect.

APPENDICES



Figure A.1: Mach 2 rectangular nozzle

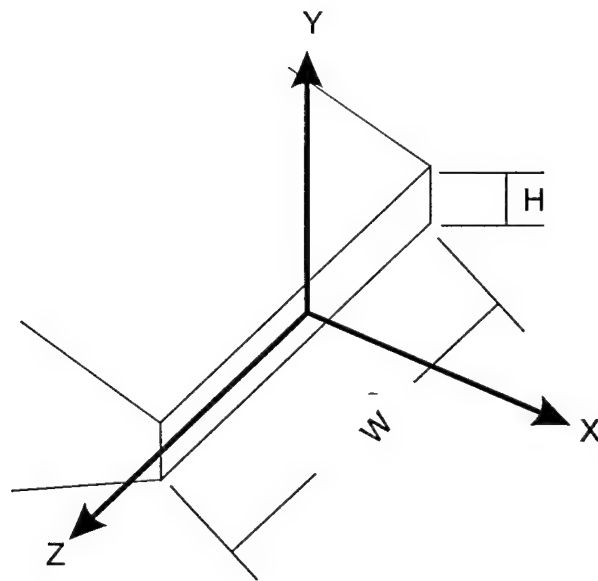


Figure A.2: Coordinate system (collar is on the positive y side)

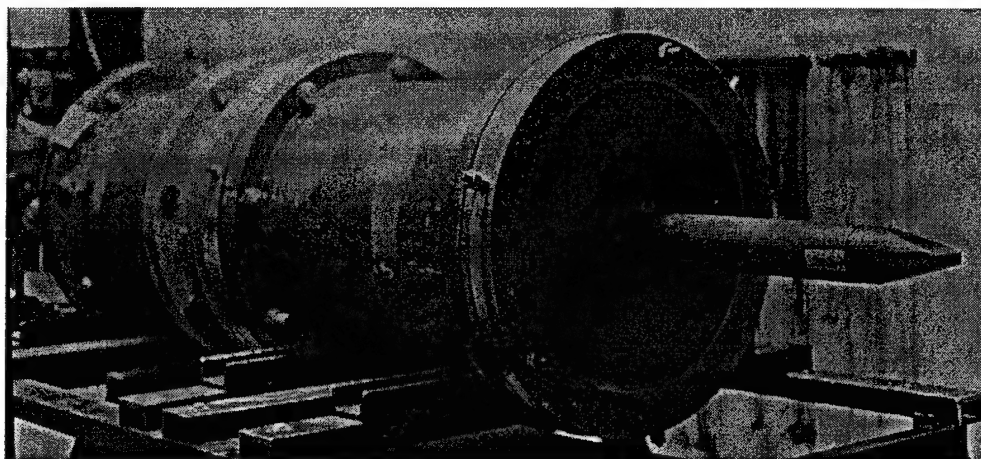


Figure A.3: External Jet Facility

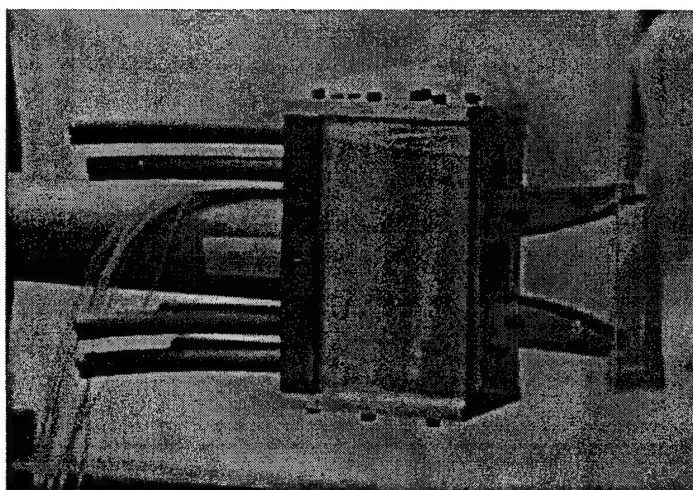


Figure A.4: Thrust vectoring nozzle configuration

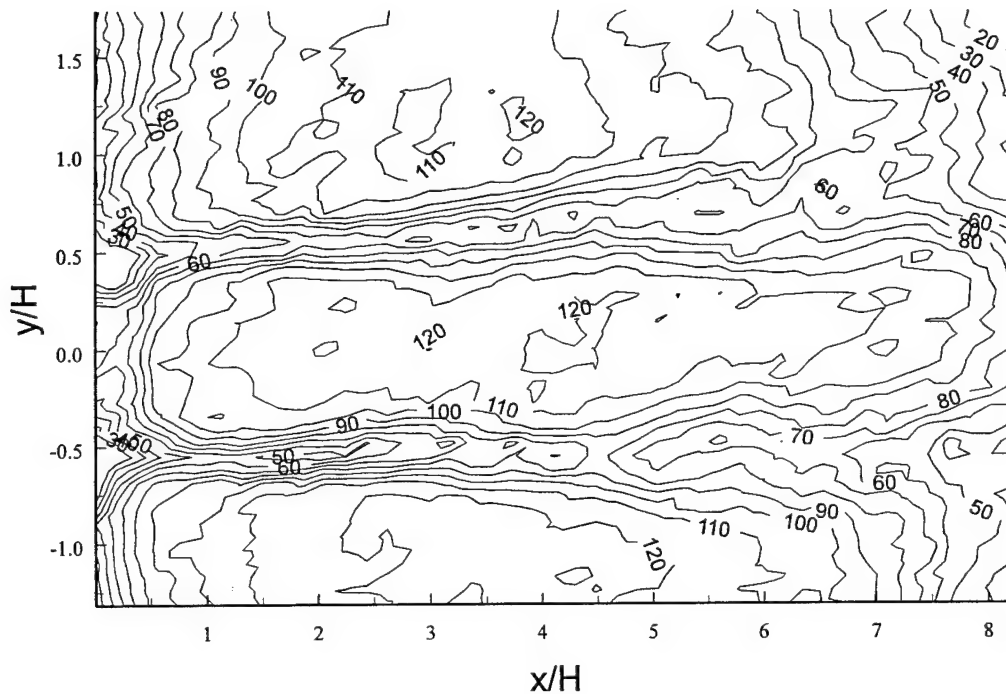


Figure A.5: Distribution of the number of velocity measurements used in the averaging of the short dimension ideally expanded free jet

Figure A.5 shows the distribution of the number of velocity data points used in the average flowfield calculation of the ideally expanded free jet (in the short dimension). As can be seen, the free stream regions (core of the jet and the ambient) have the largest number of samples because of the higher signal to noise ratios. The shear layer samples drop somewhat due to the large spatial velocity gradients which cause noise problems. Most regions have a large number of samples over which the average velocity was calculated.

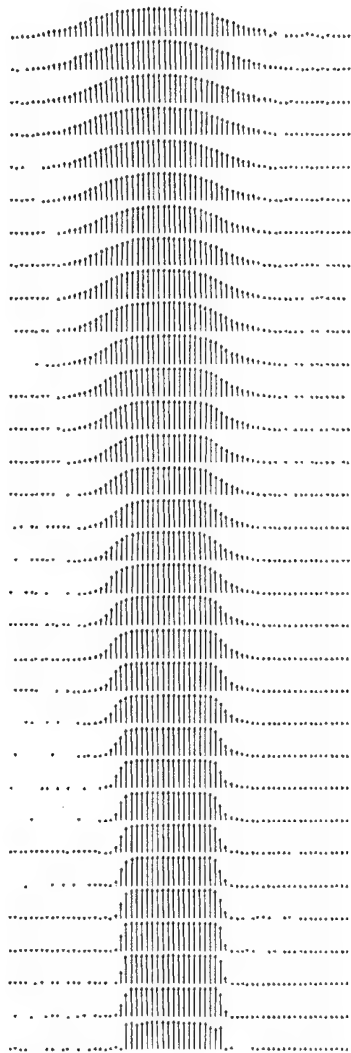


Figure A.6: Mean velocity vector field for the overexpanded jet in the short dimension

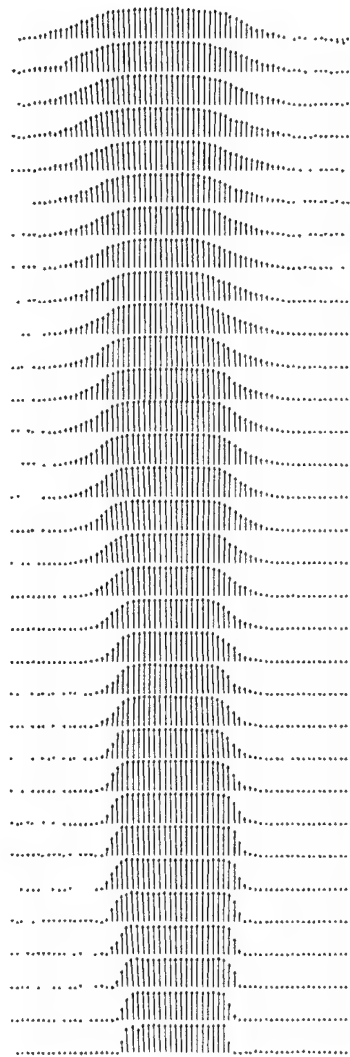


Figure A.7: Mean velocity vector field for the underexpanded jet in the short dimension

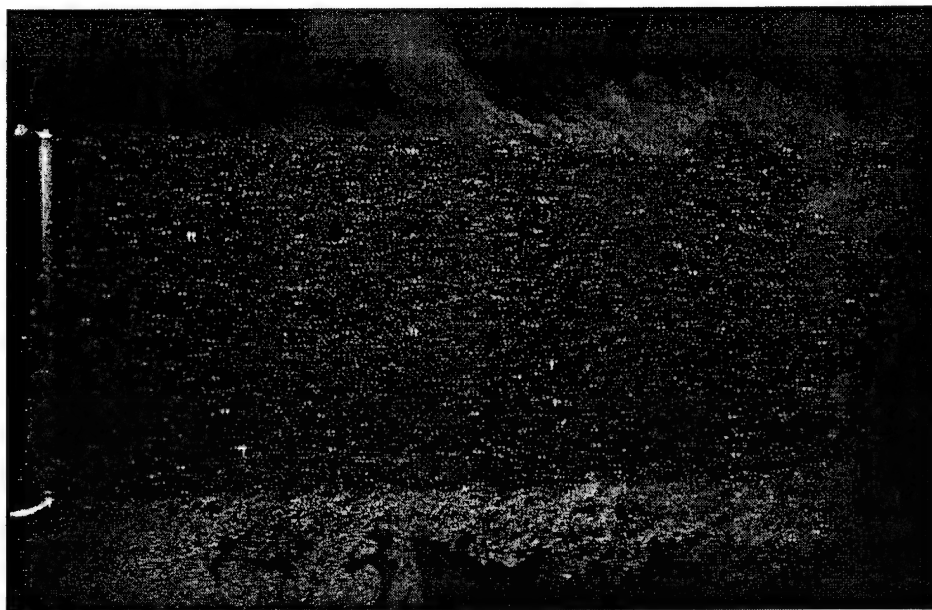


Figure A.8a: PIV image of the underexpanded free jet in the long dimension

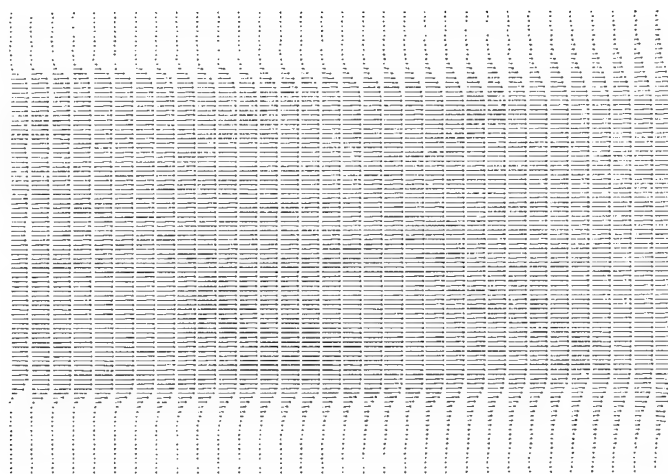


Figure A.8b: Mean velocity vector field for the underexpanded free jet in the long dimension

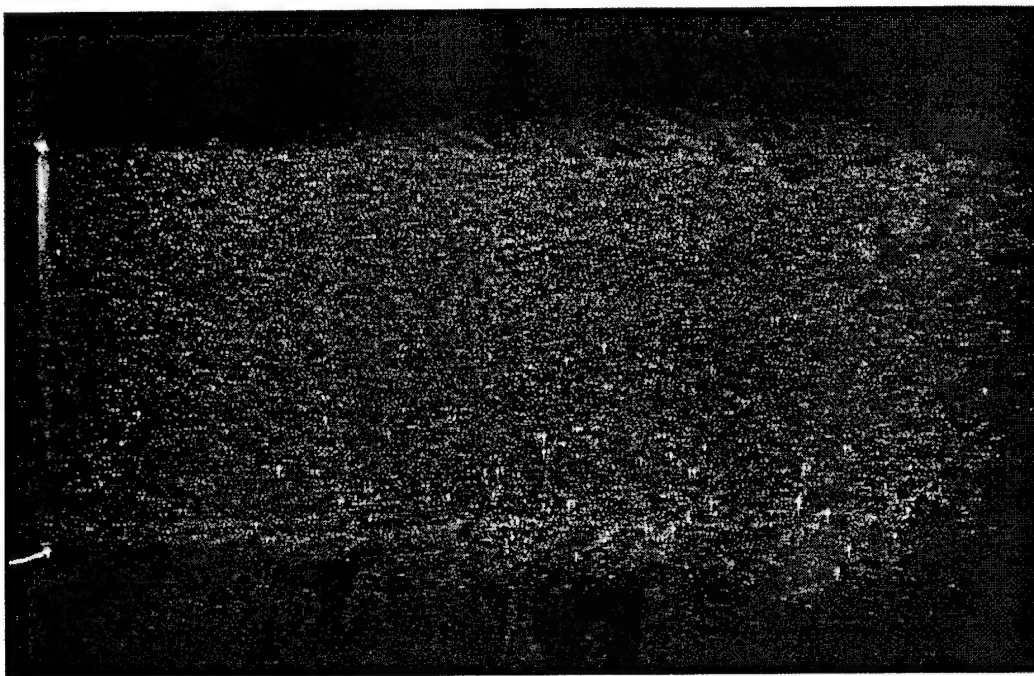


Figure A.9a: PIV image of the overexpanded free jet in the long dimension

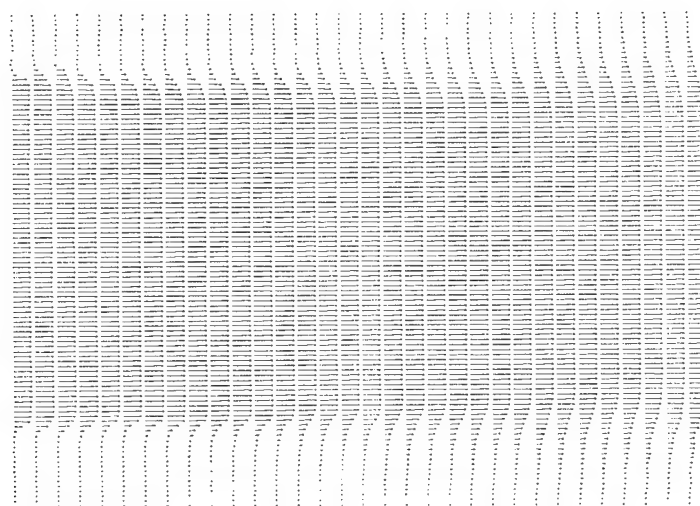


Figure A.9b: Mean velocity vector field for the overexpanded free jet in the long dimension

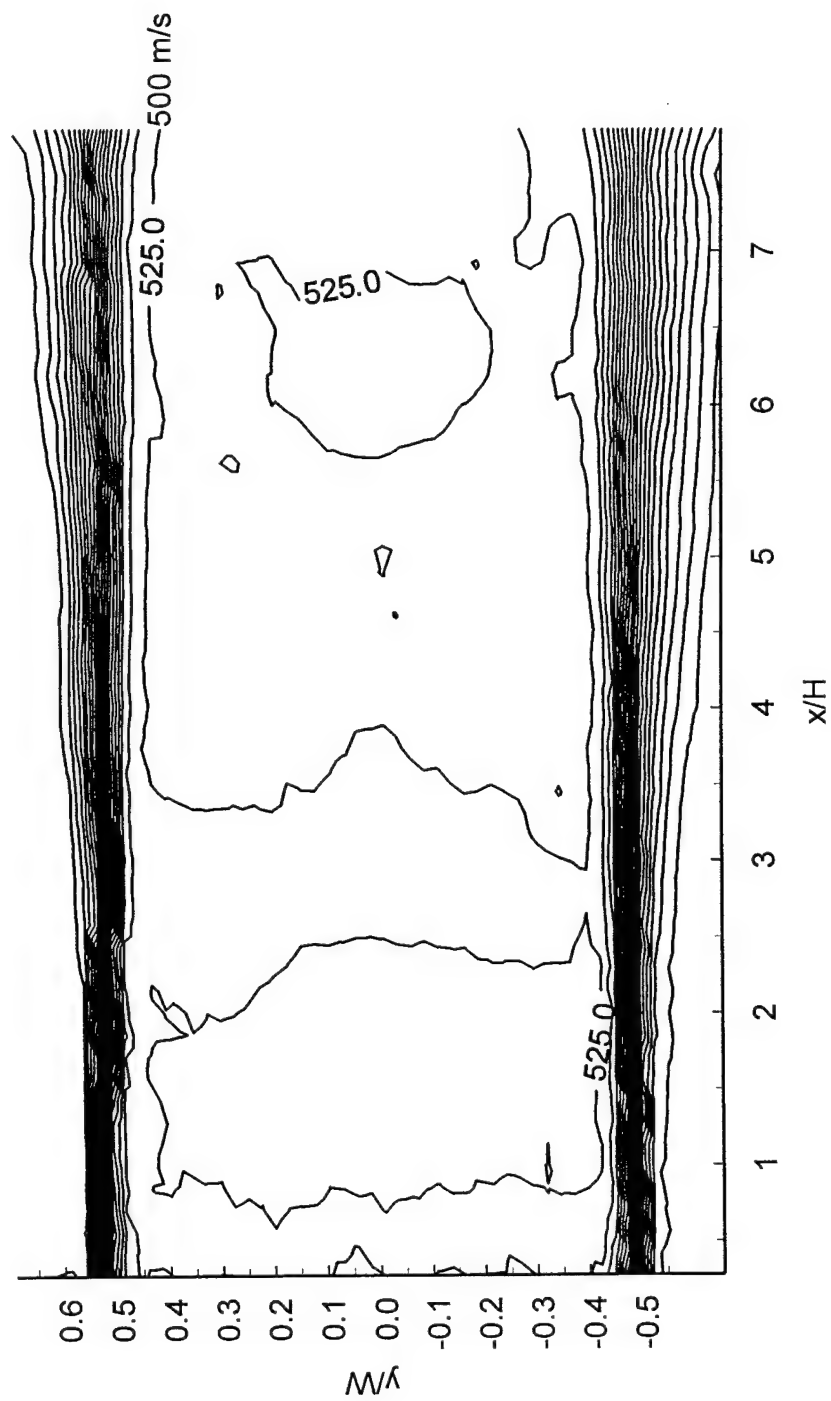


Figure A.10: Iso-velocity contours for the ideally expanded free jet in the long dimension

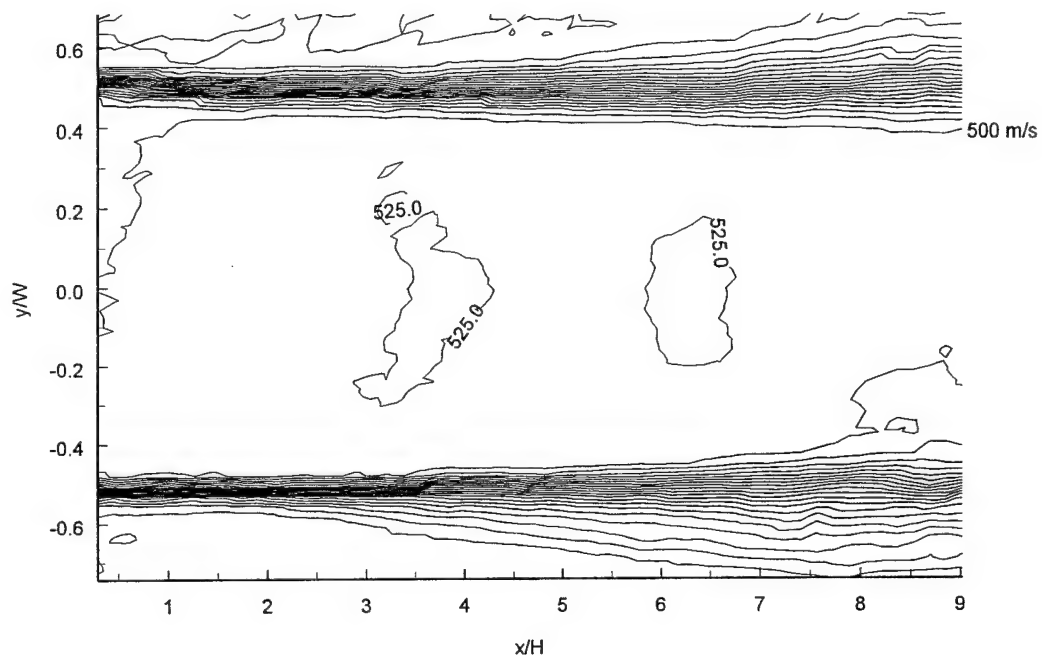


Figure A.11: Iso-velocity contours for the overexpanded free jet in the long dimension

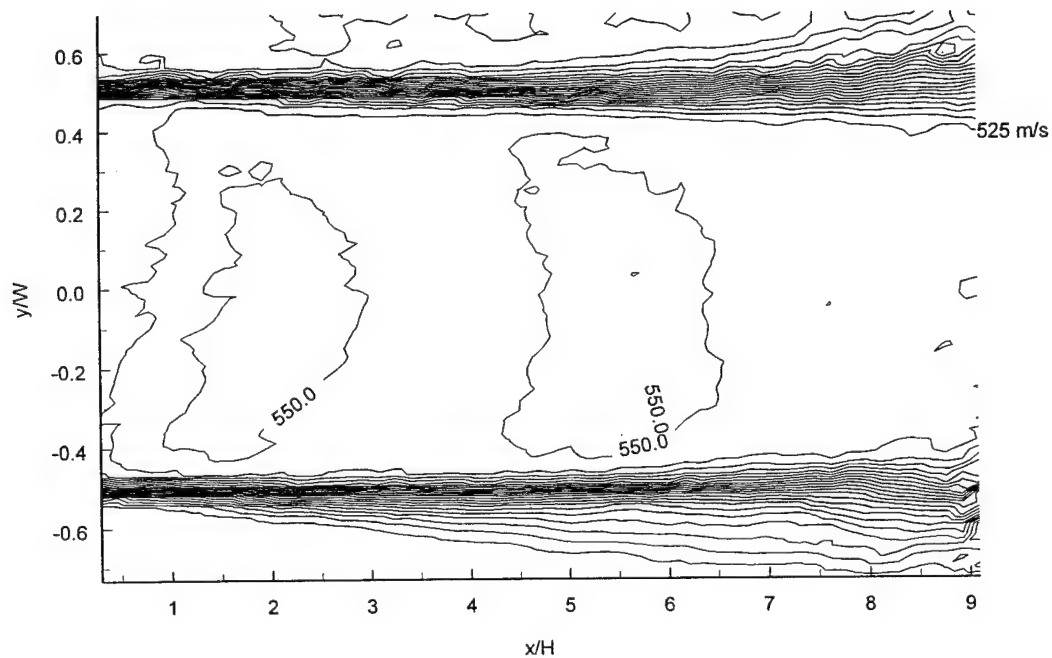


Figure A.12: Iso-velocity contours for the underexpanded free jet in the long dimension

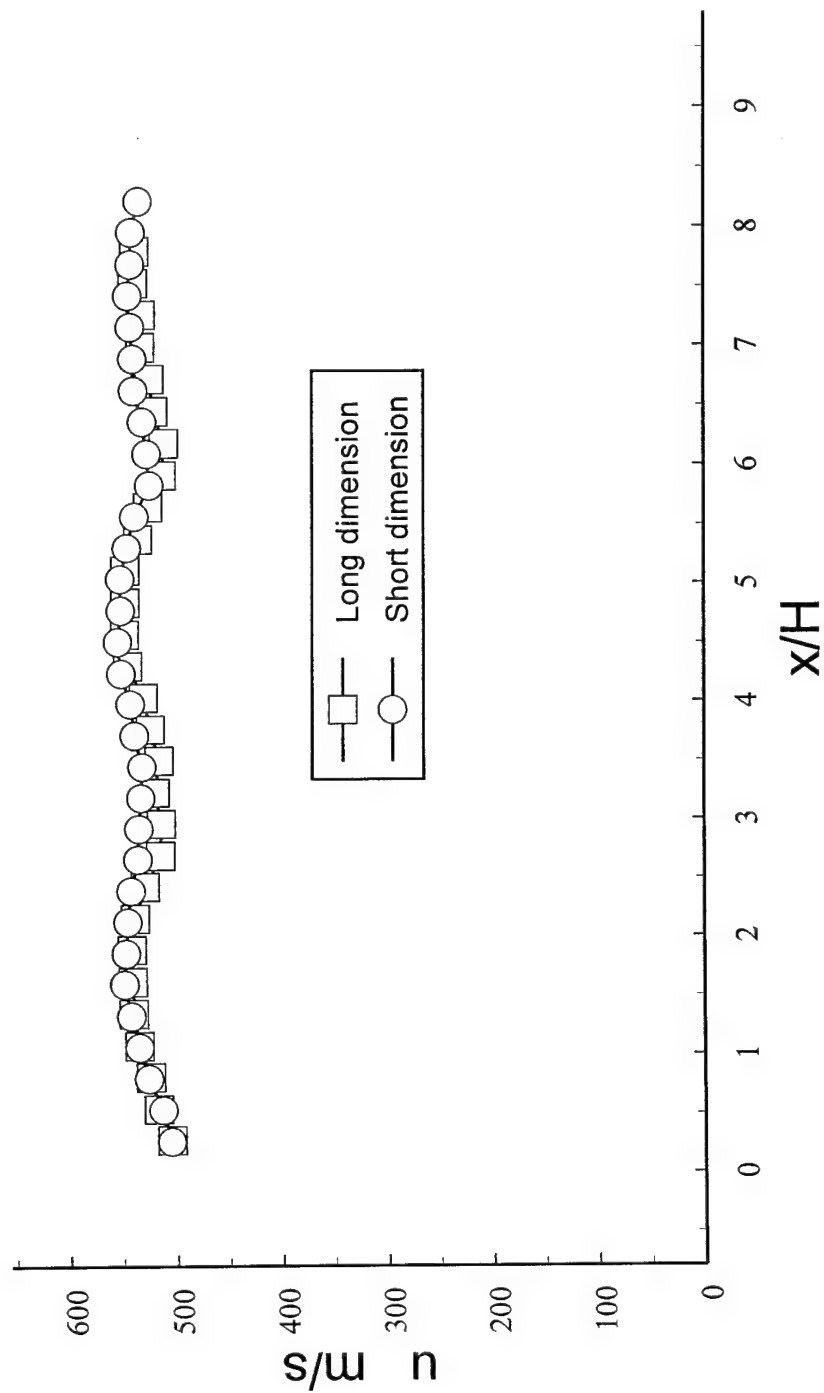


Figure A.13: Comparison of centerline velocities of the ideally expanded jet in both dimensions

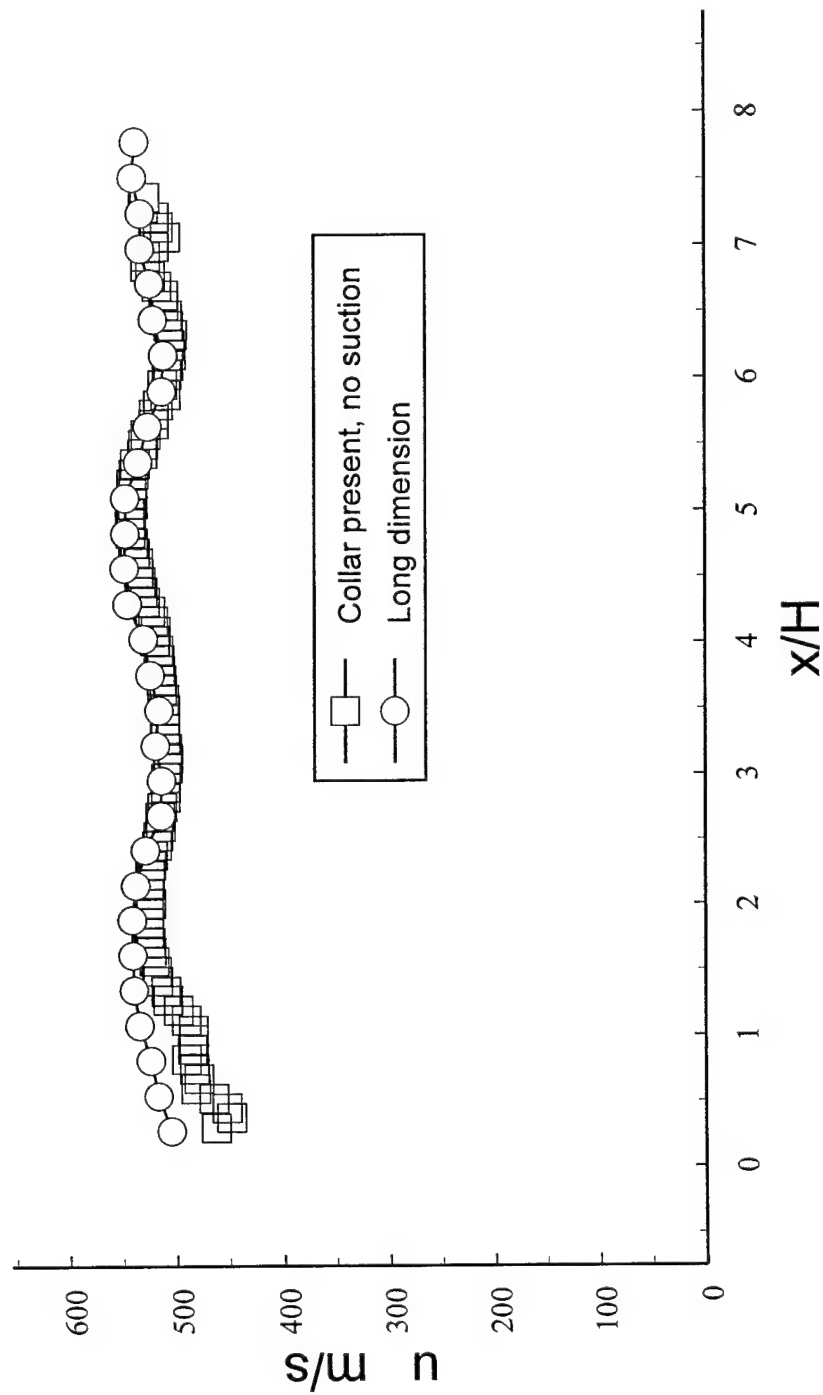


Figure A.14: Comparison of centerline velocities of the ideally expanded jet and the jet with the collar but no suction

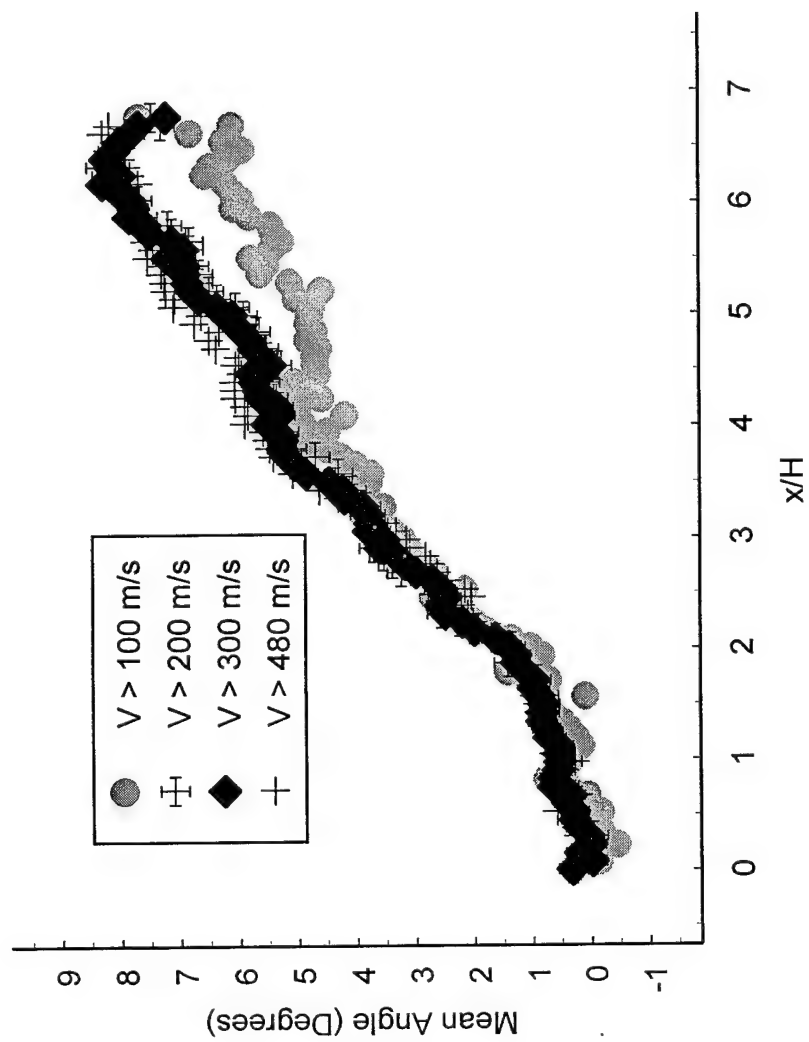


Figure A.15: Thrust angle comparisons for the moderate suction case using different inclusion criteria

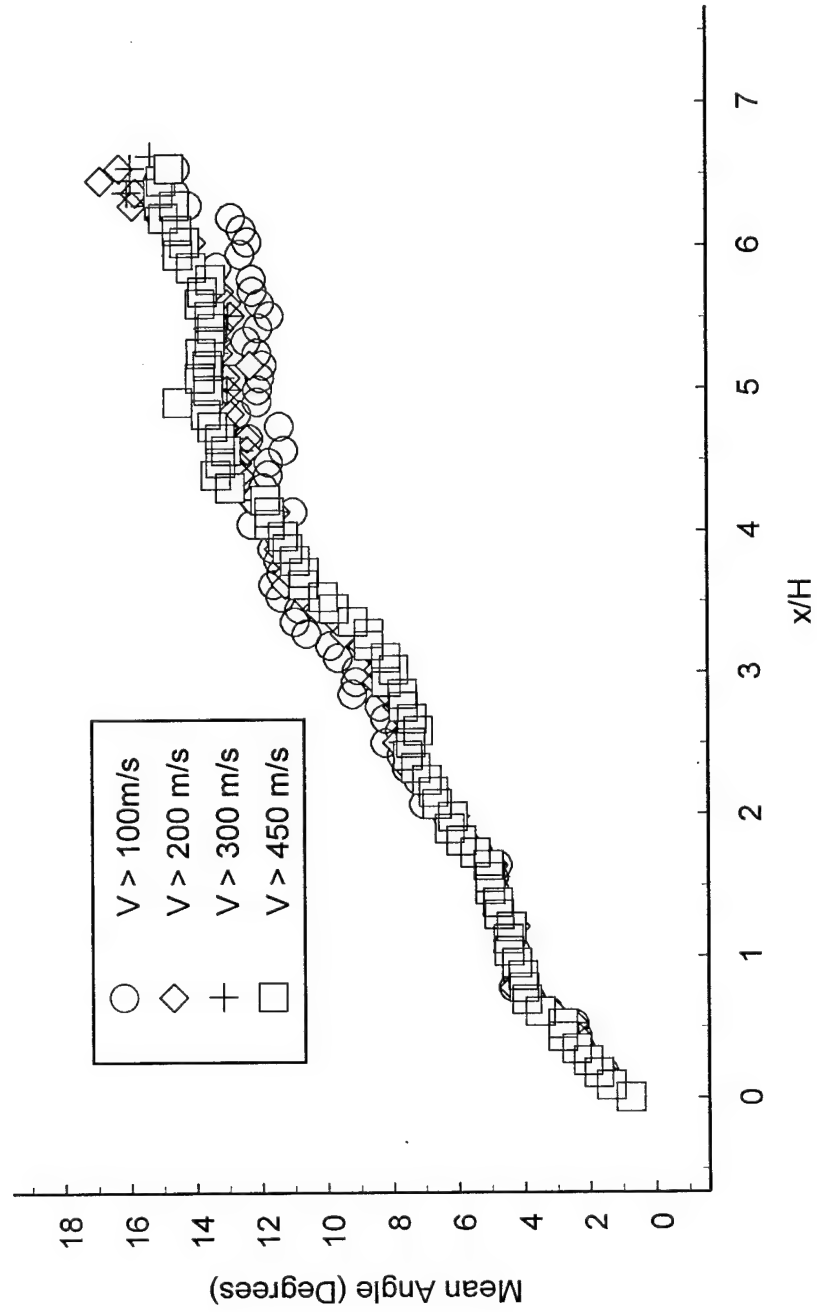
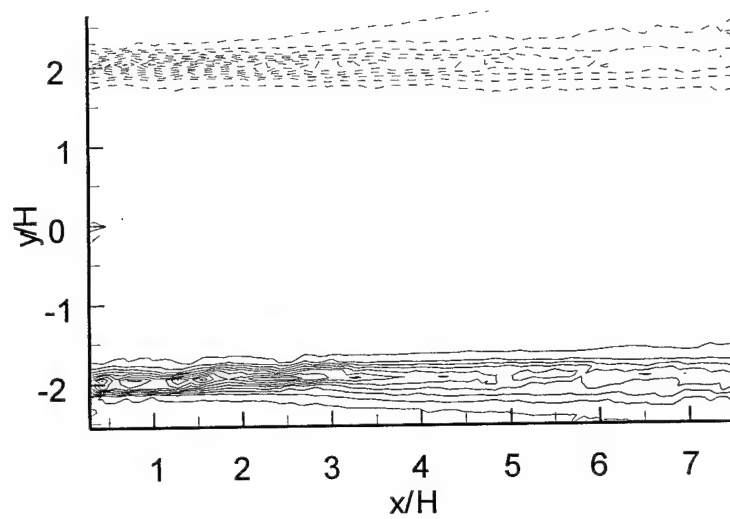
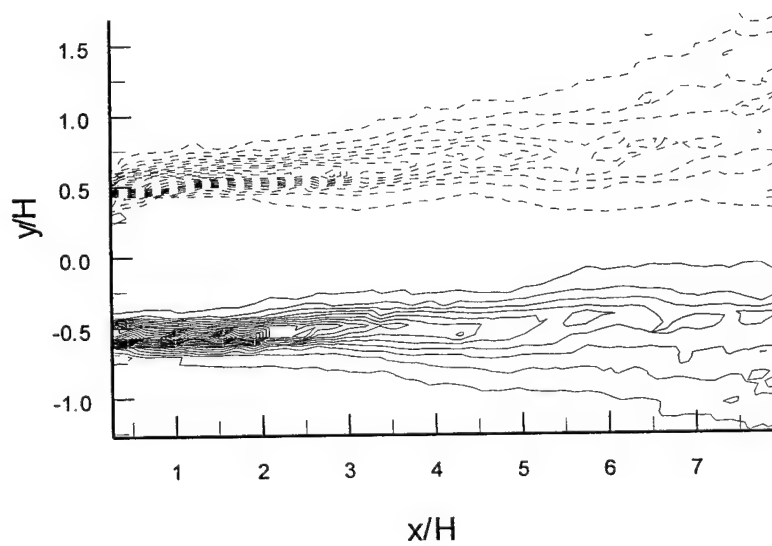


Figure A.16: Thrust angle comparisons for the maximum suction case using different inclusion criteria



(a)



(b)

Figure A.17: Vorticity distributions for the ideally expanded free jet; (a) long dimension, (b) short dimension

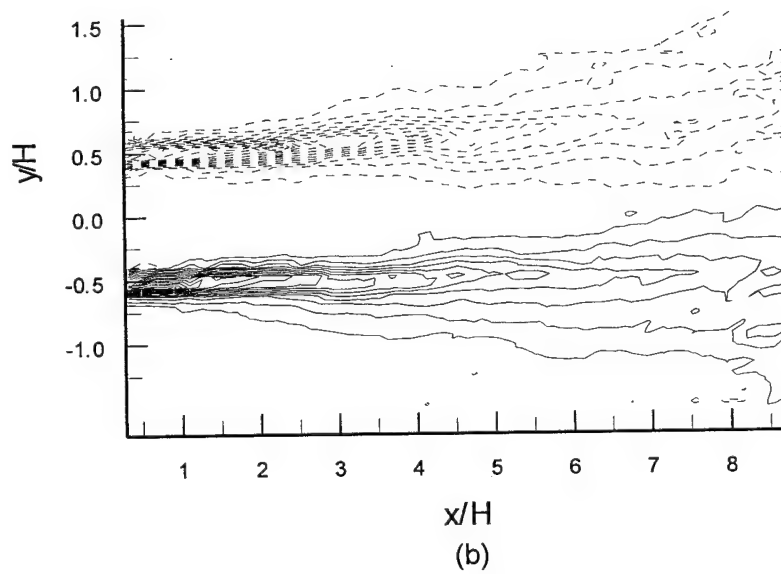
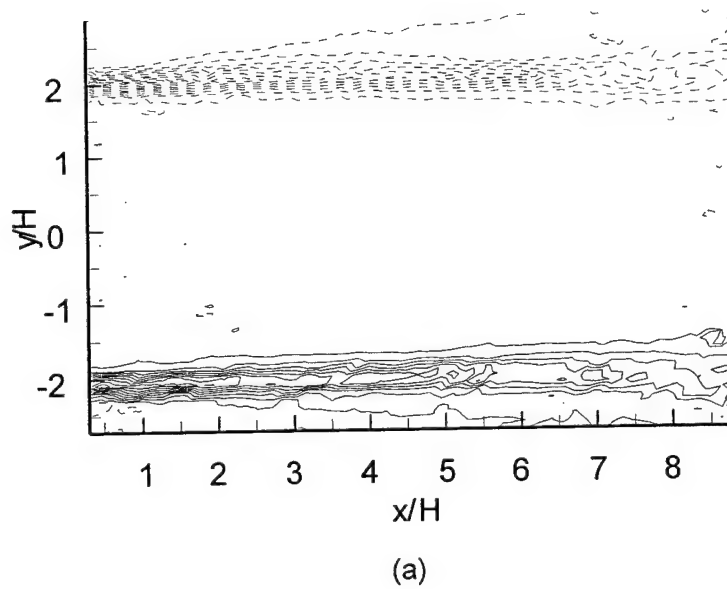
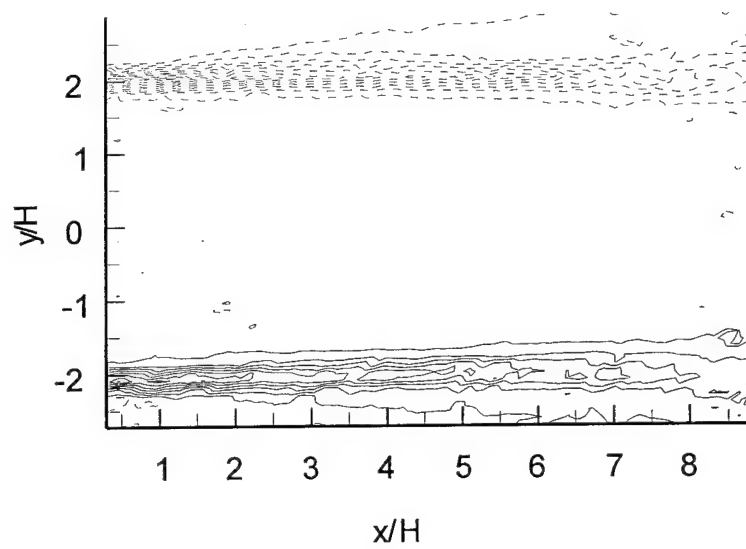
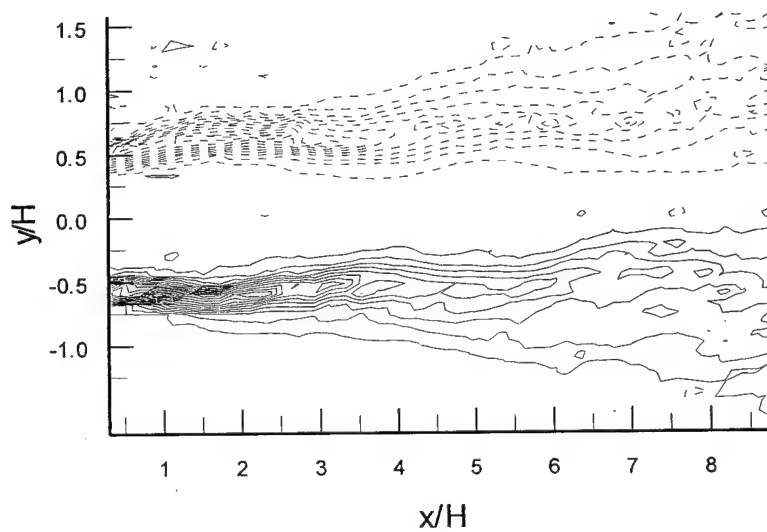


Figure A.18: Vorticity distributions for the overexpanded free jet; (a) long dimension, (b) short dimension



(a)



(b)

Figure A.19: Vorticity distributions for the underexpanded free jet; (a) long dimension, (b) short dimension

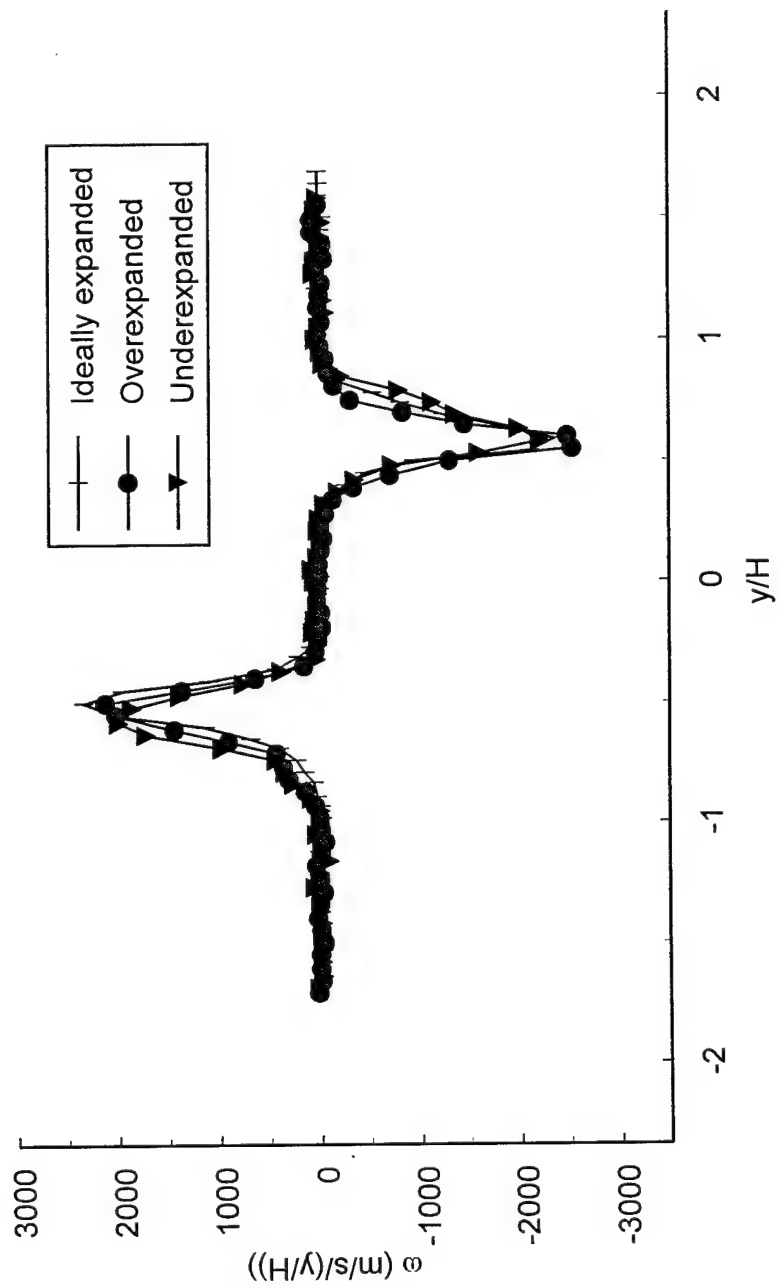
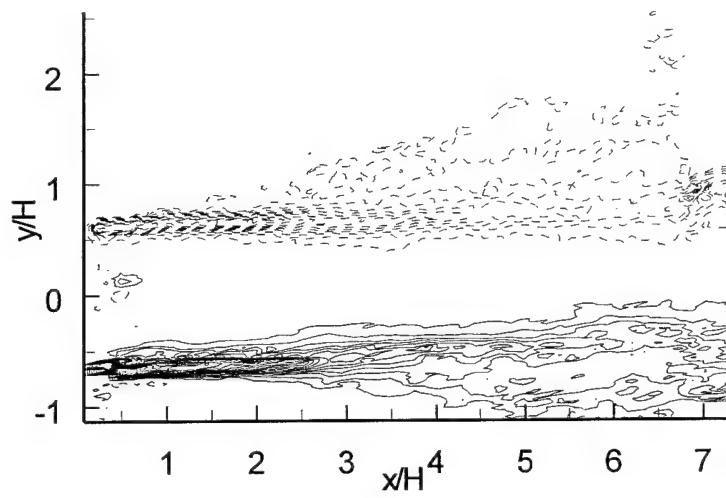
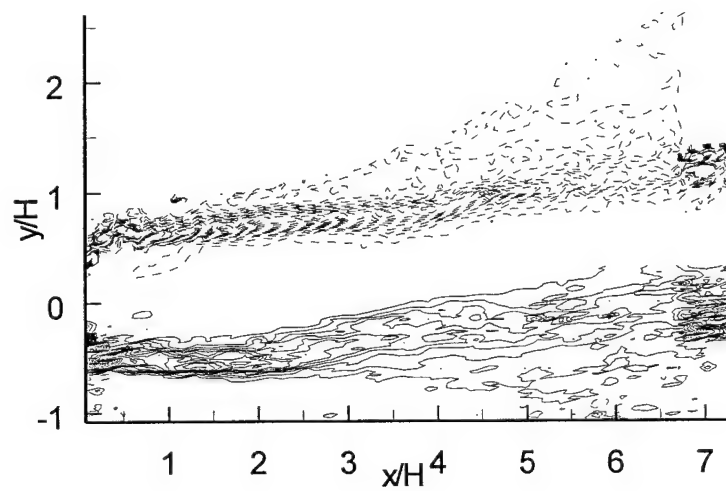


Figure A.20: Free jet cross-stream vorticity profiles for x/H equal to 2.93



(a)



(b)

Figure A.21: Vorticity distributions for the thrust vectoring configuration;
(a) no suction , (b) moderate suction

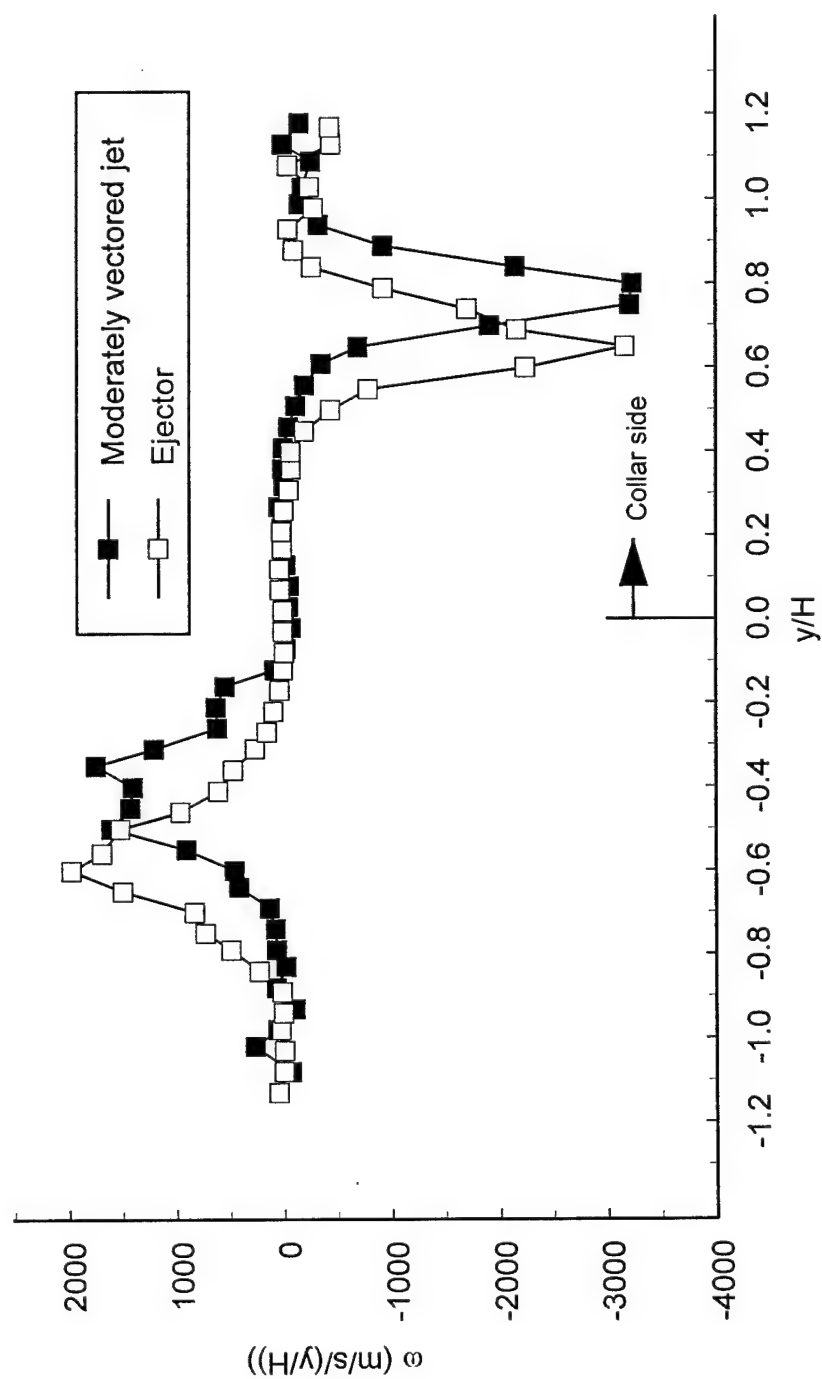


Figure A.22: Thrust vectored jet cross-stream vorticity profiles for x/H equal to 2.83

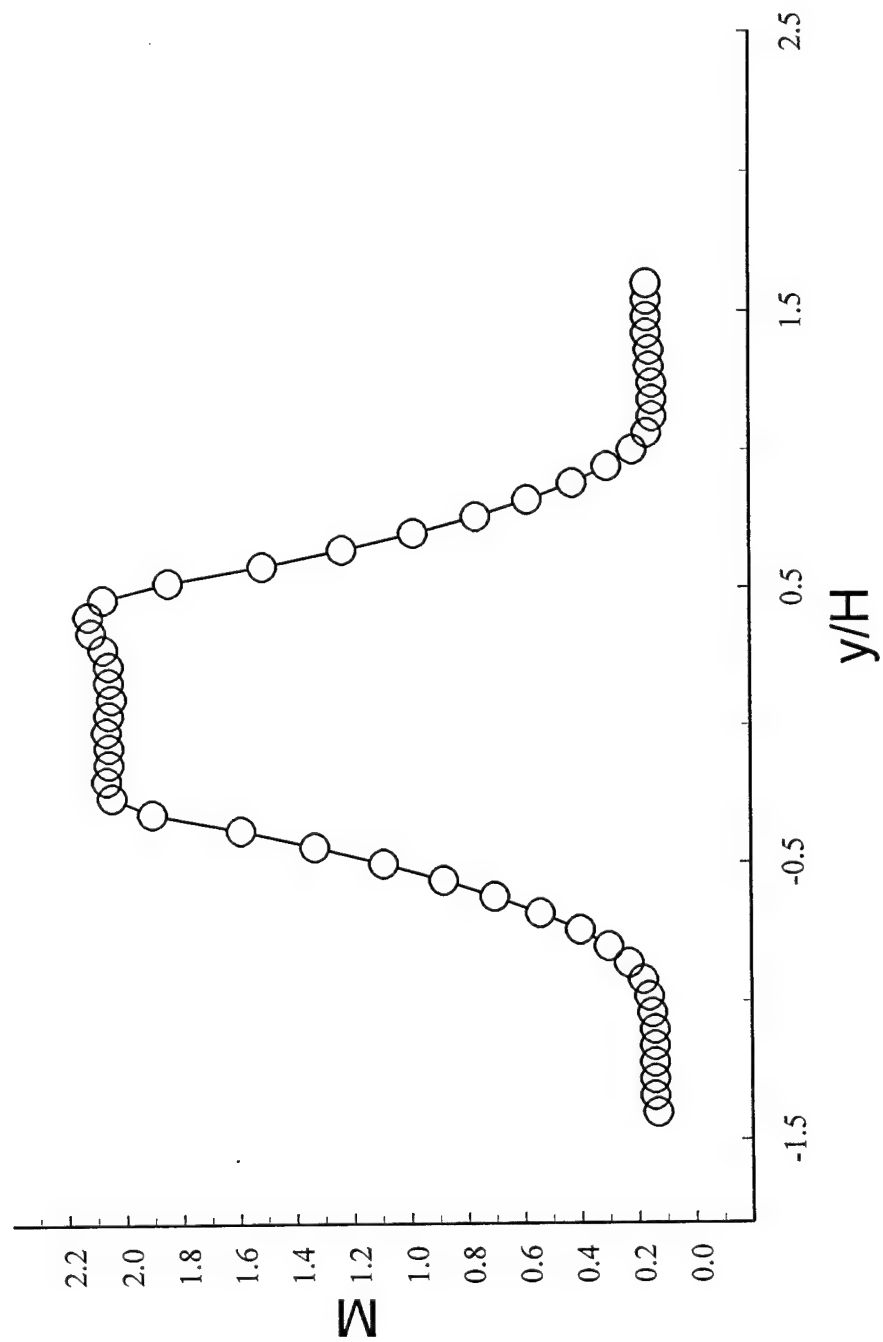


Figure A.23: Mach number profile as calculated from total (P_{o2}) and static pressure for $x/H = 4.9$

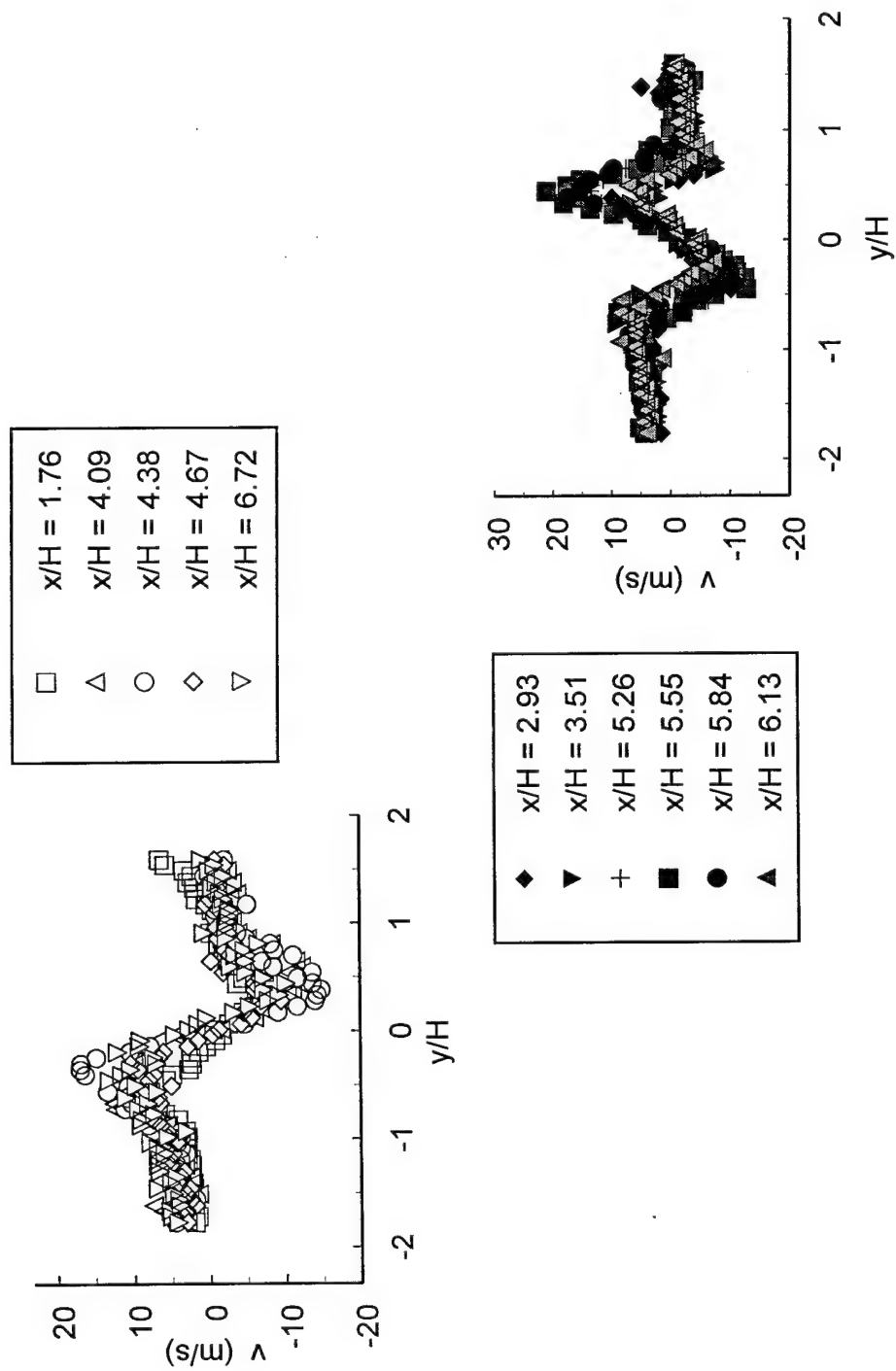


Figure A.24: v velocity component cross-stream profiles for the overexpanded free jet

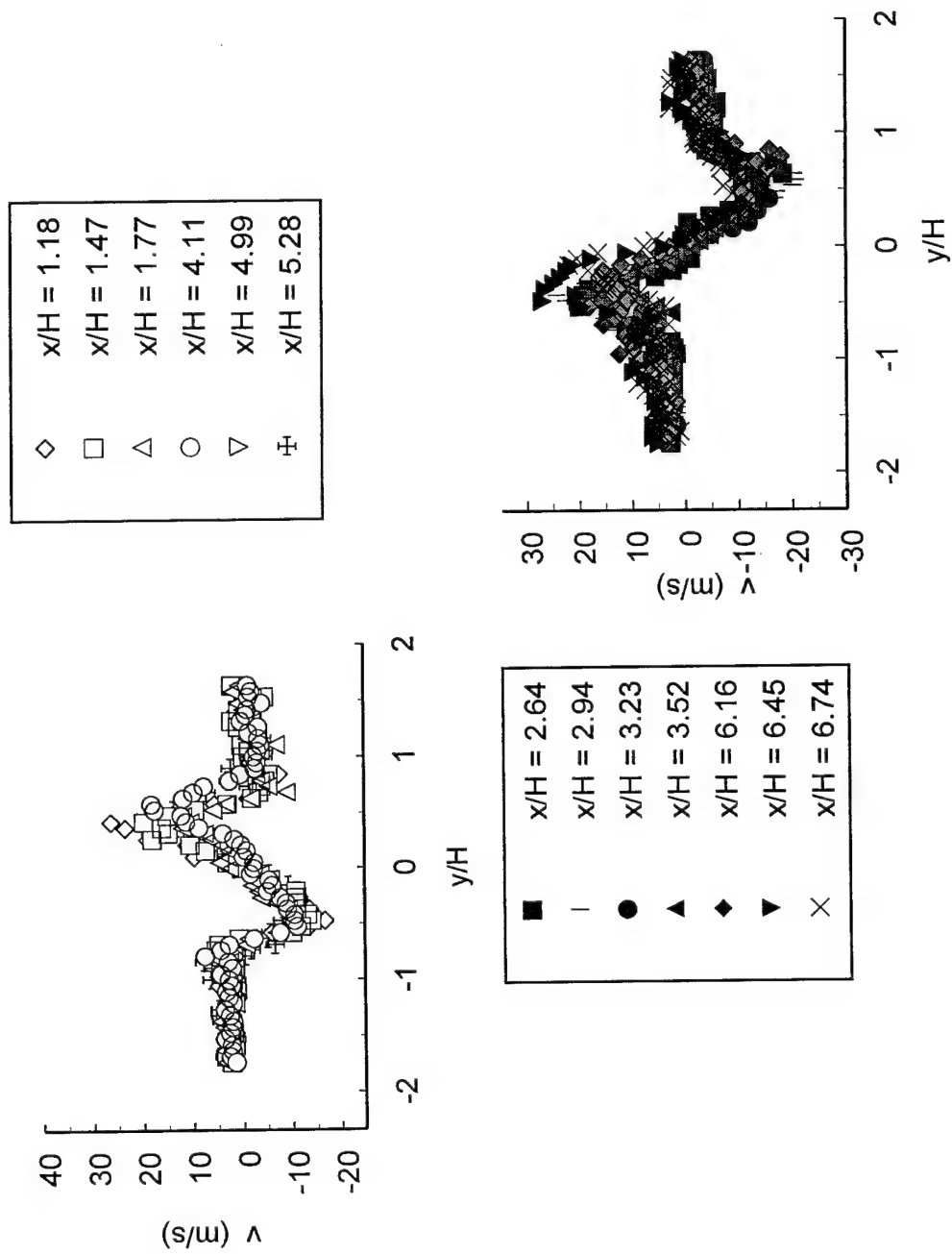


Figure A.25: y velocity component cross-stream profiles for the underexpanded free jet

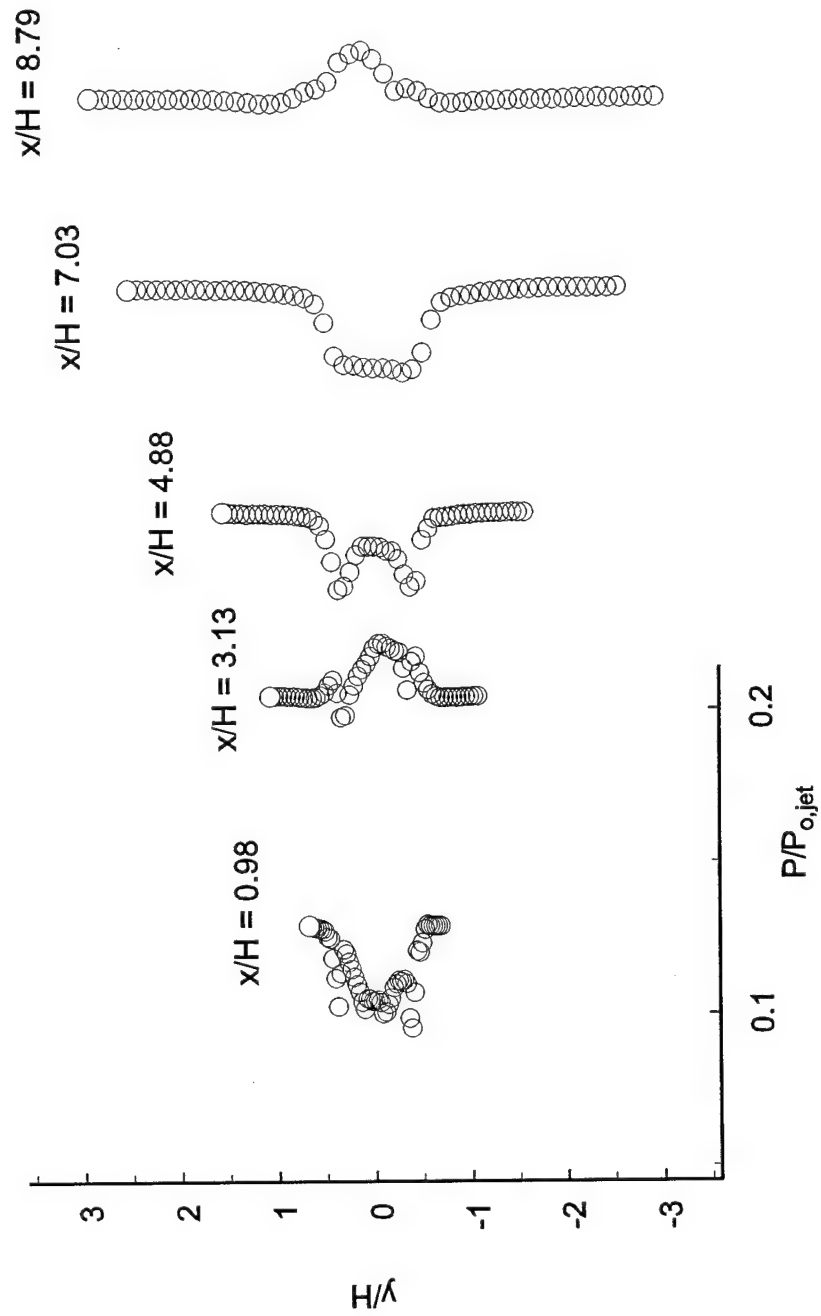


Figure A.26: Static pressure profiles at various streamwise locations for the ideally expanded free jet

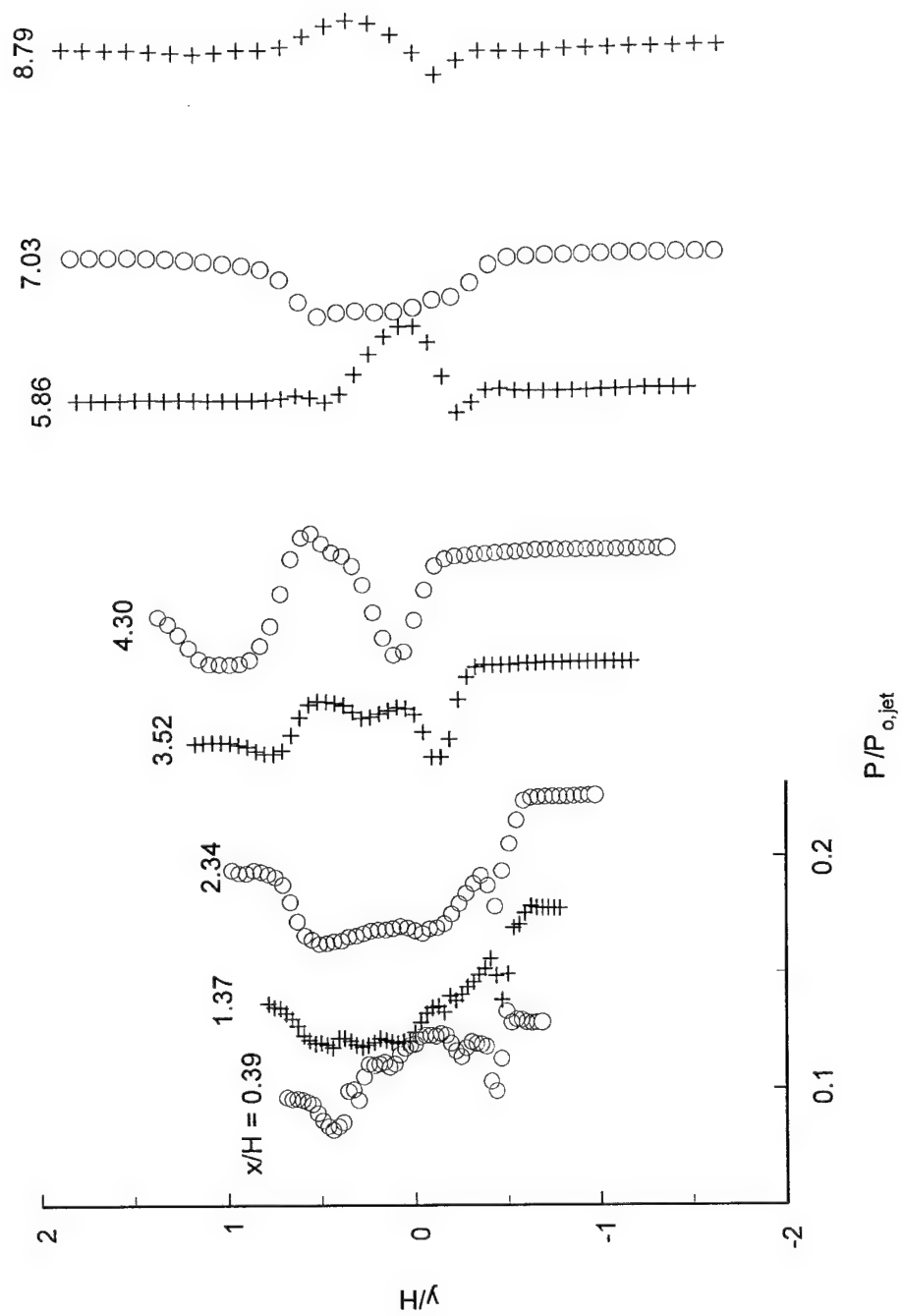


Figure A.27: Static pressure profiles at various streamwise locations for the thrust vectoring configuration without suction

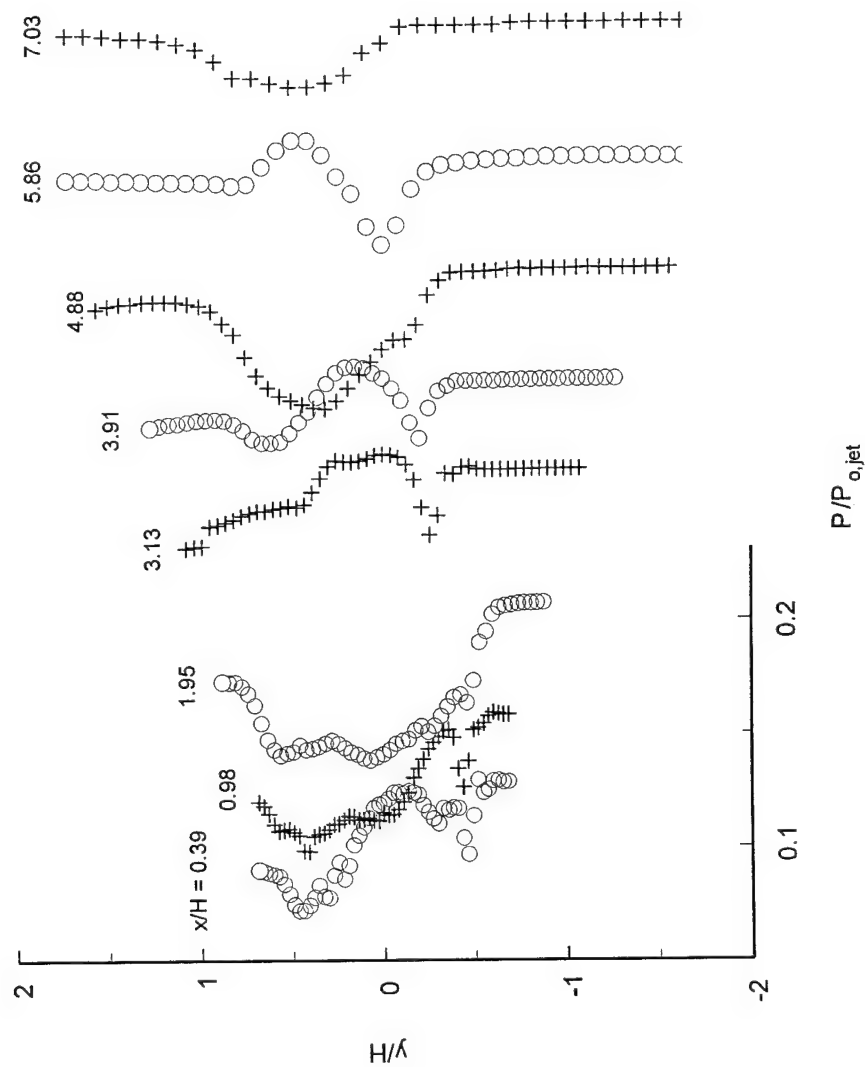


Figure A.28: Static pressure profiles at various streamwise locations for the thrust vectoring configuration with moderate suction

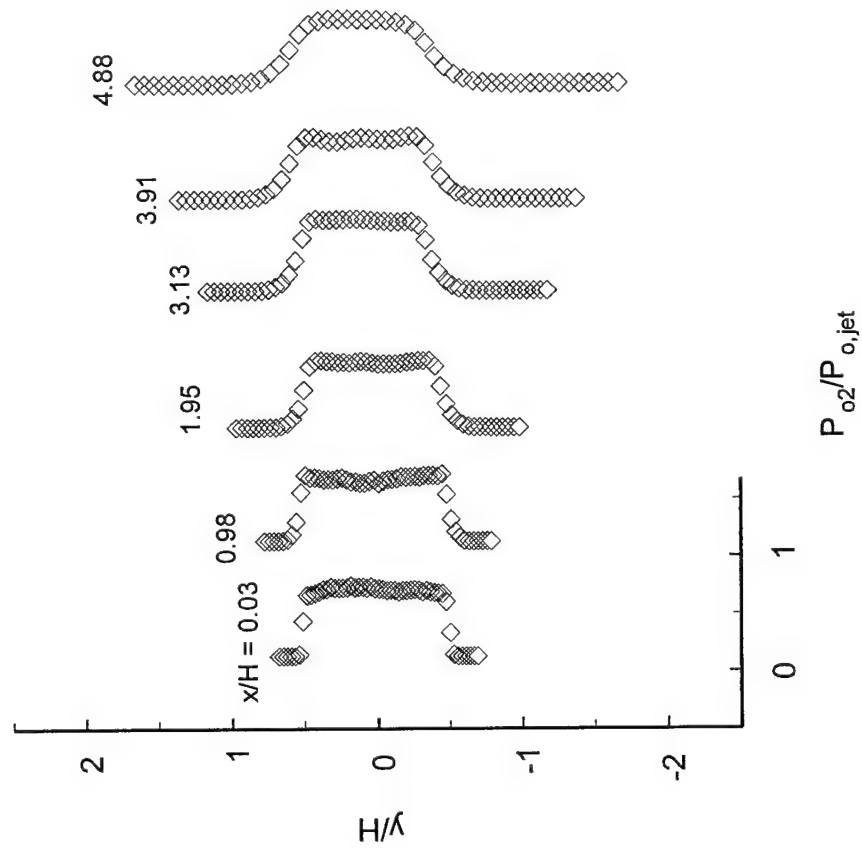


Figure A.29: Total pressure profiles at various streamwise locations for the ideally expanded free jet

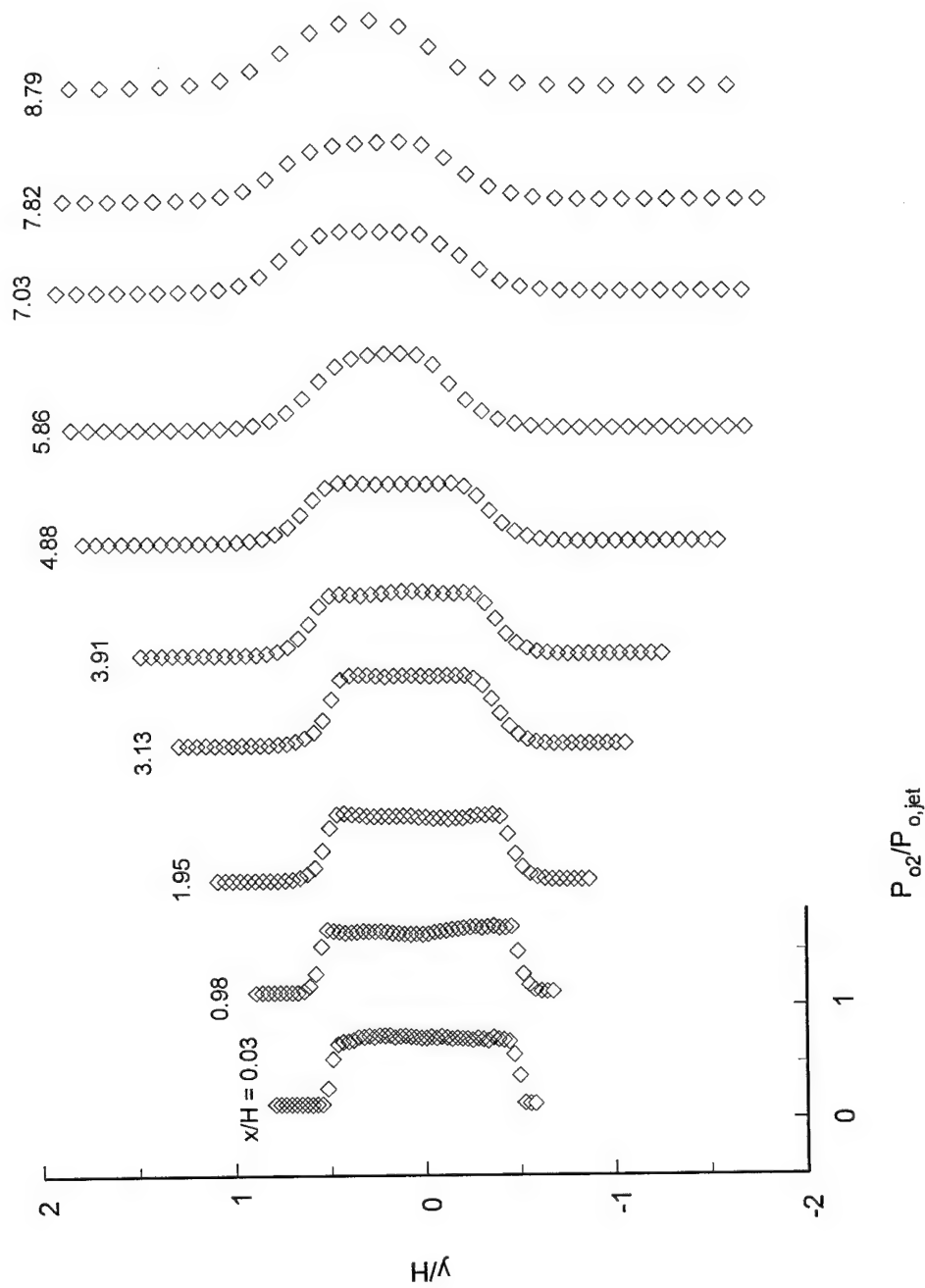


Figure A.30: Total pressure profiles at various streamwise locations for the thrust vectoring configuration without suction

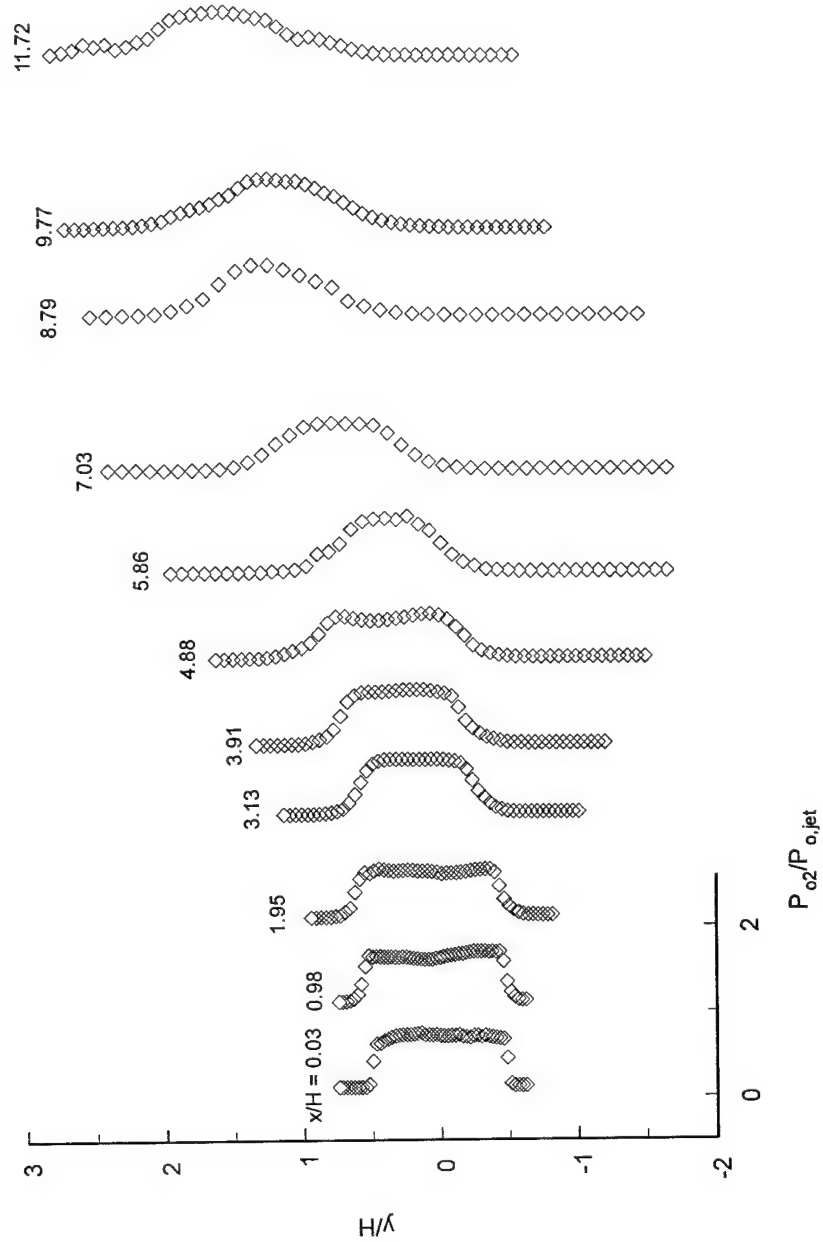


Figure A.31: Total pressure profiles at various streamwise locations for the thrust vectoring configuration with moderate suction

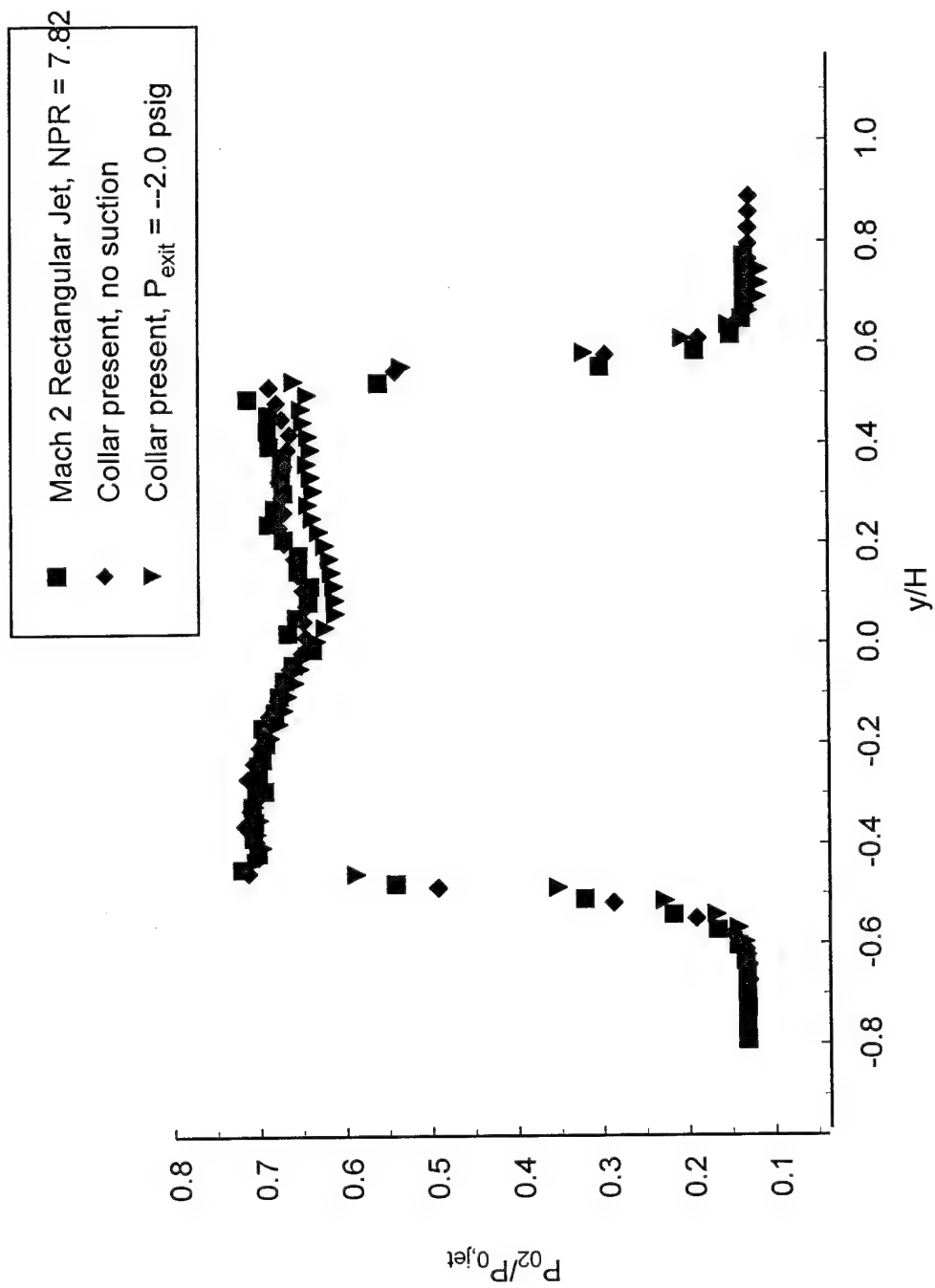


Figure A.32: Total pressure profiles for various jet conditions at $x/H = 0.977$

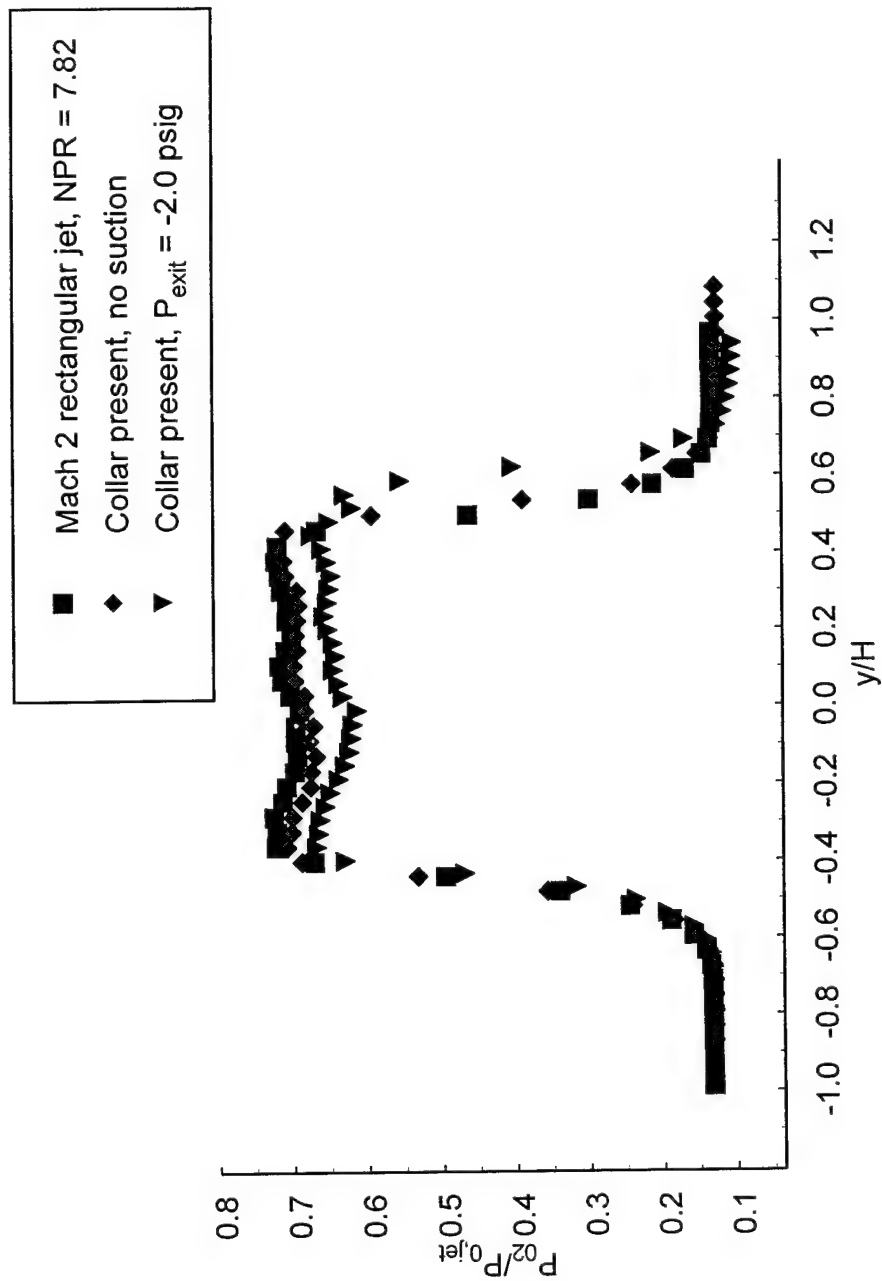


Figure A.33: Total pressure profiles for various jet conditions at $x/H = 0.977$

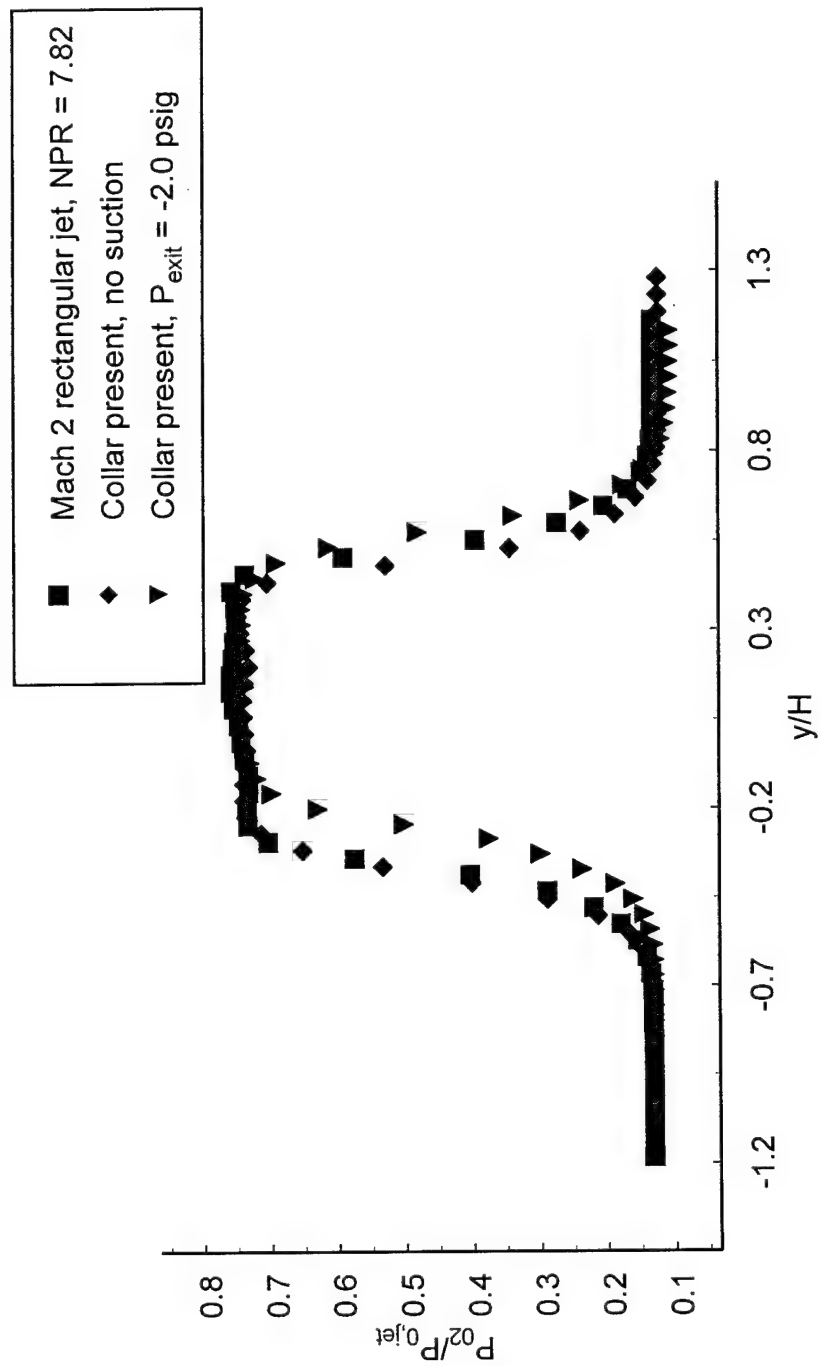


Figure A.34: Total pressure profiles for various jet conditions at $x/H = 3.13$

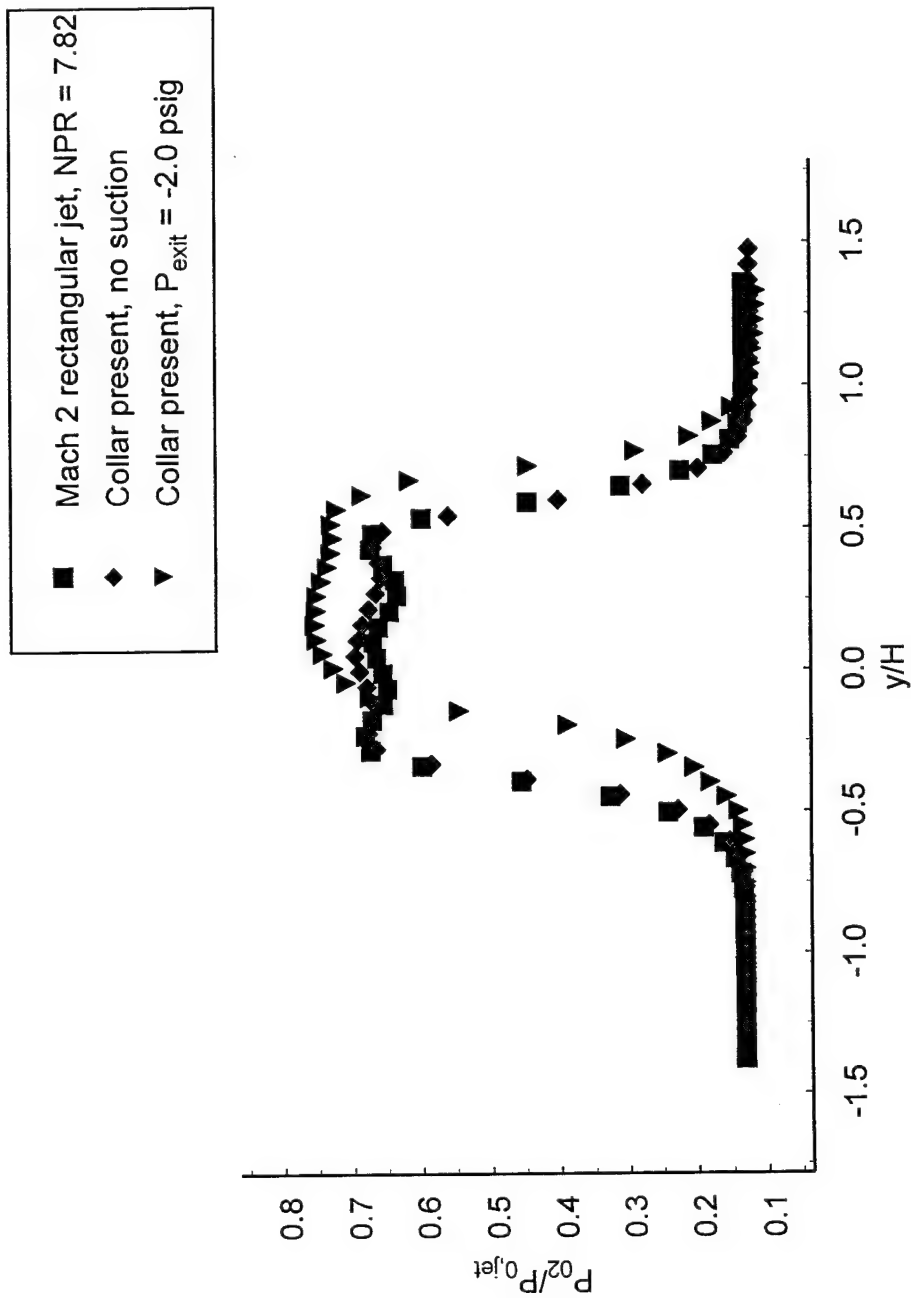


Figure A.35: Total pressure profiles for various jet conditions at $x/H = 3.91$

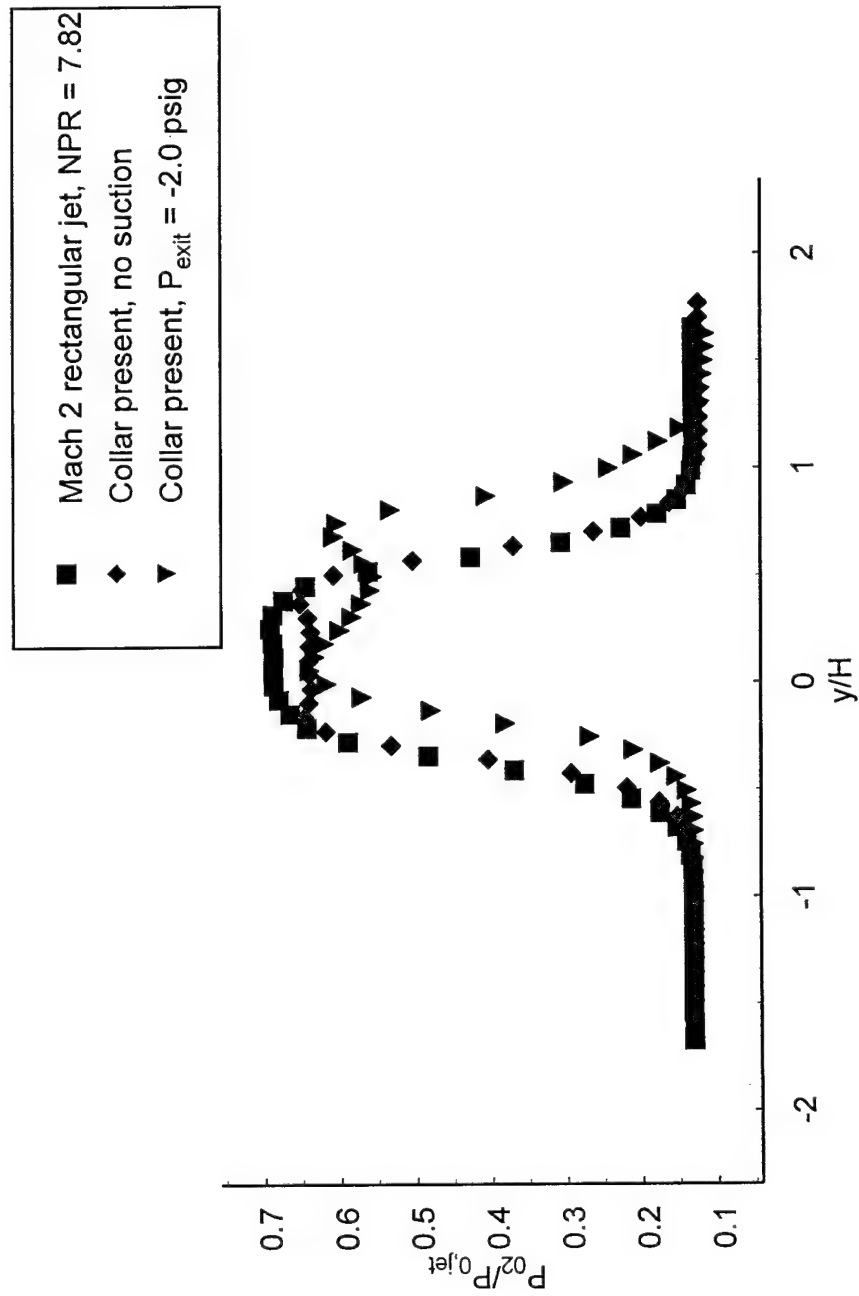


Figure A.36: Total pressure profiles for various jet conditions at $x/H = 4.88$

Discussion of Pressure Measurements

A comparison between the total pressure profiles of the various cases at different streamwise locations can give insight into the shock structure present in the flow. Figure A.32 shows total pressure profiles for x/H equal to 0.977 which shows that the profiles are quite similar except for the collar side half of the vectored case. The observed drop in total pressure P_{02} is due to an expansion fan (increase in Mach number) that originates at the collar side nozzle lip and is passing approximately halfway across the jet at this location. The next downstream location as depicted in Figure A.33 (x/H equal to 1.95) shows the vectored jet has entirely passed through the expansion fan. The following two downstream locations of $x/H = 3.13$ (Figure A.34) and $x/H = 3.91$ (Figure A.35) show a gradual increase in P_{02} for the vectored jet, which suggests the presence of a compression process (drop in Mach number). A shifting of the profiles toward the collar for the vectored jet is also observed. The vectored jet profile at x/H of 4.88 (Figure A.36) shows that a strong expansion process has occurred since the last profile location, and the shifting of the core is readily seen. The only noticeable difference between the free jet and the ejector case is at this location, as the ejector profile has a decrease in P_{02} in the core region. Therefore, the addition of the collar does have a mild effect on the location of the shock cells.

Static pressure profiles were taken for the three cases at various streamwise locations as shown by the static pressure distributions of Figures A.27, A.28 and A.29. The static pressure measurement is complicated by leading edge wave reflection off the shear

layer, which can impact on the probe near the static pressure ports. This effect is generally limited to probe locations very close to the sonic line, where the reflections occur. The free jet static pressure profiles are symmetric as expected. The static pressure in the core of the jet may be above or below 14.7 psia, depending on the type of process occurring (expansion or compression). When the collar is added, the profiles become more asymmetric. In many of these profiles, the static pressure in the gap between the jet and the collar is quite low, which suggests that the mere presence of the probe has caused vectoring of the jet (more so than for the pitot pressure measurements). This sensitivity of the jet to intrusive measurement techniques was observed during all of the pressure measurements, with the static probe causing more problems. This effect illustrates the importance of using nonintrusive techniques such as PIV. The addition of suction tended to make the collar side static pressure drop relative to the no suction case.

REFERENCES

- Ashley, S., "Thrust Vectoring: A New Angle to Air Superiority," *Mechanical Engineering*, January 1995, pp. 58-64.
- Boggs, R., "Engineers Leap Vectoring Barrier," *Design News*, November 23, 1992, pp. 60-63.
- Brown, G. L., and Roshko, A. R., "On Density Effects and Large Structure in Turbulent Mixing Layers," *Journal of Fluid Mechanics*, Vol. 64, No. 4, 1974, pp. 775-781.
- Chih, C., Krothapalli, A., and Gogineni, S., "Experimental Observations on Instability Modes in a rectangular Jet," *AIAA Journal*, Vol. 30, No. 10, October 1992, pp. 2388-2394.
- Clemens, N. T. and Mungal, M.G., "Two- and Three-Dimensional Effects in the Supersonic Mixing Layer," *AIAA Journal*, Vol. 30, No. 4, April 1992, pp. 973-981.
- Crow, S. C. and Champagne, F. H., "Orderly Structure in Jet Turbulence," *Journal of Fluid Mechanics*, Vol. 48, 1971, pp. 547-591.
- Drazin, P. G. and Reid, W. H., *Hydrodynamic Stability*, Cambridge University Press, New York, 1981.
- Goebel, S. G. and Dutton, J. C., "Experimental Study of Compressible Turbulent Mixing Layers," *AIAA Journal*, Vol. 29, No. 4, April 1991, pp. 538-546.
- Gutmark, Ephraim and Ho, Chih-Ming, "Preferred Modes and the Spreading Rates of Jets," *Physics of Fluids*, Vol. 26, No. 10, October 1983, pp. 2932-2938.
- Hedges, L. S. and Eberhardt, D. S., "Comparison of Confined, Compressible, Spatially Developing Mixing Layers with Temporal Mixing Layers," *AIAA Journal*, Vol. 31, No. 11, November 1993, pp. 1977-1983.
- Humphrey, J. A. C., Li, S., "Tilting, Stretching, Pairing, and Collapse of Vortex Structures in Confined Countercurrent Flow," *Trans. ASME. J. Fluids Engineering*, Vol. 103, 1981, p466.
- King, C. J., Krothapalli, A., Strykowski, P. J., "The Effect of Annular Counterflow on Supersonic Jet Noise," *Proceedings of the First Joint CEAS/AIAA Aeroacoustics Conference*, Munich, Germany, June 12-15, 1995.

- Krothapalli, A., Baganoff, D., and Karamcheti, K., "On the Mixing of a Rectangular Jet," *Journal of Fluid Mechanics*, Vol. 107, 1981, pp. 201-22.
- Krothapalli, A., Hsia, Y., Baganoff, D., and Karamcheti, K., "The Role of Screech Tones in Mixing of an Underexpanded Rectangular Jet," *Journal of Sound and Vibration*, Vol. 106, No.1, 1986, pp. 119-143.
- Lepicovsky, J., Ahuja, K. K., Brown, W. H., and Burrin, R. H., "Coherent Large-Scale Structures in High Reynolds Number Supersonic Jets," *AIAA Journal*, Vol. 25, No. 11, November 1987, pp. 1419-1425.
- Liepmann, H. W., and Roshko, A., *Elements of Gas Dynamics*, John Wiley & Sons, Inc., New York, 1957.
- Panton, R. L., *Incompressible Flow*, John Wiley & Sons, New York, 1984.
- Papamoschou, Dimitri, and Roshko, Anatol, "The Compressible Turbulent Shear Layer: an Experimental Study," *Journal of Fluid Mechanics*, Vol. 197, 1988, pp. 453-477.
- Papamoschou, Dimitri, "Structure of the Compressible Turbulent Shear Layer," *AIAA Journal*, Vol. 29, No. 5, May 1991, pp. 680-681.
- Plesniak, M. W., and Johnston, J. P., "Reynolds Stress Evolution in Curved Two-Dimensional Mixing Layers," *Proceedings of the Seventh Symposium on Turbulent Shear Flows*, Stanford University, Stanford, CA, Aug. 21-23, 1989, pp. 6.3.1-6.3.6.
- Powell, Alan, "The Noise of Choked Jets," *Journal of the Acoustical Society of America*, Vol. 25, No. 3, May 1953, pp. 385-389.
- Quinn, W. R., "Streamwise Evolution of a Square Jet Cross Section," *AIAA Journal*, Vol. 30, No. 12, December 1992, pp. 2852-2857.
- Ramshankar, R., "The Dynamics of Countercurrent Mixing Layers," Yale Ph. D. Thesis, 1988.
- Roshko, A., and Bernal, L. P., "Streamwise Vortex Structure in Plane Mixing Layers," *Journal of Fluid Mechanics*, Vol. 170, 1986, pp. 499-525.
- Ross, C. B., "Calibration of Particle Image Velocimetry in a Shock-Containing Supersonic Flow," M. S. Thesis, Florida State University, Tallahassee, FL, 1993.
- Saad, M. A., *Compressible Fluid Flow*, Prentice Hall, New Jersey, 1993.
- Samimy, M., Reeder, M. F., and Elliot, G. S., "Compressibility Effects on Large Structures in Free Shear Flows," *Physics of Fluids*, Vol. 4, No. 6, June 1992, pp. 1251-1258.

- Shapiro, A. H., *The Dynamics and Thermodynamics of Compressible Fluid Flow*, Vol. 1, Ronald Press, New York, 1953.
- Shau, Y. R., and Dolling, D. S., "Exploratory Study of Turbulent Structure of a Compressible Shear Layer using Fluctuating Pitot Pressure Measurements," *Experiments in Fluids*, 1992, pp. 293-306.
- Shau, Y. R., Dolling, D. S., and Choi, K. Y., "Organized Structure in a Compressible Turbulent Shear Layer," *AIAA Journal*, Vol. 31, No. 8, August 1993, pp. 1398-1405.
- Strykowski, P. J., Krothapalli, A., Alvi, F. S., and King, C. J., "Mixing Characteristics of Countercurrent Compressible Turbulent Shear Layers," Seventh ONR Propulsion Meeting, Buffalo, NY, Aug. 29-31, 1994, pp. 204-215.
- Strykowski, P. J., Krothapalli, A., and Forliti, D. J., "Counterflow Thrust Vectoring of a Supersonic Rectangular Jet," *To be submitted to the AIAA Journal*, 1995.
- Strykowski, P. J. and Niccum, N. L., "The Stability of Countercurrent Mixing Layers in Circular Jets," *Journal of Fluid Mechanics*, Vol. 227, 1991, pp. 309-343.
- Strykowski, P. J., and Wilcoxon, R. K., "Mixing Enhancement Due to Global Oscillations in Jets with Annular Counterflow," *AIAA Journal*, Vol. 31, No. 3, March 1993, pp. 564-570.
- Strykowski, P. J., and Wilcoxon, R. K., "Self-Excitation and Mixing in Axisymmetric Jets with Counterflow," AIAA Paper No. 92-0538, January 1992.
- Van der Veer, M. R., "Counterflow Thrust Vectoring of a Subsonic Rectangular Jet," M. S. Thesis, University of Minnesota, Minneapolis, MN, 1995.
- Wishart, D. P., and Krothapalli, A. "On the Structure of a Heated Supersonic Jet," AIAA Paper No. 94-0666, January 1994.
- Wishart, D. P., "The Structure of a Heated Supersonic Jet Operating at Design and Off-Design Conditions," Ph. D. Thesis, Florida State University, Tallahassee, FL, 1995.

BIOGRAPHICAL SKETCH

David John Forliti was born November 15, 1969 in St. Paul, Minnesota. He attended the University of Minnesota, where he received a Bachelor of Science degree in Mechanical Engineering with distinction and cum laude honor's including an undergraduate thesis during the summer of 1993. Employment positions included two years of undergraduate teaching assistant experience as well as one year as an undergraduate research assistant.

Upon finishing his undergraduate experience, the author began working on a master of science at the College of Engineering, a joint school of Florida State University and Florida A & M University, during the fall semester of 1993. During the following two years, he spent one semester as a teaching assistant and three semesters working as a research assistant at the Fluid Mechanics Research Laboratory on the Florida State University campus. Research topics involve experimental investigation of high speed fluid mechanics using optical methods such as schlieren flow visualization and Particle Image Velocimetry as well as intrusive pressure measurement techniques. He will receive his master of science degree summer semester of 1995.